STUDIA UNIVERSITATIS
BABEŞ-BOLYAI

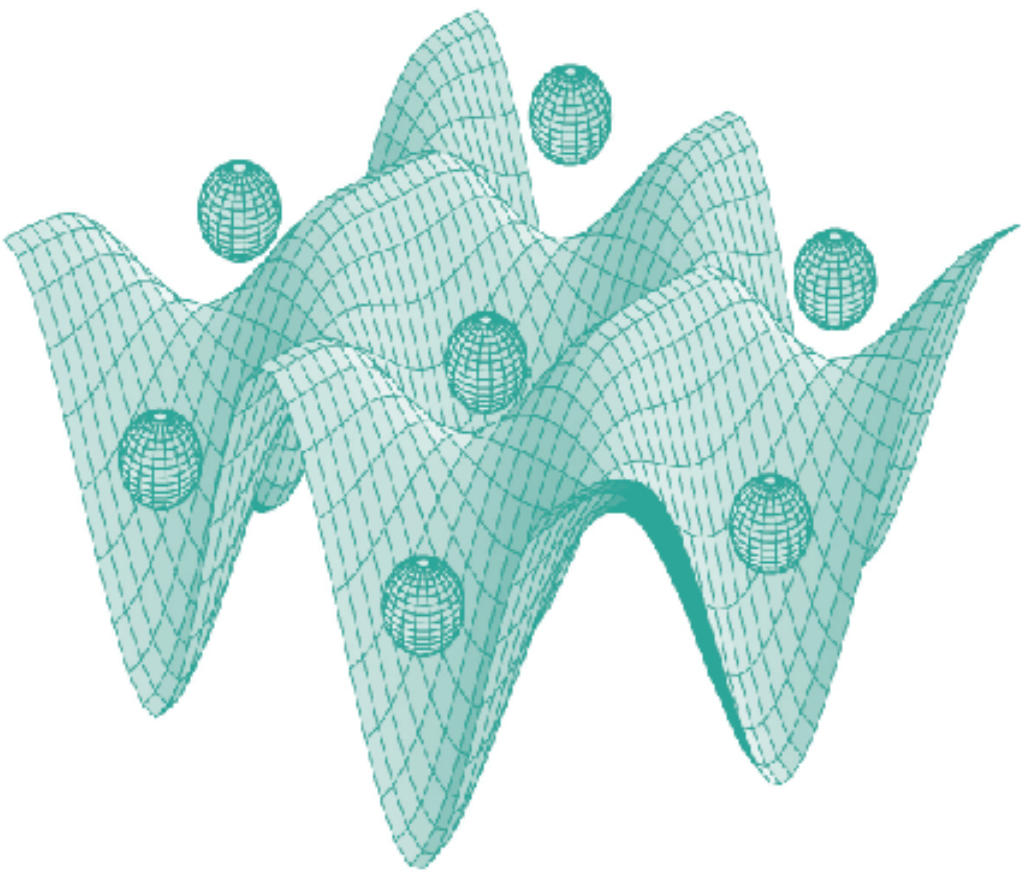

PHYSICA

1-2/2023

STUDIA
UNIVERSITATIS BABEŞ-BOLYAI
PHYSICA

1-2/2023

ISSN (print): 0258-8730;
ISSN (online): 2065-9415; ISSN-L: 0258-8730;

Published by Babeş-Bolyai University

EDITORIAL OFFICE OF STUDIA UBB PYSICA:
1, M. Kogălniceanu St., Cluj-Napoca, ROMANIA, Phone: +40 264 405300
http://www.studia.ubbcluj.ro/serii/physica/index_en.html

YEAR **Volume 68 (LXVIII) 2023**
MONTH **DECEMBER**
ISSUE **1-2**

PUBLISHED ONLINE: 2023-12-30
PUBLISHED PRINT: 2023-12-30
ISSUE DOI:10.24193/subbphys.2023

S T U D I A
UNIVERSITATIS BABEȘ–BOLYAI
PHYSICA

1-2

CUPRINS – CONTENT – SOMMAIRE – INHALT

STUDIA UBB PHYSICA, Vol. 68 (LXVIII), 1-2, 2023, pp. 5-12
(RECOMMENDED CITATION)
doi:10.24193/subbphys.2023.01

CALCULATION OF NUCLEAR STOPPING POWER

Zs. BÁLINT[1] and L. NAGY[1*]

ABSTRACT. Fast charged particles interact with matter mainly by interaction with the electron shell of the atoms causing ionization and excitation, i.e. inelastic scattering. However, for lower velocity projectiles an important part of the energy loss is due to elastic scattering on the nuclei, which is called nuclear stopping. In the present paper we calculate the nuclear stopping cross section of protons and antiprotons in different materials. The obtained results are compared with calculations by other groups and with the electronic stopping cross sections. The difference between the results for protons and antiprotons is explained.

Keywords: *interaction of charged particles with matter, nuclear stopping, Barkas effect*

INTRODUCTION

The interaction of fast charged particles with matter is studied since the discovery of radioactivity. Shortly after the structure of the atom was clarified by the experiments proposed by Rutherford [1], a theory for the slowing down of α and β-rays in matter was published by Bohr [2]. After the elaboration of quantum mechanics, Bethe deduced a formula (based on the Born approximation) for the stopping power of fast ions in matter [3], which is widely used till today.

The slowing down of protons and heavier ions in different materials has great practical importance in many fields. Precise calculations are needed for hadron therapy, different material science and astrophysical applications.

[1] *Babeș-Bolyai University, Faculty of Physics, 1 Kogălniceanu str., 400084 Cluj-Napoca, Romania*
* *Corresponding author: ladislau.nagy@ubbcluj.ro*

Charged particles passing through matter lose their energy due to the interaction with the atoms. The most important and extensively studied process is the energy loss of the projectile due to the interaction with the electrons causing excitation or ionization. The mentioned Bethe model considers only this process. However, there exists also energy loss because of the elastic collisions of the projectile with the nuclei. This is negligible relative to the electron stopping at high energies but may be important for lower energy projectiles. This nuclear stopping is far less studied in the literature relative to the electron stopping. Examples of such calculations for proton and other ion projectiles are in the book of Ziegler, Biersack and Littmark [4] and the computer code developed by them [5]. A detailed study for nuclear stopping of antiprotons in different materials was published by Nordlund [6], and some results for helium and hydrogen targets are also available [7, 8].

THEORY

The nuclear stopping is due to the elastic collision of the projectile with the nuclei from the target. Except for extremely low energies, when the de Broglie wavelength of the projectile ion becomes comparable with the atomic dimensions, the collision process may be treated classically. From the theory of classical scattering one obtains, that the θ scattering angle for a projectile with energy E_0 can be written as [7]

$$\theta(b) = \pi - 2\int_{r_{min}}^{\infty} \frac{b\,dr}{r^2\sqrt{1-V(r)/E_c-b^2/r^2}}, \tag{1}$$

where b represents the impact parameter of the projectile, r is the distance between the projectile and the target atom (with respective masses m_p and m_t), $E_c = \frac{E_0 m_t}{m_p+m_t}$ is the center-of-mass energy and V(r) is the screened Coulomb potential. The r_{min} distance is given by the largest root for the zero value of the term under the square root.

The energy transferred to the atom during elastic scattering depends on the scattering angle of the projectile:

$$T(b) = 4\,\frac{m_p \cdot m_t}{(m_p+m_t)^2}\,E_0 \sin^2\left(\frac{\theta}{2}\right). \tag{2}$$

The nuclear stopping cross section is defined as the integral of the kinetic energy transferred to the target atom over all impact parameters [7],

$$S_n = 2\pi\int_0^{\infty} b\,T(b)\,db. \tag{3}$$

The stopping power is related to the stopping cross section by

$$-\frac{\langle \Delta E \rangle}{\Delta x} = N(-S), \tag{4}$$

where N is the atomic density of the target material; the minus sign indicates energy lost by the projectile and transferred to the target atom [9].

If in the expression (2) of the transferred energy one calculates the angle from the pure Coulomb scattering on the nucleus, a divergent integral for the nuclear stopping cross section is obtained, due to the infinite range of the Coulomb potential. In order to avoid this problem one has to take into account the screening effect of the electron cloud, resulting in a projectile-atom potential of finite range.

There are several different models for the calculation of the interaction potential V(r). We have performed the calculations first assuming a frozen electron cloud (more appropriate for fast projectiles), and then a static potential, accounting for the static influence of the projectile on the atom (adiabatic approximation).

For hydrogen, we compare the results calculated from the frozen core model with those obtained with the static potential. For helium we use only the frozen core model, while for Be, C, N, O, Ne, Al and Si targets we use the potential calculated for the antiproton projectile [6] for both proton and antiproton projectiles.

The antiproton projectiles can collide with the nucleus due to the attractive potential, in which case nuclear reactions may occur [6]. Because we did not consider these processes, events where the antiproton came closer than 3 fm to the nucleus were excluded from the calculation. Since the probability of a nuclear reaction is very small, the results do not change significantly.

In the expression of the scattering angle, the value of the integrand approaches infinity near r_{min}, so here we have used an analytical approximation for the first small interval.

RESULTS AND DISCUSSION

Helium

For helium, we calculated the interaction potential applying the frozen core approximation. The potential for proton projectiles, using a wavefunction for the helium atom obtained from a simple variational method, can be written as:

$$V(r) = e^{-2\alpha r}\left(2\alpha + \frac{2}{r}\right), \tag{5}$$

where $\alpha = \frac{27}{16} \approx 1.6875$.

In Fig. 1, we present our results for the antiproton-helium and proton-helium nuclear stopping cross sections. For antiprotons we find good agreement with the theoretical results of Bailey et al. [9], and Schiwietz et al. [10], respectively for protons with the results of the SRIM program [5]. In both cases, the value of nuclear stopping is found to exceed that of electronic stopping at low energies.

Comparing the results for proton and antiproton projectiles one may observe that the nuclear stopping cross section for antiproton projectiles is significantly higher than for protons, so the Barkas effect [11] is valid also for the nuclear stopping. This result is different from the pure Coulomb scattering, where the cross section does not depend on the charge sign of the projectile. The cause of this charge dependence is that the antiproton, attracted by the nucleus, passes it at a smaller distance, resulting in a higher potential and energy transfer.

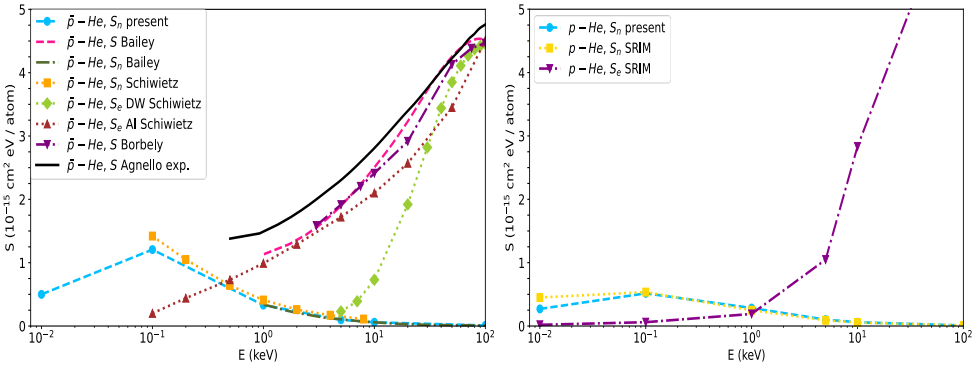

Fig. 1: Stopping cross sections (S_n – nuclear, S_e – electronic, S - total) of antiprotons (left panel) and protons (right panel) in He as a function of projectile energy. The present frozen core approximation results are compared to other theoretical calculations: nuclear stopping cross sections of Bailey et al. [7] and Schiwietz et al. [10], electronic and total stopping cross sections of Bailey et al. [7], Borbély et al. [9] and Schiwietz et al. [10], and to the experimental data for $\bar{p}$ of Agnello et al. [8]. For p the electronic and nuclear cross sections obtained from the SRIM program [5] are presented.

Hydrogen

For hydrogen targets, we have calculated the nuclear stopping cross section using both models: the frozen core approximation and using the potential calculated for hydrogen in [6]. The interaction potential calculated from the frozen core model for proton projectile is

$$V(r) = e^{-2r}\left(1 + \frac{1}{r}\right). \quad (6)$$

Whereas the adiabatic potential calculated for antiprotons [6] can be written as

$$V(r) = \frac{Z_1 Z_2}{r}\Phi^{exp}, \quad (7)$$

where Φ^{exp} is the screening function, which can be written as the sum of a few exponential functions.

In Fig. 2, we present our results for the antiproton-hydrogen and proton-hydrogen nuclear stopping cross sections calculated from both the frozen core and adiabatic approximation models. The results calculated for the antiproton from the two models show a significant discrepancy at 10 eV. Since the frozen core model does not take into account the distortion of the electron cloud due to the interaction with the projectile, the value calculated using the adiabatic approximation may be closer to the true nuclear stopping in this case. Our results are lower than the results presented in the article [6]. The reason for the discrepancy may be due to differences in the calculation methods.

For proton projectiles, the adiabatic approximation and frozen core models show good agreement at higher energies, but at lower energies the frozen core model results in a larger stopping cross section than the one calculated with the adiabatic approximation. The adiabatic approximation results are in good agreement with the nuclear stopping cross sections obtained from the SRIM program.

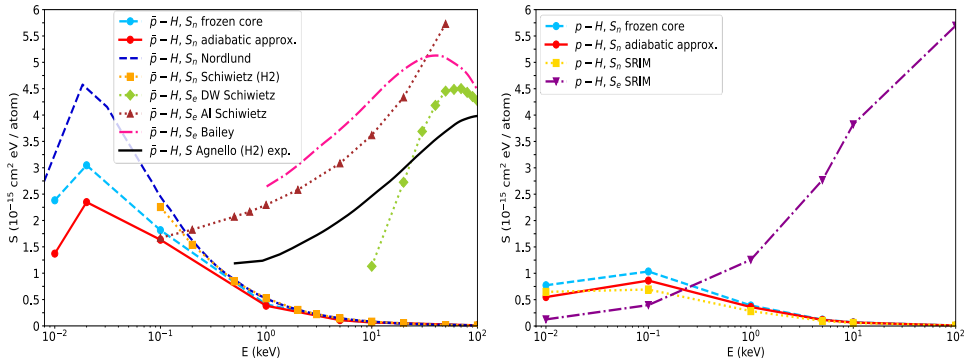

Fig. 2: Stopping cross sections (S_n – nuclear, S_e – electronic, S - total) of antiprotons (left panel) and protons (right panel) in H as a function of projectile energy. The present frozen core and adiabatic approximation results are compared to other theoretical calculations: nuclear stopping cross sections of Nordlund et al. [6] and Schiwietz et al. [10], electronic cross sections of Bailey et al. [7] and Schiwietz et al. [10], and to the experimental data for $\bar{p}$ of Agnello et al. [8]. For p the electronic and nuclear cross sections obtained from the SRIM program [5] are presented.

Silicon

In Fig. 3, we compare our result for the nuclear stopping cross section obtained with the adiabatic approximation for a silicon target with the results of Nordlund et al. [6] and those obtained from the SRIM program. As in the case of hydrogen, there is a discrepancy between the nuclear stopping calculated for antiprotons and the results presented in [6]. The value of nuclear stopping in this case exceeds the value of electronic stopping below 100 eV.

For protons (except for 1 keV), our results are in good agreement with the results of the SRIM program and the results of Nordlund et al. [6].

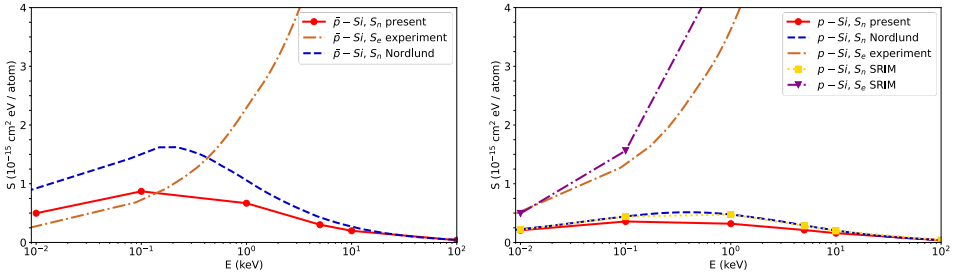

Fig. 3: Stopping cross sections (S_n – nuclear, S_e – electronic) of antiprotons (left panel) and protons (right panel) in Si as a function of projectile energy. The present adiabatic approximation results are compared to other theoretical calculations: the nuclear cross sections of Nordlund et al. [6] and the data obtained from the SRIM program [5]. The experimental data are taken from [6].

Beryllium

In Fig. 4, we present our results for the antiproton-beryllium and proton-beryllium nuclear stopping cross sections calculated from the adiabatic approximation model.

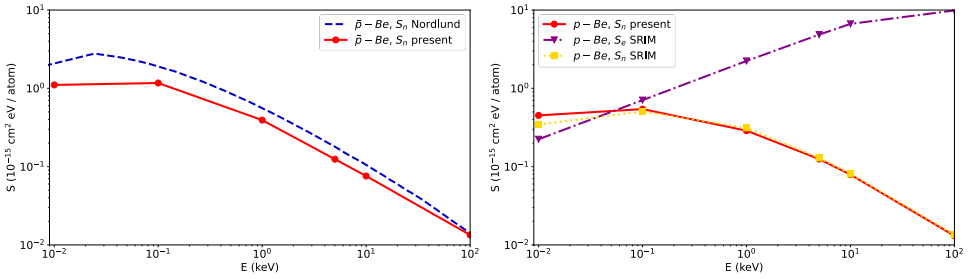

Fig. 4: Stopping cross sections (S_n – nuclear, S_e – electronic) of antiprotons (left panel) and protons (right panel) in Be as a function of projectile energy. The present adiabatic approximation results are compared to other theoretical calculations: nuclear stopping cross section of Nordlund et al. [6] for $\bar{p}$ and the electronic and nuclear cross sections obtained from the SRIM program [5].

There is a significant discrepancy between our results calculated for antiproton projectiles below 100 keV and the results of the article [6]. However, for proton projectiles our results show good agreement with the results of the SRIM program.

Nitrogen

In Fig. 5, we present our results for the antiproton-nitrogen and proton-nitrogen nuclear stopping cross sections calculated from the adiabatic approximation model. For antiproton projectiles below 5 keV, there is no good agreement between our results and the results of the article [6]. The values of the proton-nitrogen nuclear stopping cross section are in good agreement with the results of the SRIM program at higher energies, but below 5 keV there is a visible difference between the two curves.

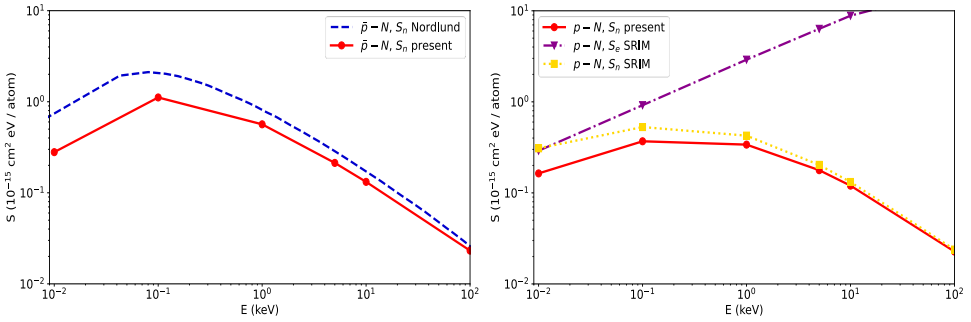

Fig. 5: Stopping cross sections (S_n – nuclear, S_e – electronic) of antiprotons (left panel) and protons (right panel) in N as a function of projectile energy. The present adiabatic approximation results are compared to other theoretical calculations: nuclear stopping cross section of Nordlund et al. [6] for $\bar{p}$ and the electronic and nuclear cross sections obtained from the SRIM program [5].

CONCLUSIONS

Nuclear stopping power of charged particles was studied using a classical model. We have numerically calculated the nuclear stopping cross section of proton and antiproton projectiles for H, He, Be, C, N, O, Ne, Al, and Si targets.

Due to the attractive interaction between the nucleus and the antiproton, the minimal distance between the target and the projectile is smaller, resulting in larger scattering angle and larger energy transfer than for a proton projectile under similar conditions. Thus, for all targets, the nuclear stopping power is higher for antiproton projectiles than for protons of the same energy (Barkas effect).

It was shown that at low energies, the value of the nuclear stopping cross section is significant, and in may cases larger, relative to the electronic stopping cross section.

For helium and hydrogen targets we have used a frozen core approximation, and the results obtained were in good agreement with the results of Bailey et al. [7] and Schiwietz et al. [10]. In the case of hydrogen, the small difference with the results of Schiwietz et al. [10] can be explained with the fact that in [10] the nuclear stopping was calculated for hydrogen molecules.

Our results calculated with the Nordlund static potential are not in good agreement with the results presented in the original article [3]. The reason for the discrepancy may be due to differences in the calculation methods. In [6] the interaction of the antiproton with the atoms was modelled by using molecular dynamics simulations. We calculated the nuclear stopping cross sections using equations (1)-(3) with great attention to the convergence of the integrals, which is a more direct method.

REFERENCES

1. E. Rutherford, *Philos. Mag. Ser. 6*, 21, 669–688 (1911).
2. N. Bohr, *Philos. Mag.*, 25, 10 (1913).
3. H. Bethe, *Ann. Phys. (Berlin)*, 397, 325 (1930).
4. J. F. Ziegler, J. P. Biersack, and U. Littmark, "The Stopping and Range of Ions in Matter", Pergamon, New York, **1985**.
5. J. Ziegler, and J. Biersack, SRIM, http://www.srim.org.
6. K. Nordlund *et al.*, *Phys. Rev. A*, 96, 042717 (2017).
7. J. J. Bailey *et al.*, *Phys. Rev. A*, 92, 022707 (2015).
8. M. Agnello *et al.*, *Phys. Rev. Lett.*, 74, 371–374 (1995).
9. S. Borbély *et al.*, *Phys. Rev. A*, 98, 012707 (2018).
10. G. Schiwietz *et al.*, *J. Phys. B: At. Mol. Opt. Phys.*, 29, 307 (1996).
11. W. H. Barkas, J. N. Dyer, and H. H. Heckman, *Phys. Rev. Lett.*, 11, 26 (1963).

STUDIA UBB PHYSICA, Vol. 68 (LXVIII), 1-2, 2023, pp. 13-24
(RECOMMENDED CITATION)
doi:10.24193/subbphys.2023.02

EXPERIMENTAL DEVICE FOR THE STUDY OF PERMANENT MAGNET ARRANGEMENTS

K. BODÓ[1], A. R. TUNYAGI[2] and A. SIMON[2*]

ABSTRACT. In this paper we present a complex experimental device used for the study of the magnetic field created by neodymium magnet arrangements, with emphasis on the series and parallel connection of those magnets. The measurements performed are suitable and useful for both high-school or college/university-level students.

Keywords: *magnet arrangement; magnetic flux density; series, parallel and mixed connection; equivalent magnet*

INTRODUCTION

Magnets are objects used to produce magnetic field. This field is invisible for the human eye but it can be foreseen, computed, depicted, or experimentally mapped for some common geometric shapes [1, 2]. Because permanent magnets are extensively used in a wide range of applications from electrical and radio engineering, to household appliances, transportation, medicine, and many other fields [3-6] the understanding of the magnetic field by terms of magnetic flux density (or field strength) is very important for implementations.

Some applications require more sophisticated magnetic field configurations than those created by individual magnets, thus special arrangements of magnetic structures have been developed for both research and applications, also aiming the strongest possible field per mass of permanent magnet material. Historically

[1] *Undergraduate student, Engineering Physics, Babeș-Bolyai University, Faculty of Physics, M. Kogălniceanu 1, 400084 Cluj-Napoca, Romania.*
[2] *Babeș-Bolyai University, Faculty of Physics, M. Kogălniceanu 1, 400084 Cluj-Napoca, Romania*
* *Corresponding author: alpar.simon@ubbcluj.ro*

speaking, one of the most spectacular structures is that increase the magnetic flux on one side of the arrangement while reducing, or even canceling it on the opposite side. Such arrangements were first theoretically proposed by Mallinson [7] and later realized by Halbach [8-10].

The topic of experimental measurements on magnet arrangements is a complex and challenging one, from both theoretical and experimental point of views and rises an excellent inter- and multidisciplinary subject for Engineering Physics undergraduate students.

The present paper describes the design and implementation of an experimental device used for the study of permanent magnet arrangements. It was proposed as a graduation project for Engineering Physics specialization, at Babeș-Bolyai University, Faculty of Physics [11].

It is organized as follows: in the first section some general considerations are presented about permanent magnets and magnetic flux density measurement techniques, with emphasis on some previous measurements performed in our laboratory. The design and implementation of the device are described in the subsequent sections and finally, the measurement results are presented and conclusions are made.

Permanent magnets and magnetic flux density measurement

A magnet is called permanent if its magnetic properties are perpetual and it generates its own persistent magnetic field outside the material without any external trigger (energy source) like electromagnets.

There are four material families of permanent magnets, each of them having properties and features which maintain both scientific and commercial interest about them. Their properties, advantages or inconveniences in their use are extensively discussed in scientific literature [6, 12, 13]

The magnetic behavior of those materials is described in terms of four interrelated vector quantities: $\vec{B}$ – magnetic induction or flux density (it is expressed in terms of flux lines per unit of cross-section area, describing the concentration of magnetic flux at a point in space), $\vec{H}$ – magnetic field strength or intensity, $\vec{M}$ – magnetization (it describes the magnetic state of the material, representing the vector sum of individual atomic magnetic moments per unit volume) and $\vec{F}$ – magnetic force (attractive/repulsive type, usually arises between electrically charged particles because of their motion, it is also used to describe strength).

Nowadays the measurement of the magnetic flux density is not a very difficult task, both commercially available magnetometers and Hall sensors are helpful for the user. The attraction or repulsion force between two magnets is also easily measurable using force measurement devices or sensors, but to find the force produced by a single magnet or a more complex arrangement is a tricky task – it

requires the use of a ferromagnetic material attached to a force sensor in order to be able to have measurable information, thus all data will be relative to the selected material properties.

A manually operated prototype of an experimental device used for the study of the magnetic field and magnetic force created by axially symmetric neodymium magnet arrangements, was developed in our laboratory [14]. This device was re-designed, upgraded and fully automatized by means of operation and measurement, and will be presented in detail in the following sections.

The experimental device

Construction details about the upgraded experimental device is presented in Fig. 1 and a top view photo is given in Fig. 2.

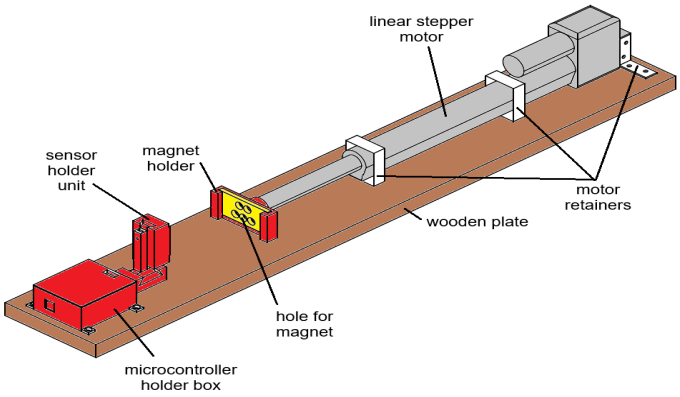

Fig. 1: Schematic drawing of the experimental set-up

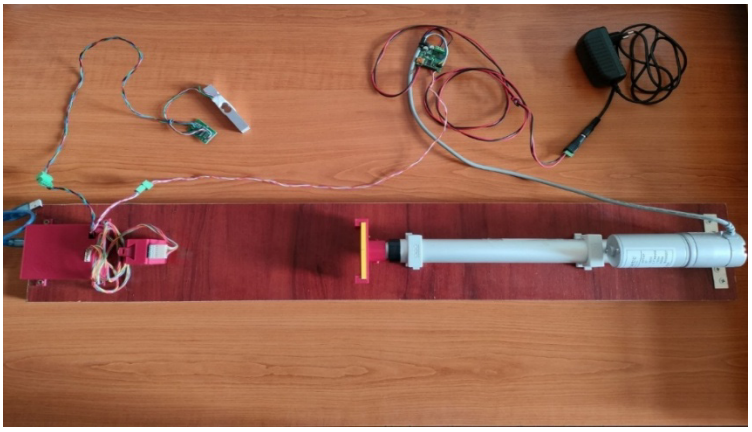

Fig. 2: Top view of the experimental set-up

As one can observe the apparatus is placed on a wooden plate, as it was the prototype too. One major difference is the relative movement. In this device the magnet holder (Fig. 3) is moved, by means of a computer controlled linear motor, towards the highly sensitive sensor which is hold in a fixed position (Fig. 4).

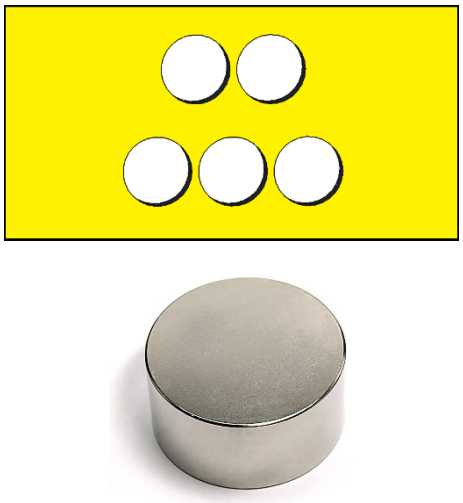

Fig. 3: The magnet holder and the neodymium magnet

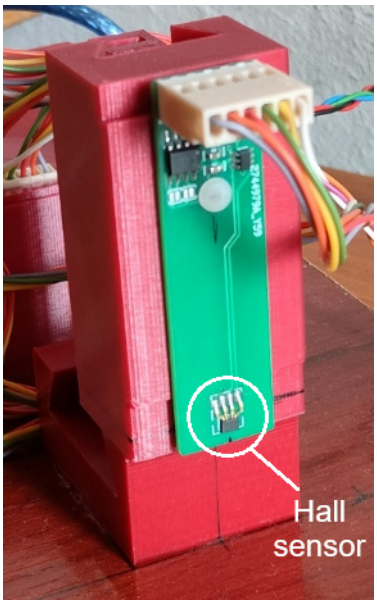

Fig.4: The magnetic sensor and its holder

Construction details about dimensions, materials and implementation are given in [11, 14].

Both device operation and data acquisition are microcontroller driven [15, 16], the user having a LabView [17] interface to operate the set-up. The front panel of the driving and measuring system is presented in Fig. 5., the description of it being presented elsewhere [11].

When started, the code waits for input data, these are: *the total length of the measurements* (in mm) which represent the distance on which the motor will move towards the sensor, *the distance between measurements* (in mm) representing the measurement step and *the number of measurements* in one measuring point. By pressing the *Send* button, a Python code is initiated [11] which creates an array containing all the data necessary for the motor movement and the sensor measurements. This array is returned to LabView and the measurements are initiated.

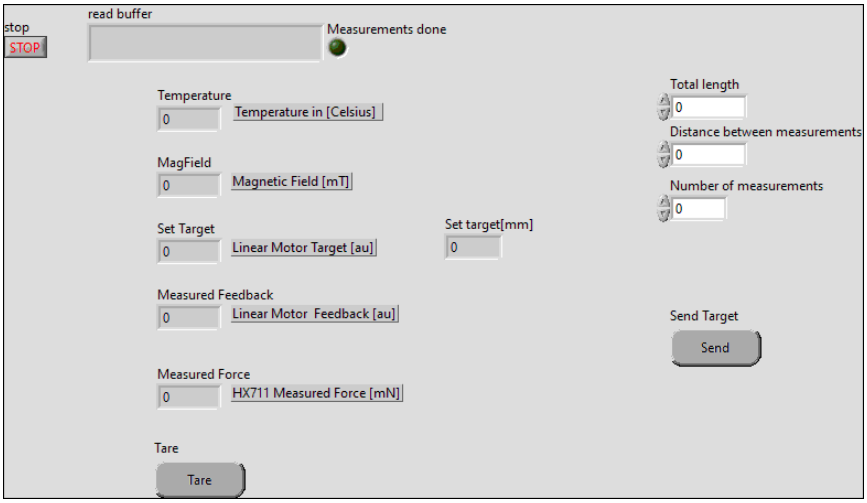

Fig. 5: Front panel of the driving and measuring system

The motor will do all adjustments and move in every position given by the code. In each position the sensor [18] will perform the given number of measurements, their average being stored in a file along with the position. All these steps will be repeated until the holder reaches the last measurement point.

Due to the characteristics of the motor [19], the maximum length on which measurements can be performed is about 2500 motor steps, namely 180 mm.

All programming codes are available in [20].

EXPERIMENTAL RESULTS

The magnetic field created by different magnetic arrangement was studied as function of distance. The dependences for individual, series or parallel arrangement of neodymium magnets have similar shape with those presented in [14]. A comparison of the measurements made by both systems in given in Fig. 6.

As one can see, the advantage of using the upgraded system is obvious (smaller measurement steps - larger number of data) and the results sustain the finding presented in both [11, 14], namely the magnetic sensitive sensor of the Hall probe used for the prototype is not at the end of the rod, but inside.

As a novelty, the antiparallel arrangement was studied. In our situation antiparallel means a parallel connection of two or three magnets where at least one magnet has a different pole side on the measurement side of the system (Fig.7).

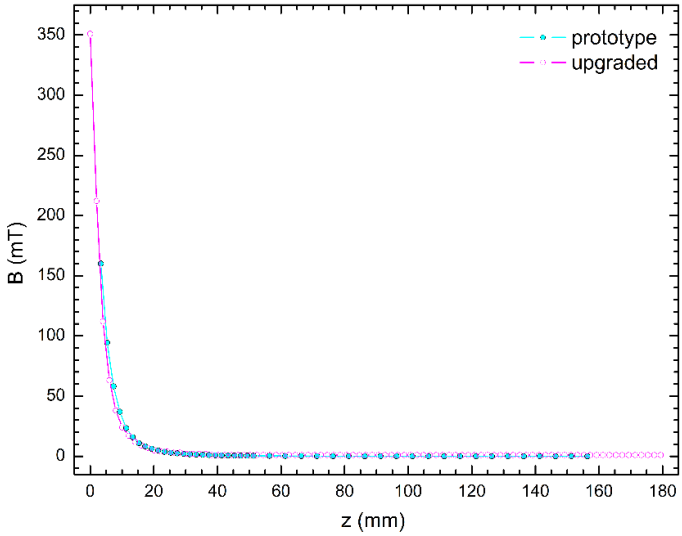

Fig. 6: Upgraded system vs. prototype

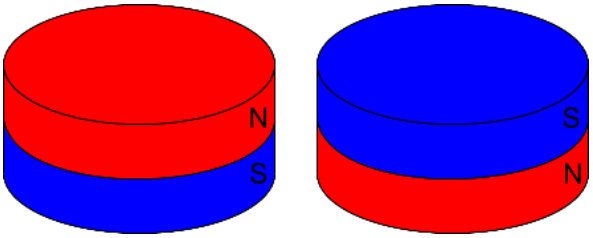

Fig. 7: Illustration of the antiparallel positioning of two magnets

The magnetic field lines as function of distance between magnets, simulated with the *Magpylib* package are [11] presented in Fig. 8.

The orientation of the Hall sensor in our setup is not suitable for this sort of measurements because it can only measure field in the Z direction. Attempts to make measurements along Z axis confirmed this assumption and all the results were only small fluctuation of noisy values due to slight misalignment between the Z axis of the magnet structure and the Z axis of the Hall sensor.

Rotation of the Hall sensor was not an option because several other types of measurements were performed and by modifying the position of the sensor would have made comparison between the results irrelevant.

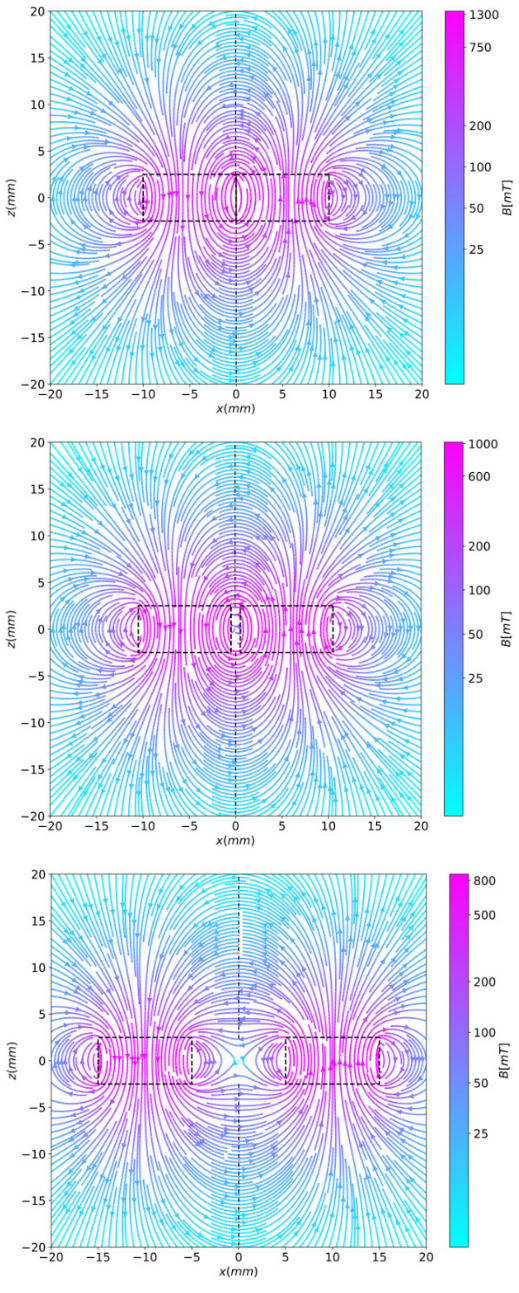

Fig. 8: Simulated magnetic field lines as function of distance between two magnets: (a) 0 mm, (b) 1 mm, (c) 10 mm

Measurements were performed for the antiparallel connection of three magnets and the results are depicted in Fig.9, Fig.10 and Fig.11 respectively.

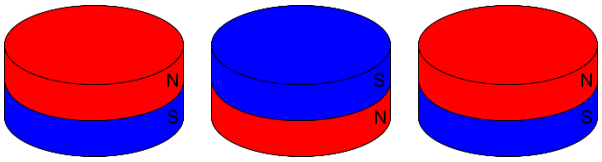

Fig. 9: Illustration of the antiparallel positioning of three magnets

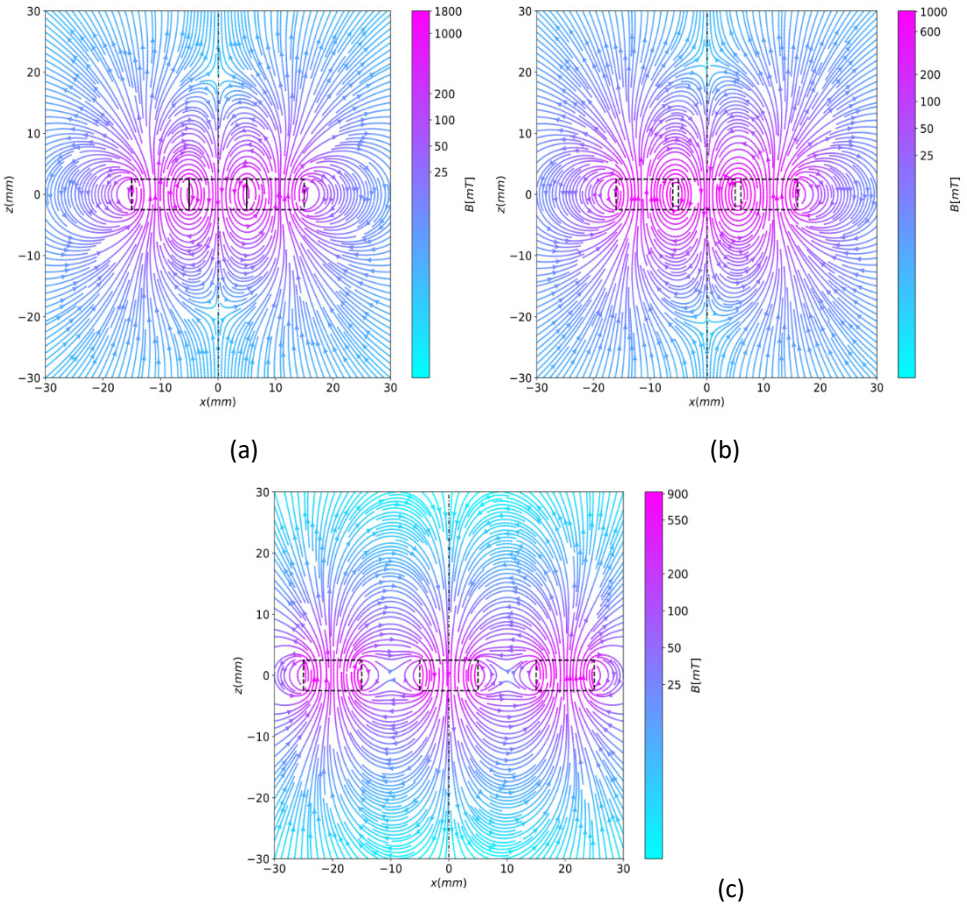

Fig. 10: Simulated magnetic field lines for different distances between three magnets: (a) 0 mm, (b) 1 mm, (c) 10 mm

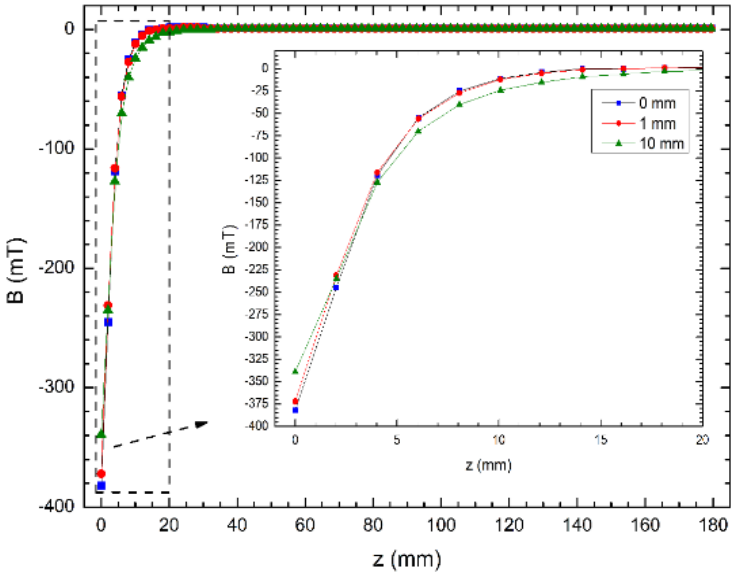

Fig. 11: Variation of magnetic flux density as function of z for three values of the distance between the magnets (0 mm, 1 mm and 10 mm) measured along the z axis in positive direction

In the case of three antiparallel magnets the measurement axis will be the symmetry axis of the system, which coincides with the symmetry axis of the middle magnet. The negative value of the measured field is due to the opposite pole side (South) of this magnet. When the distance between the magnets is 0 mm or 1 mm, the two magnets placed on both sides will enhance the field on the symmetry axis as demonstrated by the simulated field line plots and a more intense field is achieved. Simulation data shows a "zero-field" zone and a direction change in the field at distances around 20 mm. This cannot be pointed out by measurements because at such distances we are near the zone where the value to be measured is around or below sensor resolution or detection limit, respectively.

For 10 mm between magnets the resultant field shows a slightly different dependence with distance, having approximately the same aspect like that of a single magnet. This finding might suggest that, due to arrangement symmetry the contribution of the side magnets is not so relevant (are neglectable) in this case at such distances.

In order to verify these findings, the well-known relationship for the magnetic flux density at an on-axis point, at distance z from the face of an axially magnetized disk-shaped magnet (R radius, D thickness or height) [21-22] was fitted on our experimental data:

$$B(z) = \frac{B_r}{2}\left\{\frac{z+D}{[R^2+(z+D)^2]^{0.5}} - \frac{z}{[R^2+z^2]^{0.5}}\right\}$$

where B_r is the remanence field (value of B on the hysteresis loop, when the magnetizing external field has been removed), it is independent of the magnet's geometry and is given by the manufacturers [23, 24].

The results of the fitting are presented in Fig. 12. As one can observe, for a 10 mm distance between magnets there is a very good correlation between the experimentally measured data, and the fit made by using the formula for a single magnet.

For the 0 mm distance between magnets, the fit made by using the formula for a single magnet (dashed line) is satisfactory too, but there is a better fit using 0.53 in the exponent and not 0.5 like for one magnet, or for a 10 mm distance between magnets. The same findings are found for the 1 mm magnet distance. These later observations could explain the faster decay of the magnetic flux density for 0 and 1 mm as presented in the inset of Fig. 11.

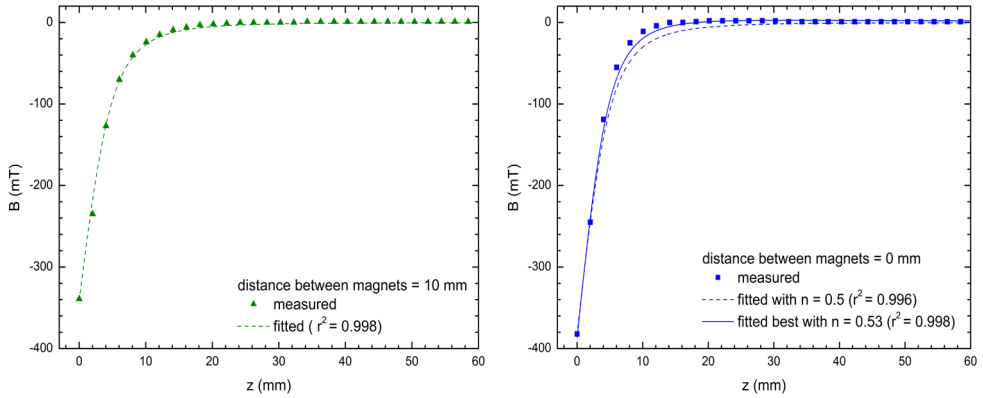

(a) (b)

Fig. 12: Fitting for the variation of magnetic flux density measured along the *z* axis, for different distances between magnets: (a) 10 mm, (b) 0 mm

CONCLUSIONS

The antiparallel coupling of neodymium magnets was studied by means of an upgraded measurement system designed for the study of the magnetic field created by different magnetic arrangements. The microcontroller driven data

acquisition and measurement system and the linear stepper motor are excellent tools in performing precise and accurate experimental measurements.

The project was an important diagnostic tool for the students' performances and skills, and it was successfully presented at the final graduation exam.

REFERENCES

[1.] P. Granum, M. Linnet Madsen, J. T. Kerr McKenna, D. L. Hodgkinson, J. Fajans, Nuclear Inst. and Methods in Physics Research, A 1034 (2022) 166706
[2.] M. Ortner, L. G. Coliado Bandeira, SoftwareX 11 (2020) 100466
[3.] C. Treutler, "Magnetic sensors for automotive applications," Sensors and Actuators A: Physical, vol. 91, no. 1, pp. 2–6, 2001, 3rd European Conference on Magnetic Sensors & Actuators.
[4.] K. Sakamoto, Y. Iwaji, T. Endo, T. Taniguchi, T. Niki, M. Kawamata, and A. Kawamura, Power Conversion Conference-Nagoya. IEEE, 2007, pp. 1119–1125.
[5.] M. Riley, A. Walmsley, J. Speight, and I. Harris, Materials science and technology, vol. 18, no. 1, pp. 1–12, 2002.
[6.] J. M. D. Coey - Magnetism and Magnetic Materials-Cambridge University Press (2010)
[7.] J. Mallinson, IEEE Trans. Magn. 9, 678 (1973).
[8.] K. Halbach, IEEE Trans. Nucl. Sci. 26, 3882 (1979).
[9.] K. Halbach, Nucl. Instrum. Methods 169, 1 (1980).
[10.] K. Halbach, J. Appl. Phys. 57, 3605 (1985).
[11.] K. Bodó, "Experimental set-up for the study of the magnetic field created by axially symmetric permanent magnet arrangements" BSc Thesis, Engineering Physics, Faculty of Physics, Babes-Bolyai University, Romania, July 2023.
[12.] S.R. Trout, Proceedings of EMCW, 1-7, 2000
[13.] Standard specifications for permanent magnetic materials (MMPA STANDARD No. 0100-00) https://allianceorg.com/pdfs/MMPA_0100-00.pdf (accessed November 2022)
[14.] A. R. Tunyagi, K. Bodó, A. Simon, Rom. Rep. Phys. 75, 910 (2023)
[15.] Arduino Uno, https://store.arduino.cc/arduino-uno-rev3 (accessed October 2022)
[16.] https://reference.arduino.cc/reference/en/language/functions/advanced-io/pulsein/ (accessed October 2021)
[17.] Linear High Precision Analog Hall Sensor 144. URL: https://www.asensor.eu/onewebmedia/Datasheet-HE144X.pdf (accessed January 2023)
[18.] Glideforce linear actuator light duty series. https://www.pololu.com/file/0J1238/LDLinear-Actuator-Data-Sheet-201208.pdf (accessed January 2023)
[19.] What is LabVIEW? https://www.ni.com/en-gb/shop/labview.html (accessed January 2023)

[20.] Magnetic field mapping system for permanent magnet arrangements: phys.ubbcluj.ro/~alpar.simon/codes/magnets
[21.] J.M. Camacho and V. Sosa, Revista Mexicana de Fisica E, 59, 8-1 (2013).
[22.] K. Kaphle, G. Karki, and A. Panthi, Journal of the Institute of Engineering, 15, 150-160 (2020).
[23.] https://www.kjmagnetics.com/specs.asp (accessed March 2023)
[24.] https://www.supermagnete.de/eng/physical-magnet-data (accessed March 2023)

STUDIA UBB PHYSICA, Vol. 68 (LXVIII), 1-2, 2023, pp. 25-38
(RECOMMENDED CITATION)
doi:10.24193/subbphys.2023.03

A COMPARISON OF COMPUTATIONAL FLUID DYNAMICS TURBULENCE MODELS FOR DIFFERENT REYNOLDS NUMBERS FLOWS

K. GERGŐ[1,2], V. REDNIC[1], R.V.F. TURCU[1,3*]

ABSTRACT. The present research was made to improve the engineering perspective concerning the computational fluid dynamics method. The main purpose is to obtain the limits of different turbulence models and to establish which of them is the most suitable for different Reynolds number flows. The flow configuration was a typical one, named backward facing step, which is widely used to investigate flows experimentally and computationally. The study involves multiple stages, from creating the geometry and meshing the experimental model to simulating all the conditions to obtain sufficient data to compare the turbulence fluid flow models with experimental results.

Keywords: *backward facing step, turbulence models, atomization, CFD, fluid flow, Reynolds-number*

INTRODUCTION

Computational fluid dynamics (CFD) is a very powerful tool for technological development engineering since it makes easier, cheaper and more time efficient the process of taking measurements. The method is based on a computational,

[1] *National Institute for Research and Development of Isotopic and Molecular Technologies, Center of Advanced Research and Technologies for Alternative Energies (CETATEA), Donat 67-103, Cluj-Napoca, Romania.*
[2] *Technical University of Cluj-Napoca, Faculty of Electronics, Telecommunications and Information Technology, 26-28 George Barițiu str., 400027 Cluj-Napoca, Romania.*
[3] *Babeş-Bolyai University, Faculty of Physics, 1 Kogălniceanu str., 400084 Cluj-Napoca, Romania.*
[*] *Corresponding author: flaviu.turcu@ubbcluj.ro*

iterative process. The main point is to approximate the propagation of different physical phenomena in a pre-defined system.

CFD was introduced in technological development in the 1970s, when the first commercial software packages were developed.[1] These early programs were limited by the available computing power, and could only handle relatively simple two-dimensional problems. As computing power increased in the following decades, so did the capabilities of CFD. Three-dimensional models became common, and more complex problems could be analyzed. This led to the adoption of CFD in a variety of industries, including aerospace, automotive, and energy. For example, CFD simulations are used extensively in car racing for designing the aerodynamics of the car, optimizing the airflow over certain geometrically designed shapes, and improving the cars performance. CFD models are also used to predict the car's behavior under different driving conditions and to evaluate new designs before they are physically tested.

Preparing a CFD analysis involves multiple stages of pre-processing and post-processing. These stages, presented in the Results and Disscussions section.

An important quantity in CFD simulations which is involed in the present study as well is the **Reynolds number**. The Reynolds number is a dimensionless parameter used in fluid mechanics to characterize the behavior of a fluid flow. The Reynolds number (Re) is defined as the ratio of inertial forces to viscous forces within a fluid flow. It can be expressed mathematically as:

$$Re = \rho \frac{vL}{\mu}$$

where ρ is the density of the fluid, v is the velocity of the flow, L is a characteristic length scale (such as the diameter of a pipe or the chord length of an airfoil), and μ is the dynamic viscosity of the fluid. The Reynolds number has the same value for all fluid flows that have the same geometric shape and the same fluid properties. The value of the Reynolds number determines the type of flow regime that exists within the fluid flow. At low Reynolds numbers (typically less than 2000), the flow is laminar, meaning that the fluid flows in smooth, parallel layers without turbulence. At high Reynolds numbers (typically greater than 6000), the flow becomes turbulent, meaning that the fluid flows in a chaotic, unpredictable with eddies and vortices forming within the flow. Between 2000-6000 **Reynolds number (Re)** values, there is a transitional regime, in which vortices form and dissipate quickly. [2]

The Reynolds number is an important parameter in many areas of fluid mechanics, including aerodynamics, hydrodynamics, and heat transfer. It is used to predict the onset of turbulence, to design and optimize fluid flow systems, and to compare different fluid flow configurations. It is a key parameter in the design of many engineering systems, such as pipelines, pumps, and aircraft.

Fluid flow models

There are a lot of choices for fluid flow models. A CFD engineer should know the advantages and disadvantages of each in order to create a proper model for a certain phenomena. The following chapter will contain a brief description of the most widely used fluid flow models:

Inviscid flow is a type of fluid flow where the fluid is assumed to have zero viscosity, meaning that it has no internal friction. Inviscid flow is an idealized model that is used to simplify the analysis of fluid dynamics problems, especially in aerodynamics and assumes that the fluid is homogeneous and the flow is non-rotational, meaning that the fluid particles move in straight lines and do not rotate around their own axis. It is often used to analyze the flow of fluids around solid objects, such as wings, propellers, and airfoils.

Laminar flow, on the other hand, is a type of fluid flow where the fluid particles move in parallel layers or streams, with minimal mixing between them. Laminar flow occurs when the fluid is moving at low velocities, and the flow is characterized by smooth, steady motion. Laminar flow is often observed in small channels and pipes, and it is important in the design of fluid handling systems. Laminar flow is often modeled using the Navier-Stokes equations, which describe the behavior of viscous fluids. There are other models that reflect much better the behaviour of certain flows based on the Reynolds Averaged Navier-Stokes (RANS) equations, which are used to solve for the time-averaged flow field.

The **k-epsilon model** is a two-equation model, which solves for the turbulent kinetic energy (k) and the dissipation rate of turbulent kinetic energy (epsilon). The k-epsilon model assumes that the turbulence is isotropic and that the eddies in the flow are small and rapidly decaying. This model is suitable for moderate Reynolds number flows where the turbulence is not very intense.

The k-epsilon model is computationally less expensive than the k-omega model. The model is relatively easier to set up and calibrate and it is more suitable for low-to-moderate Reynolds number flows where the turbulence is not very intense. The k-epsilon model assumes isotropic turbulence, which may not be appropriate for all flow situations. The model is less accurate in predicting separated flows, flow separation, and swirling flows. It can also produce unphysical results in cases where the turbulence is anisotropic, such as in flows with strong curvature or rotation.

The **k-omega model** is also a two-equation model that solves for the turbulent kinetic energy (k) and the specific dissipation rate (omega). The k-omega model assumes that the turbulence is anisotropic and that the eddies in the flow are larger

and less rapidly decaying than in the k-epsilon model. This model is suitable for high Reynolds number flows where the turbulence is intense.

The k-omega model is more accurate than the k-epsilon model in predicting turbulent flows with intense anisotropy, such as those involving swirling flows or strong curvature. The model is also better suited for high Reynolds number flows where the turbulence is more intense and it can better capture the effect of pressure gradients on the turbulence, which is important in many engineering applications.

The k-omega model is more computationally expensive than the k-epsilon model, it is more difficult to set up and requires more calibration. The model may be less accurate in predicting laminar-turbulent transition and wall-bounded flows. The main difference between the two models is in their treatment of the dissipation rate of turbulent kinetic energy. In the k-epsilon model, the dissipation rate is calculated using an empirical formula that assumes a constant ratio between the length scale of turbulence and the dissipation rate. In the k-omega model, the specific dissipation rate is directly related to the turbulent viscosity, which is determined by solving a transport equation for omega.

Overall, both models have their own advantages and limitations, and the choice of model depends on the specific flow conditions and the desired level of accuracy.

The aim of this paper is to present the general path of building a CFD model for a physical phenomena and to compare the results obtained by using turbulence fluid flow models available in today's CFD technologies with experimental data.

THEORETICAL DETAILES

Until this point we presented various turbulence simulation models for a certain phenomena. One of the main steps of setting up a proper model in CFD technology is to select the proper fluid-flow model that fits best the parameters of the flow in cause. For example, there are models that go well with high-turbulence flows but are expensive comupationally. If you have a simple non-viscous fluid that has low flow velocity, the best reccomendation is to use a laminar model that goes well with this kind of phenomena and converges relatively fast. The setup (geometry) used for this present research is named backward facing step. It's a simple geometry but it's also suitable to study turbulent flows in different conditions.

A **backward facing step** is a flow configuration in which a fluid flows in a channel or duct and encounters a sudden expansion, which creates a step-like geometry with a vertical wall facing upstream and a horizontal wall downstream.

The fluid flow is said to be backward facing because the direction of the flow is opposite to the direction of the step.

When the fluid flows through the narrow channel before the step, it accelerates and develops a boundary layer near the walls. As the flow encounters the step, the sudden expansion causes the flow to slow down and the boundary layer to thicken. This results in the formation of a recirculation region downstream of the step, where the fluid flows back towards the step before turning downstream again. The backward facing step is a common flow configuration used in experimental and numerical studies to investigate fluid dynamics phenomena such as turbulence, boundary layer separation, and heat transfer. It is also relevant to many engineering applications, such as in the design of heat exchangers and combustion systems.

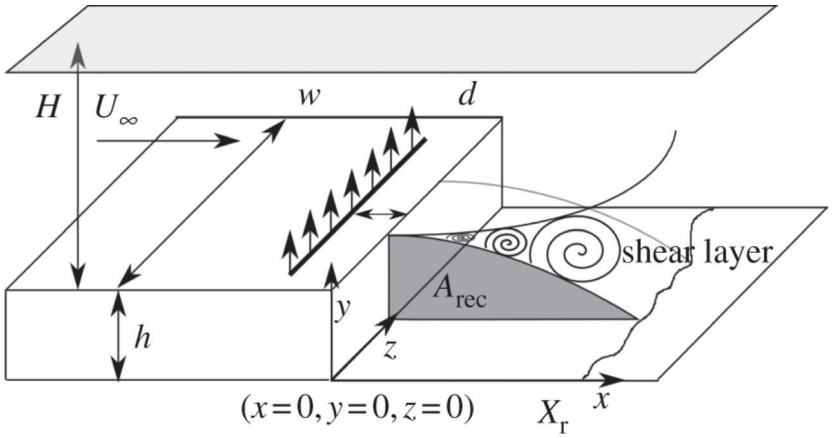

Fig. 1: Backward facing step geometry and parameters [3]

As the duct thickens and the fluid passes through the „step", an inverse flow domain forms right beside the step. This study will compare the X_r (**Fig. 1**) values obtained from simulations with real experimental data. The source for experimental data is [4], (**Fig**. **2)**. The x-axis value is the Reynolds number of the flow mesured right before the flow passes the step,vertically in the middle of the duct. X_r is the lenght of inverse flow domain, but it's represented in dimensionless units X_r/H, H being the height of the step. In this case H=1.5 cm.

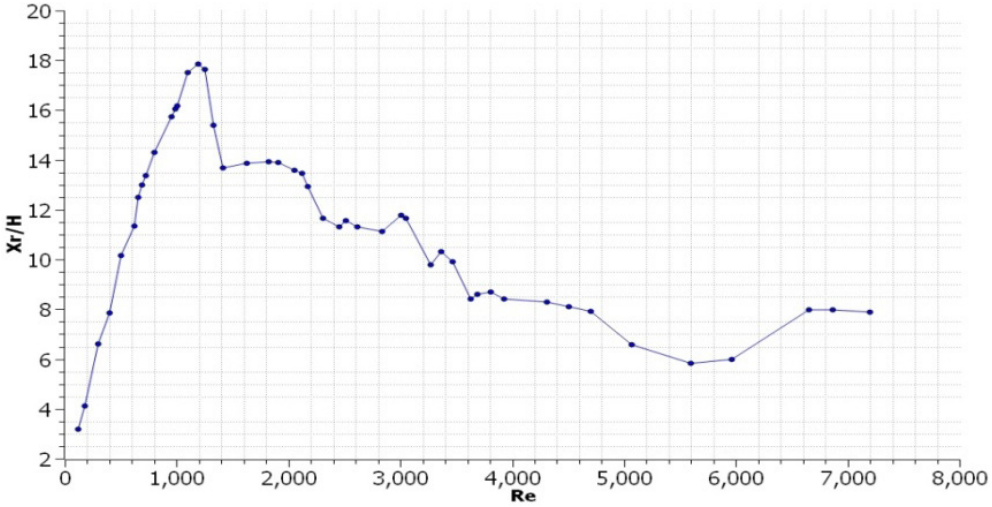

Fig. 2: The length of the inverse flow domain as a function of Reynolds number of the flow before the step [4]

RESULTS AND DISCUSSION

In the following pharagraph, we will present the steps of building a CFD model, illustrating each step with the model built for this research.

The first step is to build a **geometry** using a CAD (computer-aided design) software. Making a geometry assumes only designing the appearance of the studied object without defining the physical properties of the material. In this case, we will build the simple 2D geometry of the backward facing step presented previously.

The next step is to **mesh** the geometry as a preceding operation of the calculations. Meshing is the process of dividing a physical domain, such as an object or fluid volume, into a finite number of small elements known as “meshes” or “elements.” The meshes are usually simple geometric shapes, such as triangles, quadrilaterals, tetrahedra, or hexahedra, that collectively form a complex representation of the original physical domain.

The mesh has two undimensional quantities that caracterizes its quality: skewness and ortogonality. Skewness refers to the distortion or non-uniformity of the mesh elements. Ideally, mesh elements should be as regular as possible, with uniform angles between their faces. However, in practice, mesh elements can become distorted, resulting in non-uniform angles between their faces. Skewness can negatively impact the accuracy and stability of the simulation results, as it can cause numerical errors and convergence problems. Therefore, it is desirable to

keep the skewness of mesh elements as low as possible. Orthogonality, on the other hand, refers to the degree to which mesh elements are perpendicular to each other. In an ideal mesh, all elements should be perfectly orthogonal to their neighboring elements. However, in practice, orthogonality can be compromised due to the geometry of the physical domain or the meshing algorithm. Non-orthogonal elements can lead to inaccurate flow predictions and numerical instabilities in CFD simulations, especially in regions of high flow gradients. Therefore, it is important to maintain a high degree of orthogonality in the mesh, especially in regions where accurate flow predictions are crucial.

The mesh size and shape are determined by several factors, including the geometry of the physical domain, the desired level of accuracy, the available computational resources, and the type of analysis being performed. A fine mesh with small elements can provide more accurate results, but at the cost of increased computational resources and longer simulation times. A coarser mesh with larger elements can provide faster results, but with lower accuracy. The process of meshing involves generating the mesh, refining or coarsening it as needed, and then exporting it to the appropriate simulation software. Meshing can be done manually, but for complex geometries, automated meshing tools are typically used.

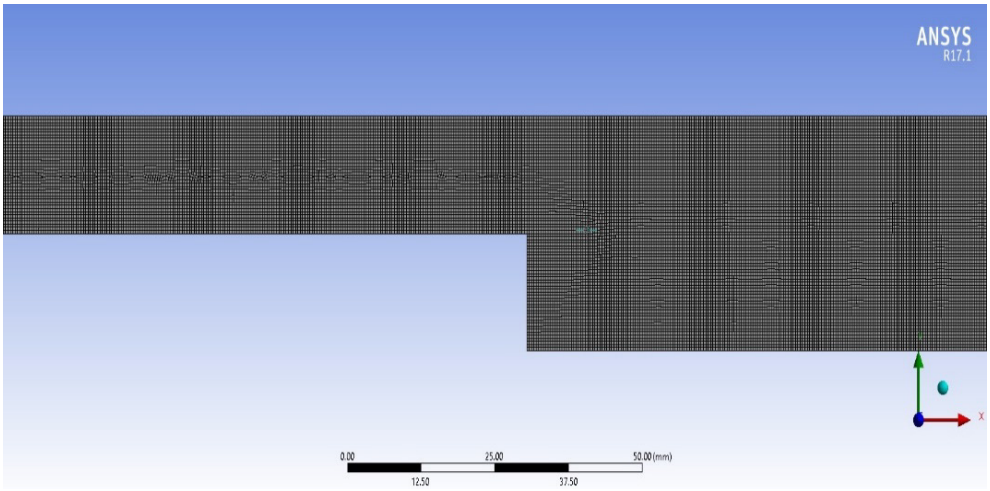

Fig. 3: The meshed form of the backward facing step geometry

The meshing for this simple geometry is represented in **Fig. 3** completed with mesh quality parameters. Orthogonality is a value near to 1 and skewness to 0. It indicates that we realized a decent mesh to run the simulation on.

Pre-processing is the initial stage of a simulation process, which involves setting up the problem, preparing the input data, and creating a numerical model to represent the physical system to be analyzed. It has two main stages:

1. Boundary conditions: Once the mesh is created, boundary conditions must be defined for the simulation. This includes specifying the inflow and outflow boundaries, the wall boundaries, the type of fluid being simulated, and any other relevant physical properties. The boundary conditions are essential for defining the initial conditions of the simulation.
2. Solver Settings: The solver settings must be defined before running the simulation. This includes the choice of solver, the numerical method used to solve the governing equations, and the convergence criteria. The solver settings must be selected to ensure that the simulation results are both accurate and efficient.

Generally, in CFD the **calculations** executed by the solver are differential equations, but solved numerically with a certain error value. These errors, called residuals, should be minimized to meet the convergence criteria. A graphical representation of this process is shown in **Fig. 4**.

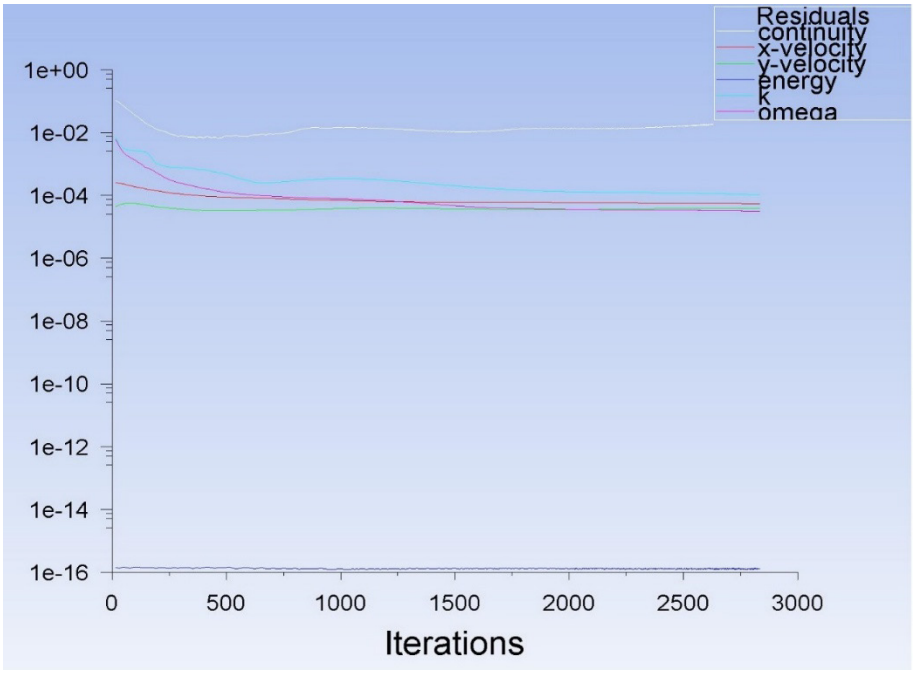

Fig. 4: Evolution of residual values for backward facing step model calculations

The convergence is an essential part of a model. A simulation works with repetitive calculations which assumes minimizing the residual values throughout the iterations. Reaching the convergence criteria means making the residual values smaller than a certain value. Residuals are a measure of the error in the numerical solution of the governing equations. The rate of decrease of the residual values is a measure of the convergence rate of the simulation. In general, the goal of a CFD simulation is to obtain a numerical solution that is both accurate and time efficient. The accuracy of the solution depends on the convergence criteria used, while the efficiency of the solution depends on the rate of convergence. A good convergence criterion should ensure that the solution is accurate enough to meet the desired level of precision while still allowing the simulation to converge in a reasonable amount of time.

In fluid dynamics simulations the most typical and wide applicable set of differential equations is the Navier-Stokes system. The Navier-Stokes equations are a set of partial differential equations that describe the motion of fluids, including liquids and gases [5]. The Navier-Stokes equations describe the fundamental laws of fluid mechanics, including the conservation of mass, momentum, and energy. They take into account the effects of viscosity, pressure, and gravity on the fluid motion.

The general form of the Navier-Stokes equations can be written as:

$$\frac{\partial u}{\partial t} + u \cdot \nabla u = -\frac{\nabla p}{\rho} + \nu \cdot \nabla^2 u + g$$

$\boldsymbol{\frac{\partial u}{\partial t}}$ represents the acceleration of the fluid, $\boldsymbol{u \cdot \nabla u}$ represents the convective acceleration due to the motion of the fluid. $-\boldsymbol{\frac{\nabla p}{\rho}}$ represents the pressure forces, while g represents the viscous forces. The last term represents the effect of gravity on the fluid.

The Navier-Stokes equations are a system of coupled, nonlinear partial differential equations that are difficult to solve analytically. Instead, numerical methods are used to solve them in practice [6].

Post-processing typically involves the following steps:

The first step in post-processing is to extract the data generated by the simulation. This data may include the velocity, pressure, temperature, and other variables at various locations within the simulated domain. The data can be extracted from the output files generated during the simulation and stored in a format that can be easily processed and analyzed. Once the data is extracted, it must be analyzed to identify any patterns or trends that may be relevant to the problem being studied. This can be done using various statistical and data analysis

techniques. For example, contour plots, velocity vectors, streamlines, and other visualizations can be used to understand the flow patterns and other features of the system. Post-processing also involves validation and verification of the simulation results. Validation is the process of comparing the simulation results to experimental data to ensure that the simulation accurately represents the physical system being studied. Verification is the process of ensuring that the simulation is solving the correct equations and is providing a reliable solution.

In this particular case, the post-processing consists of gathering data about the lenght of the backflow domain named X_r previously. The data extraction took place by representing the shear force (**Fig. 6**) of the swirl (**Fig. 5**) acting upon the lower wall and reading the coordinate when the horizontal shear force becomes positive again.

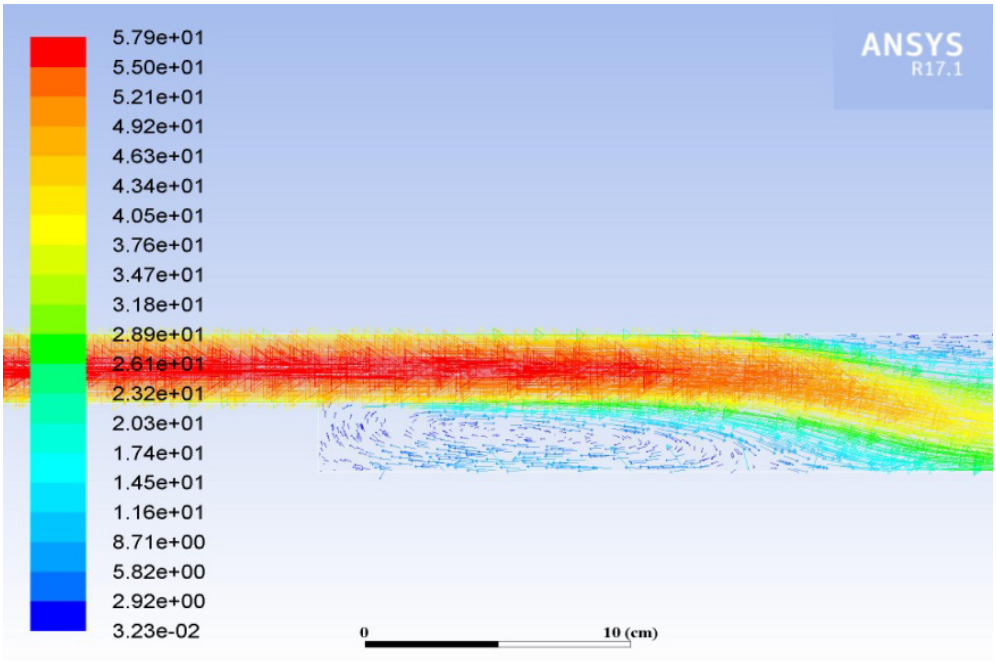

Fig. 5: Velocity vectors of the flow in the pipe in the proximity of the step

The measurements were taken this way, simulating the flow for every Reynolds number and reading the data point when the shear becomes again positive (red dot on **Fig 6**). In this case negative shear means back flow and positive shear forward flow.

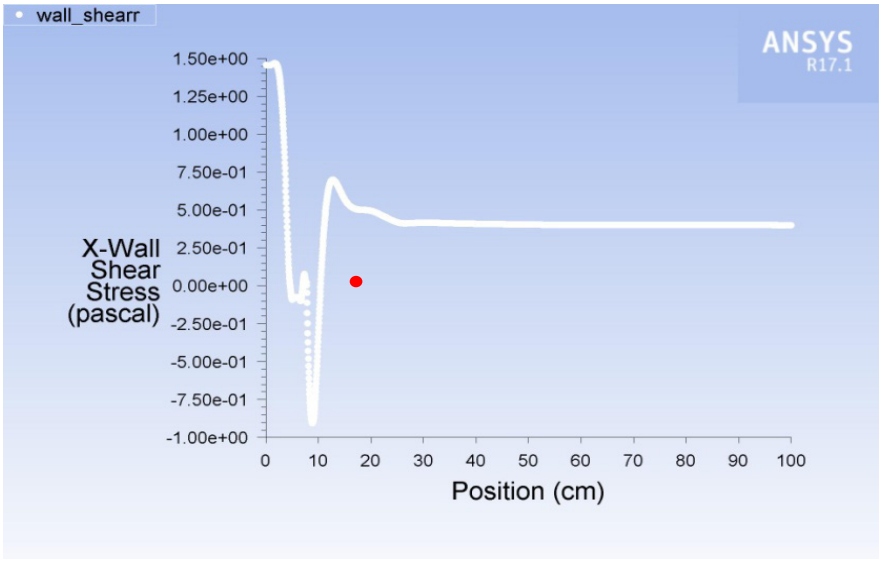

Fig. 6: The horizontal component of the shear-force on the lower wall of the geometry

The results of the CFD simulations in the 20-8000 Re range, including laminar, transitional and turbulent regimes, are presented in **Fig. 7** for both k-epsilon and k-omega models. The CFD results are compared with the experimental ones.

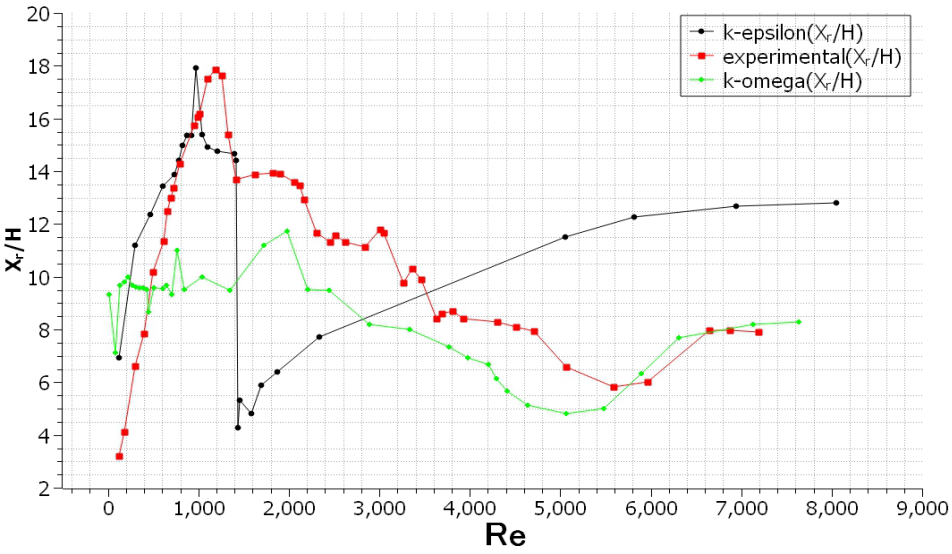

Fig. 7: Comparison between the computational and experimental [4] results

Experimentally, the behaviour of the curves varies in respect with the regime of the flow. For Re<1000, the air flow can be considered laminar. In this interval the lenght of the backflow domain grows linearly with the Reynolds number. In transitional flow regime (Re 2000-6000), the lenght X_r tends to decrease until it reaches a minimum value. Afterwards it has a tendency to grow and to stabilize at a constant value. Reaching the interval when the size of the backflow domain doesn't change anymore with the Reynolds number, means that the flow became turbulent. This behavior takes place for Re>6000. Taking into account the concordance of the curves, we can notice that the k-epsilon model works well with laminar regime but doesn't describe so well transitional and turbulent regimes. As well, we can notice that the k-omega model works well with transitional and turbulent regimes but fails to describe the laminar regime.

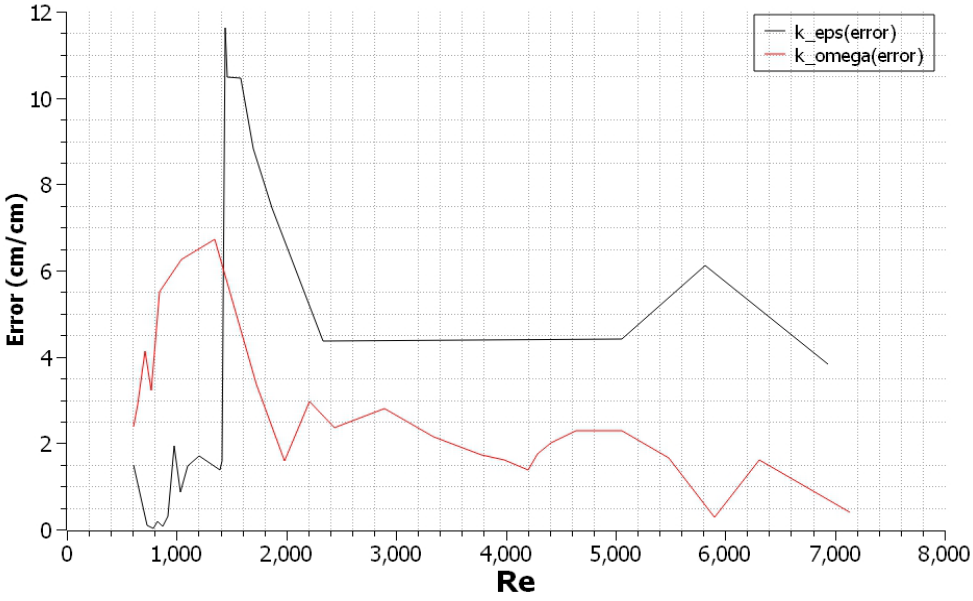

Fig. 8: Absolute errors in respect to experimental curve for both models

On **Fig. 8** is represented the error for both models compared with experimental data. As it can be noticed, the k-epsilon model has smaller errors in the laminar regime (Re<1000) and the k-omega has smaller errors in the transitional and turbulent regimes (Re>1000).

CONCLUSIONS

In conclusion, based on the obtained data can be confirmed that creating a suitable model for a physical phenomenon is strongly influenced by the proper selection of fluid flow model. For laminar and low transitional regime (Re < 1500) k-epsilon model performs very well but afterwards, not even the tendency of evolution of X_r matches the experimental results. Besides, on transitional regime k-omega tends to overperform k-epsilon, as it reflects the decreasing tendency of X_r. On turbulent regime the best choice is obviously k-omega because it predicts correctly the constant value at which the X_r stabilizes. K-epsilon also predicts a constant value for this regime, but with significantly higher error.

This research gives evidence of the fact that using two different fluid flow models can give very different results at the end. Of course, these results don't give a one hundred percent precise guideline of turbulence model selection for every kind of flow but can significantly help the CFD engineers upon taking this decision.

ACKNOWLEDGMENTS

This project is funded by the Ministry of Research, Innovation and Digitalization through Programme 1 - Development of the National Research and Development System, Subprogramme 1.2 - Institutional Performance - Funding Projects for Excellence in RDI, Contract No.37PFE/30.12.2021 and the "Nucleu" Programe within the National Plan for Research, Development and Innovation 2022-2027, project PN 23 24 02 01.

REFERENCES

1. Yufeng Wei, "The development and application of CFD technology in mechanical engineering", **2017**, IOP Conf. Ser.: Mater. Sci. Eng. 274 012012
2. Vaclav Uruba, "Reynolds number in laminar flows and in turbulence", **2019**, AIP Conference Proceedings 2118(1):020003, 38th meeting of departments of fluid mechanics and thermodynamics
3. Gautier N. and Aider J.-L. Control of the separated flow downstream of a backward-facing step using visual feedback Proc. R. Soc. A.46920130404, **2013**
4. F. Armalyt, F. Dursts, J. C. F. Pereira and B. Schonung: "Experimental and theoretical investigation of backward-facing step flow", **1983**, J. Fluid Mech., vol. 127, pp. 473496

5. Giovanni P. Galdi, “An Introduction to the Navier-Stokes Initial-Boundary Value Problem”, **2000**, Part of the Advances in Mathematical Fluid Mechanics book series (AMFM)
6. M. Ahammad, M. A. Rahman, J. Alam, S. Butt, “A computational fluid dynamics investigation of the flow behavior near a wellbore using three-dimensional Navier–Stokes equations”, **2019**, Advances in Mechanical Engineering 11(9)

STUDIA UBB PHYSICA, Vol. 68 (LXVIII), 1-2, 2023, pp. 39-48
(RECOMMENDED CITATION)
doi:10.24193/subbphys.2023.04

A COMPREHENSIVE REVIEW OF FABRICATION AND CHARACTERIZATION METHODS OF HYDROXYAPATITE

C. LUNG[1*], D. MARCONI[1,2*], T. FEHER[1*]

ABSTRACT. This synthesis article expands on the applications of hydroxyapatite (HA) coatings on titanium dioxide (TiO_2) substrates for biomedical applications, focusing on the methods of deposition and their impact on the material's properties. Various techniques, including sol-gel, electrochemical deposition and ultrasonic spray-pyrolysis are discussed because of their ability to enhance the mechanical resistance, biocompatibility and osteointegration of implants. The analysis methods used are X-Ray Diffraction (XRD), Scanning electron Microscopy (SEM) and Fourier Transform Infrared Spectroscopy (FTIR). They provide insights into the structural, chemical and physical characteristics of the HA coatings. The results indicate that these hybrid coatings significantly improve the performance and longevity of implants in orthopedic and dental applications.

Keywords: *Hydroxyapatite, Titanium Dioxide, Biomedicine, biocompatibility, Osteointegration, Sol-Gel dip-coating, Electrochemical Deposition, Ultrasonic Spray Pyrolysis, X-Ray Diffraction, Scanning Electron Microscopy, Fourier Transform Infrared Spectroscopy, hybrid coatings*

INTRODUCTION

Biomaterials are on the receiving end of a great deal of attention in the scientific community because a suitable biomaterial is capable of replacing, rebuilding and restructuring human tissue for long term use, without an excess of negative effects, whether they be toxic or inflammatory [1]. In applications such as bones replacements we are often looking for a material that will offer the appropriate

[1] *Babes-Bolyai University, Physics Faculty, M. Kogălniceanu No. 1, 400084, Cluj-Napoca, Romania.*
[2] *Department of Molecular and Biomolecular Physics, National Institute for Research and Development of Isotopic and Molecular Technologies, Cluj-Napoca, Romania.*
[*] *Corresponding authors: claudiu.lung@ubbcluj.ro, daniel.marconi@itim-cj.ro, tudorfeher@gmail.com*

balance between good mechanical resistance and good biological properties [2] In the following synthesis article, we will present past studies that included the use of titania (TiO_2) as substrate, together with a hydroxyapatite (HA) coating.

Such thin coatings present a good biocompatibility, bioactivity and osteoconductivity, which makes them ideal for improving the properties of implants used in orthopedy or stomatology [3]. Deposition methods influence the structure, properties and performance of thin layers with biomedical applications. Out of the broad range of deposition methods that are used at the moment, each one of them present their own advantages and challenges that allow us to use them in various applications in which we [4] will give the thin layers the properties that we need [1].

Next, we will discuss simple and hybrid layers of hydroxyapatite, several deposition methods, such as the sol-gel, electrochemical deposition and ultrasonic spray pyrolysis methods. We will also delve into the characteristic of analysis methods: X-Ray diffraction (XRD), Scanning Electron Microscopy (SEM) paired with energy dispersive X-Ray analysis (EDX) and Fourier Transform Infra-Red Spectroscopy (FTIR).

LITERATURE STUDY

The selection of the deposition methods depends in the range of applications that we require for the thin layer and on the properties of the deposited materials. For biomedical applications, the roughness of the titanium surfaces plays a major role in adhesion with the bone tissue [4]. It is proven that matching the roughness of the surface of the implant results in an improvement of the mechanical proprieties of the bone-implant interface, compared to a smoother surface. Furthermore, this offers a greater porosity that will improve the osteointegration between the bone and the implant [5].

Hydroxyapatite thin layers have been studied in the context of a single substrate or in the one of a hybrid substrate that has multiple constituents in its composition. There are many studies that investigate the deposition of hybrid layers on titanium substrates. It was discovered that hybrid thin layers can be deposited successfully, without traces of foreign contaminants. Titanium Oxide, which is the protective layer that naturally occurs on titanium was created, in this instance, by micro arc oxidation and the hydroxyapatite was deposited through plasma electrolysis and gel electrophoresis [2].

Literature findings have shown that a hybrid combination of the two aforementioned deposition techniques can give pure hydroxyapatite from a stoichiometric perspective on the outside layer and an intermediate layer of Titanium Oxide [6], that offers the appropriate mechanical properties and a good biostability, in the

corrosive environment of the human body [7]. Another advantage of a hybrid substrate is the improvement of the osteoblastic activity of titanium implants, respectively the capability of improving the capability of improving the activity and the proliferation of the osteoblastic cells in the human body, that are responsible with the regeneration of bone tissue [2]

For us to further elaborate this synthesis article on the theme of deposition oh thin layers of hydroxyapatite on titania substrates, we will discuss the specifical details presented in the literature, respectively deposition methods and analysis methods.

Ultrasonic Spray Pyrolysis for Hydroxyapatite Deposition

The ultrasound spray pyrolysis method stands out among others as a promising method of deposition of HA thin films on TiO_2 substrates due to her ability to produce layers that are homogenous and have a controlled thickness and composition. The method consists in the atomization of a precursor substance in fine droplets, that are then further transported by a carrier gas on the heated substrate where they undergo the process of pyrolytic decomposition and form a solid thin layer [3]. This allows for a precise control on the chemical and phasic composition of the deposited films, thus improving the limitations of the plasma deposition techniques, that often suffer of a poor stoichiometry of the sample and of inhomogeneous phases of HA. The deposition parameters such as the concentration of the precursor solution, the temperature of the substrate and the deposition time are meticulously controlled to optimize the properties of the film [8].

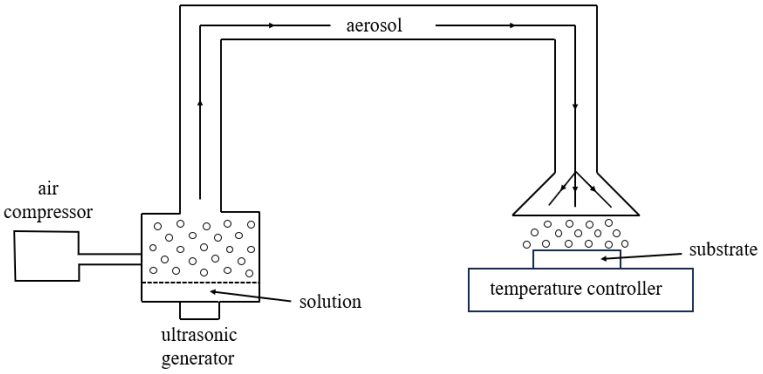

Fig. 1: Schematic of Ultrasonic Spray Pyrolysis coating method

Among the advantages that were mentioned above, the method has its' own specific limitations. One of them is the necesary thoroughness and meticulosity in the preparation of a precursor substance. It is important for it to display an appropriate degree of viscosity to ensure an efficient vaporization, but too great of a viscosity might cause the vaporizer to jam [8]. Another limitation is the difficulty in obtaining a uniform layer on a substrate of large dimensions and irregular surface [3], as the variation of the diameter of the droplets and the homogeneity of the flow of the gas can lead to non-uniform areas of the thin film [8].

Sol-Gel method for HA deposition

The Sol-Gel method is a chemical deposition method used to create solid materials out of molecules suspended in a solution as precursors. The process consists of the transition of a liquid system that takes the name of "sol" into a solid substance, the "gel". In the case of HA, the precursors are generally calcium and phosphates, which are dissolved in a solvent, together with a catalyzing agent that has the role of forming bonds with the precursor ions in order to prevent the precipitation or premature conglomeration. Moreover, the adjusting of the concentration of the sol can increase or decrease the deposition time.

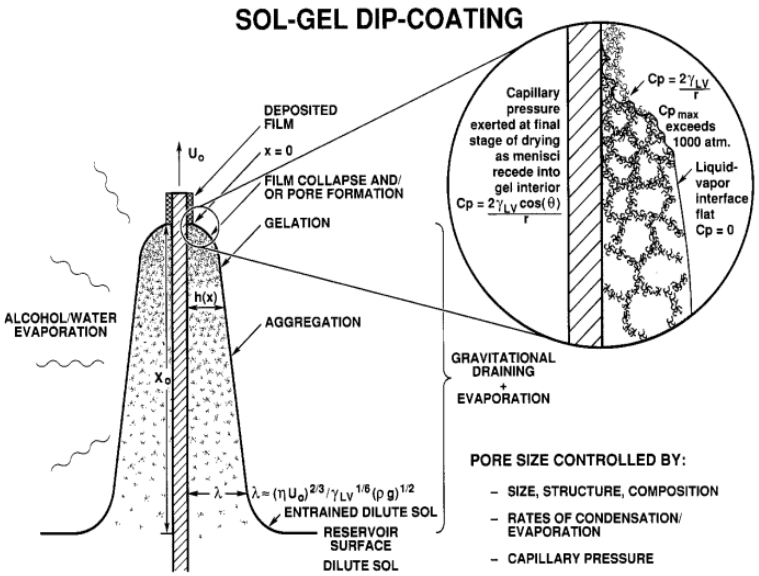

Fig. 2: Schematic of sol-gel dip-coating method [9]

Next, the sample undergoes a process of hydrolysis and polycondensation, that results in the formation of a colloidal suspension in the substance – the so called “sol”. This is later distributed in the substrate, and one method to do so is represented in diagram: Dip-Coating. This is later heat treated, and a matrix will be formed and converted into a solid substance.

The sol-gel process takes places at temperatures that are generally lower than other deposition methods, thus minimizing the thermal stress that the sample is exposed to. On another side, the preparation of the precursors in the sol gel method is very rigorous and time consuming, which could become very resource intensive for a larger scaling of this operation [2].

A hybrid layer of hydroxyapatite and TiO_2, deposited through the sol-gel method presents improvements in the mechanical resistance of the thin film with the substrate and of the cellular fixation density, compared to a single substance layer. Furthermore, it was found to be bioactive through the apparition of needle-like hydroxyapatite when submerged in a solution that stimulates biological fluid [4].

Advanced Sol-gel HAP coatings on titanium

Moreover, other research groups focused on optimizing the sol-gel process through the introduction on TiO_2 interlayers, to increase the coating adhesion and integrity.

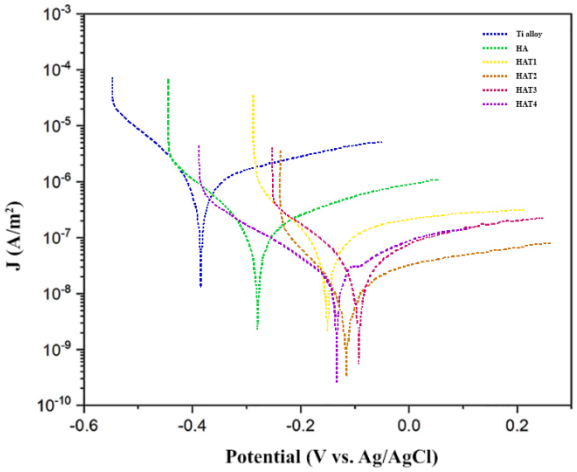

Fig. 3: Polarization Curve obtained through potentiodynamic testing [6]

The researchers were able to produce monophasic, crystalline hydroxyapatite films through pretreating Ti_6Al_4V samples with thermal oxidation, sol-gel coating

and anodization. Some of the observed advantages of this deposition method are high protective properties in simulated body fluid, demonstrated low corrosion rates, improved adhesive strength and they are free from cracks [6].

Critical parameters for the sol-gel deposition process have been identified, such as the pH value, aging time and sintering temperature. Another benefit of including the TiO_2 interlayers is the fact that the issue of mismatching thermal expansion coefficients has been alleviated, reducing the formation of cracks. The enhanced corrosion resistance has been proven through potentiodynamic tests, which shows that such coated implants are more suitable for long term applications.

In Figure 3, we can observe how the polarization curve obtained through potentiodynamic testing has shifted towards higher values of the corrosion potential [6], which indicates a lower tendency for the material to corrode. The curve labelled *Ti alloy* shows the highest corrosion current for the lowest corrosion potential, indicating low corrosion resistance. The red curve shows that for a hydorxyapatite coated sample, the corrosion potential increases and the current decreases, both of them being a desirable trait for better corrosion resistance. The HAT samples represent different thickness of titanium and hydroxiapatie bilayer coatings. Here we can see that the introduction of bilayer coatings acts as a barrier against corrosion, further reducing the parameters.

Electrophoretic deposition of hydroxyapatite coatings

The electrophoretic deposition of hydroxyapatite is another promising method of obtaining appropriate thin coatings on titanium bone implants [10]. Tests have been run by researchers to determine the optimum deposition voltage for a likeable outcome of a stable and uniform hydroxyapatite layer. The tests have been conducted at 20, 30 and 40 V dor 30 minutes in HAP suspension. Out of the three different depositions, the one at 30V gave the best results, after being evaluated for their thickness, morphology and electrochemical properties [11]. They have also exhibited the best corrosion resistance, showed fewer defects, higher compaction and remained intact for the longest period when being in contact with simulated body fluid.

The samples were studied using various analytical techniques, such as Field Emission Scanning Electron Microscopy (FE-SEM), Energy Dispersive Spectroscopy (EDS), X-ray Diffraction (XRD), and Fourier Transform Infrared Spectroscopy (FTIR).

In the FE-SEM image below, one can observe that the 20V sample displayed a more porous structure, whereas the other structures are more compact. At large voltages, such as 40V, large crystals that cause cracks in the thin film appeared as well [11].

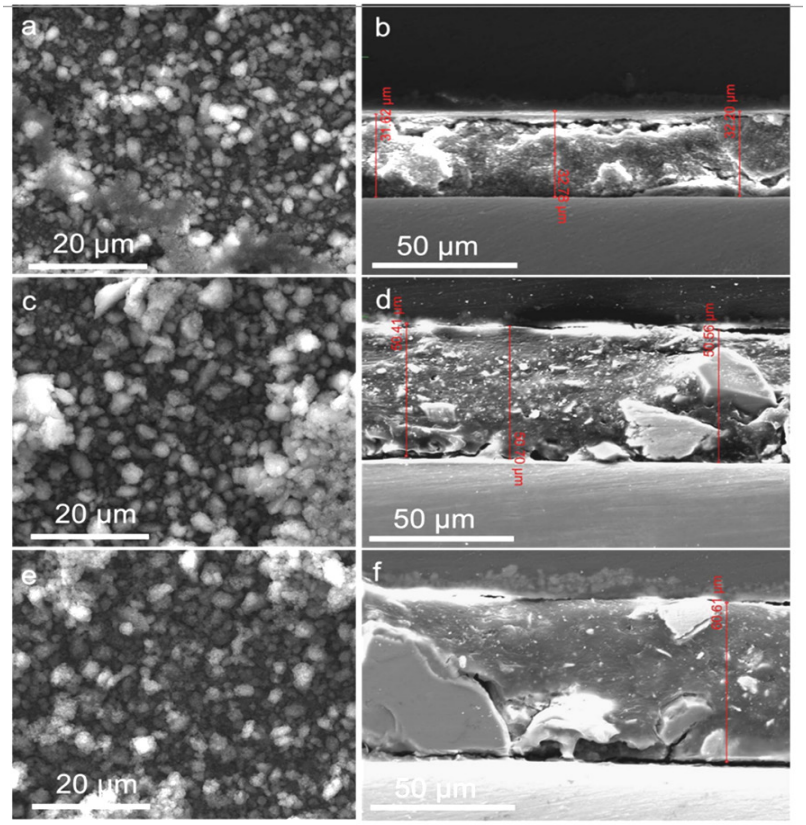

Fig. 4: FE-SEM Images in plane view and cross-sectional area of the HA coatings, deposited at 20V (a),(b), 30V (c),(d) and 40V (e),(f) [12]

Electrochemical method for hydroxyapatite deposition

This deposition method presents significant advantages in the deposition of HA on titania substrates. It offers a great control over the substrate thickness and ensures a uniform coverage, even if the substrate has a complex shape from a geometric perspective. This method allows for the doping with different ions in order to improve the biological characteristics of the sample [5]. Furthermore, this process leads to the formation of thin films with a really good adherence to the titania substrate, which is really important for the durability of titanium implants [13].

On another hand, due to the fact that this process is a line-of-sight one, it can result in a non-uniform coverage of substrates that have a complex geometry or deep grooves. The success of this deposition method relies heavily on the precise

control of the compounds that make up the electrolyte, and any deviation from it can cause a non-stoichiometric deposition of HA or the presence of unwanted phases of the compound [13].

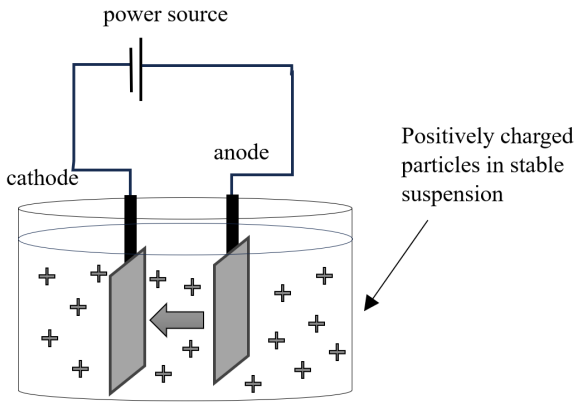

Fig. 5: Schematic of Electrochemical deposition method

Scanning electron Microscopy and Energy Dispersive X-Ray Analysis

Scanning Electron Microscopy (SEM) is a powerful analysis tool that is used for the study of the surface morphology of the thin films and their composition.

It works with the help of a thin, focused beam of electrons that will scan over the surface of the sample. As the electrons interact with the thin layer, they will be either backscattered or absorbed. If they are absorbed, they will cause the emission of secondary electrons, all of whom are later collected [14]. The secondary electrons are useful in the study of the topography of the sample, whilst the back-scattered electrons offer insights into the composition of the sample, their energy being correlated to the atomic number of the elements the material is made out of [15]. The analysis of the constituting elements takes the name of Energy Dispersive X-Ray analysis (EDX).

As seen in the SEM images below, this technique can give clear pictures of the morphology of the surface of the samples, its' uniformity, the film thickness and the orientation of HA crystals.

X-Ray Diffraction (XRD)

By measuring the intensity of diffracted X-Rays by a substance with a crystalline structure one can identify the phases of the material, its' crystallinity and other structural attributes, such as the presence of crystalline planes in the studied

substance [16]. Using the information about the atomical composition of HA obtained through the analysis of the EDX spectrum of secondary electrons, and the information about the crystal planes present in the sample obtained through XRD one can find a clear overall picture of the composition of the deposited film, both from the point of view of the elements that it consists of and the one of the crystalline phases that are present [17].

Fourier Transform Infrared Spectroscopy (FTIR)

Is an analytical technique used to obtain a infrared-absorption spectrum of a solid, liquid or gas. It is useful especially in the identification of organic and polymeric substances, and it can sometimes be used for inorganic substances as well. The technique relies on the phenomena of absorption of IR radiation with frequencies specifical to the modes of vibration of molecules, creating a spectral fingerprint for each material [2].

The FTIR technique plays an important role in the analysis of thin HA layers, offering insights into their structure and chemical composition. It can identify the presence of specific structural groups, such as phosphate PO_4 that have absorption bands at frequencies of 560 cm^{-1}, 600 cm^{-1} and 1000-1100 cm^{-1}. Hydroxyl OH groups can be highlighted by a absorption peak at the frequency of 3570 cm^{-1} [18]. By analyzing the position of such peaks, one can confirm the presence of key constituents of HA.

CONCLUSIONS

In conclusion, through this synthesis article we have achieved a comprehensive exploration of the deposition techniques such as the Sol-Gel method, electrochemical deposition and ultrasound spray pyrolysis, highlighting their applicability in the context of deposition of thin HA layers, mentioning their advantages and limitations.

The complementary analysis techniques such as X-Ray diffraction, Fourier Transform Infrared Spectroscopy and Scanning Electron Microscopy play important role in the characterization of HA thin films. FTIR offers information on the chemical groups present in the sample, XRD about the crystalline planes and HA phases, all while SEM gives insights on the morphology and stoichiometry of the sample.

BIBLIOGRAPHY

[1] B. Murphy, J. Baez, and M. A. Morris, “Characterizing Hydroxyapatite Deposited from Solution onto Novel Substrates in Terms of Growth Mechanism and Physical Chemical Properties,” MDPI AG, Jun. 2023, p. 34. doi: 10.3390/iocn2023-14491.

[2] P. Oladijo, H. Soon Min, and O. Oladijo, “Deposition and characterization of thin Films on Titanium Substrate: Review,” *International Journal on Emerging Technologies*, vol. 11, no. 4, pp. 299–305, 2020, [Online]. Available: https://www.researchgate.net/publication/347623166

[3] V. Jokanovic and D. Uskokovic, "Calcium hydroxyapatite thin films on titanium substrates prepared by ultrasonic spray pyrolysis," *Mater Trans*, vol. 46, no. 2, pp. 228–235, 2005, doi: 10.2320/matertrans.46.228.

[4] J. Harle, H. W. Kim, N. Mordan, J. C. Knowles, and V. Salih, "Initial responses of human osteoblasts to sol-gel modified titanium with hydroxyapatite and titania composition," *Acta Biomater*, vol. 2, no. 5, pp. 547–556, 2006, doi: 10.1016/j.actbio.2006.05.005.

[5] A. R. Boccaccini, S. Keim, R. Ma, Y. Li, and I. Zhitomirsky, "Electrophoretic deposition of biomaterials," Oct. 06, 2010, *Royal Society*. doi: 10.1098/rsif.2010.0156.focus.

[6] A. Jaafar *et al.*, "Sol–gel derived hydroxyapatite coating on titanium implants: Optimization of sol–gel process and engineering the interface," *J Mater Res*, vol. 37, no. 16, pp. 2558–2570, Aug. 2022, doi: 10.1557/s43578-022-00550-0.

[7] V. Nelea, C. Morosanu, M. Iliescu, and I. N. Mihailescu, "Hydroxyapatite thin films grown by pulsed laser deposition and radio-frequency magnetron sputtering: Comparative study," *Appl Surf Sci*, vol. 228, no. 1–4, pp. 346–356, 2004, doi: 10.1016/j.apsusc.2004.01.029.

[8] M. Honda, K. Kikushima, Y. Kawanobe, T. Konishi, M. Mizumoto, and M. Aizawa, "Enhanced early osteogenic differentiation by silicon-substituted hydroxyapatite ceramics fabricated via ultrasonic spray pyrolysis route," *J Mater Sci Mater Med*, vol. 23, no. 12, pp. 2923–2932, Dec. 2012, doi: 10.1007/s10856-012-4744-x.

[9] C. J. Brinker, P. R. Schunk, G. C. Frye, and C. S. Ashley, "NON-CRYSTALLINE SOLIDS Review of sol-gel thin film formation," 1992.

[10] M. C. Perju *et al.*, "Some Aspects Concerning Titanium Coverage with Hydroxyapatite," *Archives of Metallurgy and Materials*, vol. 67, no. 2, pp. 521–527, 2022, doi: 10.24425/amm.2022.137785.

[11] D. Annur, F. Bayu, S. Supriadi, and B. Suharno, "Electrophoretic Deposition of Hydroxyapatite/ Chitosan Coating on Porous Titanium for Orthopedic Application," *Evergreen*, vol. 9, no. 1, pp. 109–114, 2022, doi: 10.5109/4774222.

[12] S. Rahmadani, A. Anawati, M. D. Gumelar, R. Hanafi, and I. N. Jujur, "Optimizing parameter for electrophoretic deposition of hydroxyapatite coating with superior corrosion resistance on pure titanium," *Mater Res Express*, vol. 9, no. 11, Nov. 2022, doi: 10.1088/2053-1591/aca509.

[13] M. Manso, C. Jimeh Nez, C. Morant, P. Herrero, and J. M. Martmh Nez-Duart, "Electrodeposition of hydroxyapatite coatings in basic conditions," 2000.

[14] A. Ul-Hamid, *A Beginners' Guide to Scanning Electron Microscopy*. 2018. doi: 10.1007/978-3-319-98482-7.

[15] E. R. Fischer, B. T. Hansen, V. Nair, F. H. Hoyt, and D. W. Dorward, "Scanning electron microscopy," *Curr Protoc Microbiol*, no. SUPPL.25, May 2012, doi: 10.1002/9780471729259.mc02b02s25.

[16] B. D. Cullity, *Elements of X-ray Diffraction*, vol. 29, no. 12. 1978. doi: 10.1088/0031-9112/29/12/034.

[17] "X-Ray Diffraction Characterization of cristalinity and phase composition in plasma sprayed hap coatings".

[18] J. Reyes-Gasga, E. L. Martínez-Piñeiro, G. Rodríguez-Álvarez, G. E. Tiznado-Orozco, R. García-García, and E. F. Brès, "XRD and FTIR crystallinity indices in sound human tooth enamel and synthetic hydroxyapatite," *Materials Science and Engineering C*, vol. 33, no. 8, pp. 4568–4574, Dec. 2013, doi: 10.1016/j.msec.2013.07.014.

STUDIA UBB PHYSICA, Vol. 68 (LXVIII), 1-2, 2023, pp. 49-56
(RECOMMENDED CITATION)
doi:10.24193/subbphys.2023.05

FRIEDEL OSCILLATIONS IN A ONE-DIMENSIONAL NON-INTERACTING ELECTRON GAS IN THE PRESENCE OF TWO IMPURITIES

L. MÁTHÉ[1], I. GROSU[2*]

ABSTRACT. Using the linear response theory, we analyze Friedel oscillations in a one-dimensional non-interacting electron gas in the presence of two impurities with different potential strengths. The impurities potentials are modeled using Dirac delta function, as well as Lorentzian and Gaussian distribution functions. Our findings show that the density oscillations are strongly sensitive to both the distance between the impurities and their respective potential strengths.

Keywords: *One-dimensional electron gas, one impurity, two impurities, Friedel oscillations*

INTRODUCTION

Friedel oscillations describe the oscillatory behavior of electron density around impurities in a material, arising from the quantum character of electrons and their interactions with the crystal lattice [1,2]. The electron density exhibits periodic oscillations as a function of distance from the impurity, with the wavelength depending on the Fermi wavevector. The amplitude of the oscillations decreases with increasing distance from the impurity, and temperature can reduce the amplitude of the oscillations. The specific form of the oscillations is affected by the shape and the curvature of the Fermi surface. Impurities in the crystal scatter electrons leading to

[1] *National Institute for Research and Development of Isotopic and Molecular Technologies, 67-103 Donath str., 400293 Cluj-Napoca, Romania*
[2] *Babeş-Bolyai University, Faculty of Physics, 1 Kogălniceanu str., 400084 Cluj-Napoca, Romania*
* *Corresponding author: ioan.grosu@ubbcluj.ro*

perturbations of the electron density. The scattered electrons interfere giving rise to a standing wave pattern. Due to the Pauli exclusion principle, scattered electrons avoid regions where there are already other electrons, leading to formation of density oscillations. The distance dependence of charge oscillations is influenced by the dimensionality of the system. These oscillations can affect the electrical conductivity of materials, particularly in low dimensional systems, with graphene a special case [3]. The problem of Friedel oscillations in one-dimensional non-interacting electron gas in the presence of a single impurity was analyzed by Giuliani et al. [4], and later further extended to two impurities and a chain of dense impurities [5-7]. The Friedel oscillations have been theoretically studied in two-and three-dimensional electron Fermi liquids [8]. Additionally, Friedel oscillations in a nanowire symmetrically connected to two macroscopic electrodes with different chemical potentials have been investigated using the nonequilibrium Keldysh Green functions formalism [9]. The problem of Friedel oscillations in superconductors was also discussed within the framework of Bogoliubov-de Gennes theory [10]. More recently, Friedel oscillations in the presence of a non-Hermitian, imaginary impurity, have been studied using non-Hermitian linear response theory [11]. These theoretical results can be connected to experimental measurements, such as nuclear magnetic resonance [12], Mössbauer spectroscopy [13], scanning tunneling microscopy [14], and X-ray diffraction [15].

In this paper we analyze Friedel oscillations in a one-dimensional non-interacting electron gas, induced by two large impurities, modeled using Lorentzian and Gaussian distribution functions. The impurities have different potential strengths. The main goal of the present work is to study the effect of asymmetry in potential strengths on the Friedel oscillations. Additionally, we compare the numerically obtained results for the two models with the exact analytical results derived when the impurities are described by Dirac delta potentials.

MODEL

The two impurities are first modeled with a Dirac delta function [4,5,7] of different potential strengths (C_1 and C_2):

$$V_{ext}^{D}(x) = C_1\delta(x) + C_2\delta(x-a), \tag{1}$$

where x and a represent the distance from the perturbing impurity and the distance between impurities, respectively. We approximate the Dirac delta potential $V_{ext}^{D}(x)$ with a Lorentzian distribution function

$$V_{ext}^{L}(x) = \frac{C_1}{\pi}\frac{\varepsilon}{x^2+\varepsilon^2} + \frac{C_2}{\pi}\frac{\varepsilon}{(x-a)^2+\varepsilon^2}, \tag{2}$$

for small values of ε ($\varepsilon \to 0^+$), and a Gaussian distribution function

$$V_{ext}^{G}(x) = \frac{C_1}{\sigma\sqrt{2\pi}} e^{-\frac{x^2}{2\sigma^2}} + \frac{C_2}{\sigma\sqrt{2\pi}} e^{-\frac{(x-a)^2}{2\sigma^2}}, \tag{3}$$

when $\sigma \to 0^+$, respectively.

In the linear response theory, the dependence of the electron density deviation on the distance is expressed as follows [4-8]:

$$n(x) = \int_0^\infty \frac{dq}{\pi} \chi_0(q) V_{ext}(q) \cos(qx), \tag{4}$$

where $\chi_0(q)$ is the static Lindhard response function for one-dimensional non-interacting electron gas ($\hbar = 1$):

$$\chi_0(q) = \frac{2m}{\pi q} \ln\left|\frac{2k_F+q}{2k_F-q}\right|, \tag{5}$$

where m is the electron mass, and k_F stands for the Fermi wave number. The Fourier transform of the perturbing impurities potential $V_{ext}(q)$ is

$$V_{ext}^{D}(q) = C_1 + C_2 \cos(qa), \tag{6}$$

for the Dirac delta function. In the case of the Lorentzian and Gaussian distribution function based models, the Fourier transforms of the potentials are expressed as

$$V_{ext}^{L}(q) = [C_1 + C_2 \cos(qa)] e^{-\varepsilon|q|}, \tag{7}$$

and

$$V_{ext}^{G}(q) = [C_1 + C_2 \cos(qa)] e^{-\frac{\sigma^2 q^2}{2}}, \tag{8}$$

respectively. Using Eqs. (4)-(6) and applying the method outlined in Refs. [5-7], the electron density deviation can be analytically calculated as

$$n(x) = -\frac{2m}{\pi}\left\{C_1 si(2k_F x) + \frac{C_2}{2}[si[2k_F(x+a)] + si[2k_F(x-a)]]\right\}, \tag{9}$$

where $si(x)$ is the shifted sine-integral function, with $x > a$. In the case where $C_1 = C_2$, the expression for $n(x)$ from Eq. (9) reduces to that found in Ref. [5]. The distance dependence of the electron density within the Lorentzian distribution function model is expressed as

$$n(x)=\frac{2m}{\pi}\Big[\frac{C_1}{\pi}\int_0^\infty \frac{dy}{y}\ln\Big|\frac{1+y}{1-y}\Big|\cos(2k_Fxy)e^{-2\varepsilon k_F y} + \frac{C_2}{\pi}\int_0^\infty \frac{dy}{y}\ln\Big|\frac{1+y}{1-y}\Big|\cos(2k_Fxy)\cos(2k_Fay)e^{-2\varepsilon k_F y}\Big], \quad (10)$$

while for the Gaussian distribution function model, it reads

$$n(x)=\frac{2m}{\pi}\Big[\frac{C_1}{\pi}\int_0^\infty \frac{dy}{y}\ln\Big|\frac{1+y}{1-y}\Big|\cos(2k_Fxy)e^{-2\sigma^2 k_F^2 y^2} + \frac{C_2}{\pi}\int_0^\infty \frac{dy}{y}\ln\Big|\frac{1+y}{1-y}\Big|\cos(2k_Fxy)\cos(2k_Fay)e^{-2\sigma^2 k_F^2 y^2}\Big], \quad (11)$$

with a new variable $y = q/2k_F$. Eqs. (10) and (11) are numerically evaluated.

RESULTS AND DISCUSSION

In this section, we present our results for one-dimensional non-interacting electron gas in the presence of two impurities, modeled by Dirac delta potentials, as well as Lorentzian and Gaussian distribution functions. The Fermi wave number is used as the energy unit, i.e., $k_F = 1$.

We first model the asymmetry in potential strengths as $\gamma = C_2/C_1$ with potential strength of the impurity located at $x = 0$ fixed, i.e., $C_1 = C$. For simplicity, we introduce a normalized electron density $R(x) = n(x)/(2mC/\pi)$.

In Figures 1(a)-(c), we plot $R(x)$ as a function of the distance $k_F x$ for a single impurity within the three models discussed above, for different values of the scale parameters ε and σ, respectively. We observe that the analytical results obtained for the Dirac delta potential can be well approximated using either a Lorentzian or Gaussian distribution function when their scale parameters, ε and σ, are small. Additionally, it can be seen that when we use a Gaussian distribution function to approximate the impurity potential, our results will converge faster to the analytical result obtained for Dirac delta potential, as the half-width at half-maximum approaches zero. At the same time, the approximation of the impurity potential using a Lorentzian distribution function converges more slowly to the analytical result as the half-width at half-maximum decreases. This tendency can be clearly seen from the Fourier transforms of the potentials, given by Eqs. (6)-(8), respectively.

In Figures 1(d)-(f), the normalized density $R(x)$ is plotted as a function of the distance $k_F x$ for both one impurity and two impurities with different values of the potential strength parameter $\gamma = C_2/C_1$ (where $C_1 = C$) when the distance between impurities is $k_F a = 0$. We observe that the magnitude of the oscillations increases with the addition of a second impurity, while their phase remains unchanged at $k_F a = 0$, consistent with the findings in Ref. [5]. In addition, we find that the amplitude of the oscillations decreases or increases as the potential strength of the second impurity decreases or increases, respectively [see Figures 1(d)-(f)].

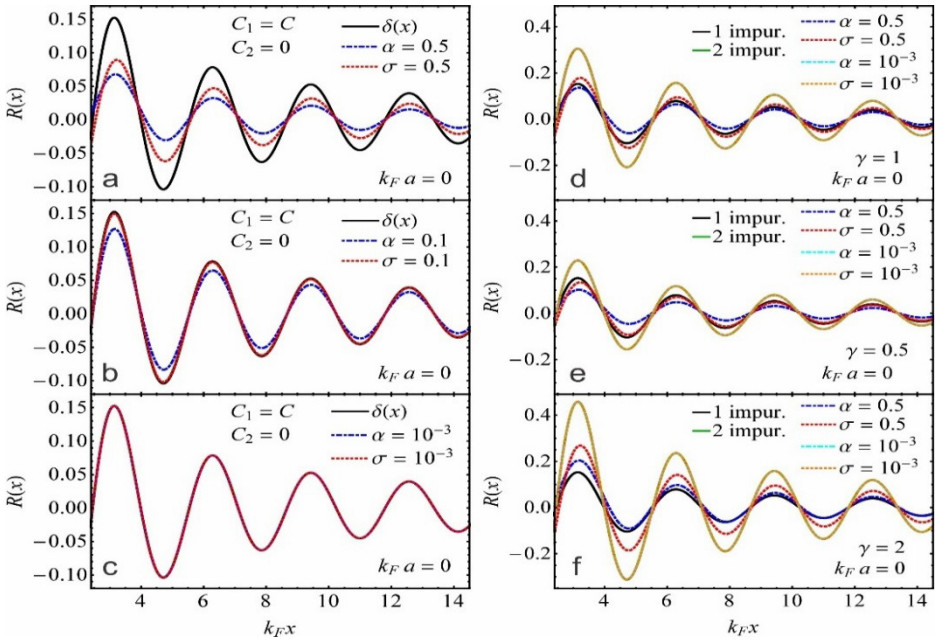

Fig. 1(**a**)-(**c**): $R(x) = n(x)/(2mC/\pi)$ as a function of $k_F x$ for a single impurity ($\gamma = 0$) at $k_F a = 0$ within different models. The black solid line corresponds to the analytical result obtained using the Dirac delta potential. The parameter values are indicated in the figures. (**d**)-(**f**): $R(x)$ as a function of $k_F x$ for one impurity (black solid line) and two impurities (green solid line), calculated analytically for $k_F a = 0$ with $k_F = 1$. The dotted lines represent the results based on the Lorentzian and Gaussian distribution function models, with different values of the scale parameters $k_F \varepsilon$ and $k_F \sigma$. The asymmetry in potential strengths is indicated in the figures.

Figures 2(a)-(f) show the results for $R(x)$ as a function of the distance $k_F x$ for one impurity and two impurities, when varying potential strength parameter $\gamma = C_2/C_1$ (where $C_1 = C$) with finite values of the distance between impurities, $k_F a \neq 0$. By changing the distance between the impurities and the potential asymmetry γ, a phase shift in the oscillations can be observed for smaller values of $k_F x$ [see Figures 2(a)-(c) for $k_F a = \pi/4$], due to the interference effects, as noted in Ref. [5]. A possible asymmetry in potential strengths has less impact on the magnitude of the oscillations at $k_F a = \pi/4$, in contrast to the $k_F a = 0$ case. A further increase in the distance $k_F a$ can lead to the formation of an antiphase between the oscillations caused by the two perturbing impurities and those caused by a single impurity [see Figures 2(d) and (f) for $k_F a = \pi/2$]. Note that the magnitude of the oscillations is significantly reduced in the presence of a second impurity with $\gamma = 1$ and $k_F a = \pi/2$. A deviation in potential strengths ($\gamma \neq 1$) can strongly influence the amplitude of the oscillations at $k_F a = \pi/2$.

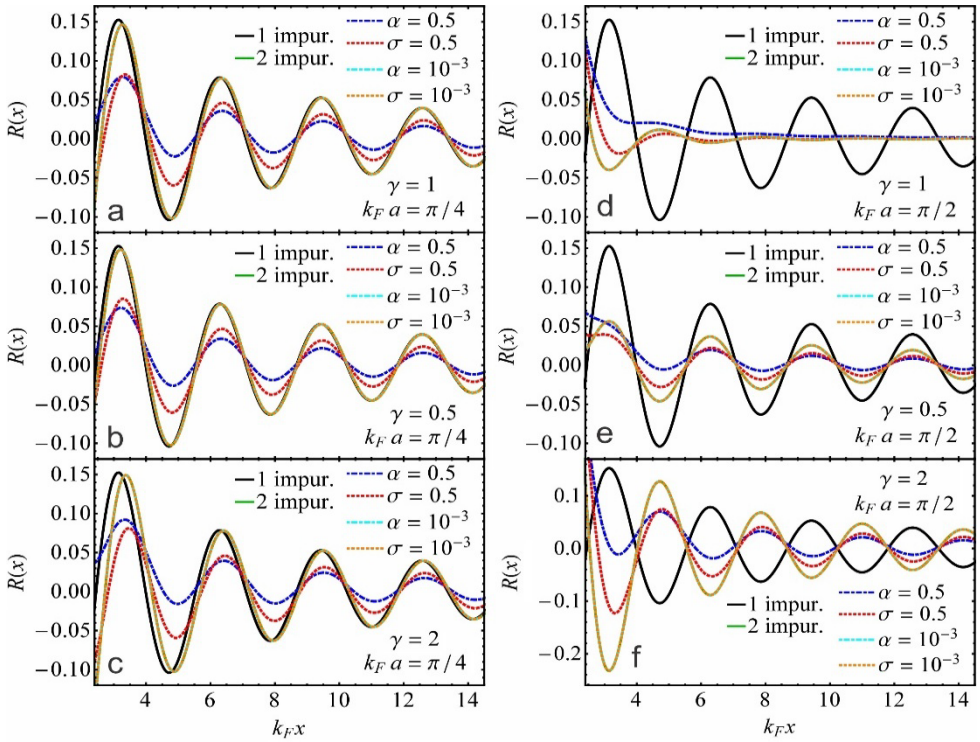

Fig. 2: The normalized density $R(x) = n(x)/(2mC/\pi)$ as a function of distance $k_F x$ for one impurity (black solid line, $\gamma = 0$) and two impurities (green solid line), calculated analytically. The dotted lines represent the results based on the Lorentzian and Gaussian distribution function models, with different values of the scale parameters $k_F\varepsilon$ and $k_F\sigma$. The distance between impurities $k_F a$ is: (**a**)-(**c**) $k_F a = \pi/4$ and (**d**)-(**f**) $k_F a = \pi/2$. The asymmetry in potential strengths γ is indicated in the figure.

Figures 3(a)-(c) present the results for $R(x)$ as a function of the distance $k_F x$ for one impurity and two impurities for different values of the distance between impurities $k_F a$ when the potential strengths (C_1 and C_2) are differently varied. We note that in the presence of two impurities, when the distance between them is $k_F a = 0$, Eq. (9) for the density variation $n(x)$ reduces to $n(x) = -(2m/\pi)(C_1 + C_2)si(2k_F x)$. Thus, this system with two impurities can be viewed as a single impurity located at $a = 0$, with a potential amplitude of $C_1 + C_2$. This can be seen by changing the values of C_1 while keeping C_2 fixed, or varying C_2 while keeping C_1 fixed in a similar manner, the oscillations show equal deviations from the results corresponding to the symmetrical $C_1 = C_2$ case [see Figure 3(a)]. Note that the large-distance ($x \gg a$) behavior of the electron density deviation $n(x)$ [4-7] is obtained as $n(x) \sim [m(C_1 + C_2)/\pi k_F] \cos(2k_F x)/x$.

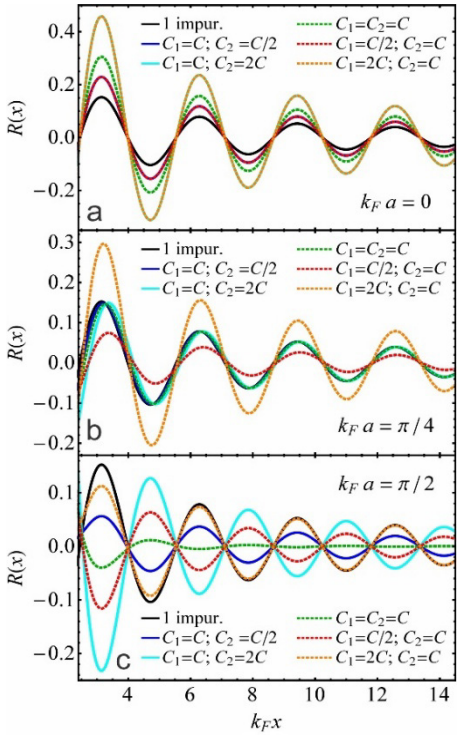

Fig. 3: The normalized density $R(x) = n(x)/(2mC/\pi)$ as a function of $k_F x$ for one impurity (black solid line, $C_1 = C$ and $C_2 = 0$) and two impurities, calculated analytically. The distance between the impurities is: (**a**) $k_F a = 0$, (**b**) $k_F a = \pi/4$ and (**c**) $k_F a = \pi/2$, with $k_F = 1$. The asymmetry in potential strengths is indicated in the figure.

In the case of $k_F a \neq 0$, the density oscillations become highly sensitive to any asymmetry appearing in potential strengths. Depending on the values of $k_F a$, the magnitude of the oscillations can be amplified by varying the potential strengths. In addition, for $k_F a \neq 0$, the large-distance behavior of the electron density deviation $n(x)$ is expressed as

$$n(x) \sim \frac{m}{\pi k_F}\left\{C_1 \frac{\cos(2k_F x)}{x} + C_2\left[\cos(2k_F a)\frac{\cos(2k_F x)}{x} + a\sin(2k_F a)\frac{\sin(2k_F x)}{x^2}\right]\right\}, \quad (12)$$

which reduces to the results in Ref. [5] when $C_1 = C_2$. Note that, in the symmetrical case ($C_1 = C_2$), at large distances and for values of $2k_F a = (2n+1)\pi$ (where n is a positive integer), the density oscillations vanish [5]. In the case of asymmetrical potential strengths, for $2k_F a = (2n+1)\pi$, the large-distance behavior of the density $n(x)$, as given by Eq. (12), reduces to the form $n(x) \sim [m(C_1 - C_2)/\pi k_F]\cos(2k_F x)/x$, which remains finite as long as $C_1 \neq C_2$.

CONCLUSIONS

In this work, we have investigated Friedel oscillations in a one-dimensional non-interacting electron gas induced by a single impurity and by two impurities with different potential strengths. The impurities have been modeled using a Dirac delta potential, as well as Lorentzian and Gaussian distribution functions. We have shown that the analytical results obtained with the Dirac delta potential can be well approximated using either a Lorentzian or Gaussian distribution function model. We have found that by further adding an impurity to a single-impurity system, the magnitude of the density oscillations can be significantly increased by appropriately adjusting the value of the distance between impurities. We have established that any asymmetry in the potential strengths of the impurities can strongly influence both the magnitude and phase of oscillations, depending on the values of the distance between the impurities.

ACKNOWLEDGMENTS

The authors would like to thank D. Sticleț, L. P. Zârbo and I. Botiz for valuable discussions. L. M. acknowledges financial support from the MCID through the "Nucleu" Program within the National Plan for Research, Development and Innovation 2022–2027, project PN 23 24 01 04.

REFERENCES

[1] J. Friedel, *Lond. Edinburgh Dublin Philos. Mag. J. Sci.* **43** (1952) 153
[2] J. Villain, M. Lavagna, P. Bruno, *C. R. Physique* **17** (2016) 276—290
[3] C. Bena, *C. R. Physique* **17** (2016) 302—321
[4] G. F. Giuliani, G. Vignale, T. Datta, *Phys. Rev. B* **72** (2005) 033411
[5] I. Grosu, L. Tugulan, *J. Supercond. Nov. Magn.* **21** (2008) 65—68
[6] I. Grosu, L. Tugulan, *Stud. Univ. Babes-Bolyai, Physica*, **LII**, **2** (2007) 79—84
[7] L. Tugulan, *Stud. Univ. Babes-Bolyai, Physica*, **LIII**, **1** (2008) 33—41
[8] G. E. Simion, G. F. Giuliani, *Phys. Rev. B* **72** (2005) 045127
[9] A. Gorczyca, M. M. Maśka, M. Mierzejewski, *Phys. Rev. B* **76** (2007) 165419
[10] M. Stosiek, C. Baretzky, T. Balashov, F. Evers, W. Wulfhekel, *Phys. Rev. B* **105** (2022) L140504
[11] B. Dóra, D. Sticlet, C. P. Moca, *Phys. Rev. B* **104** (2021) 125113
[12] C. Berthier, *J. Phys. C: Solid State Phys.* **11** (1978) 797—814
[13] T. Mitsui, S. Sakai, S. Li, T. Ueno, T. Watanuki, Y. Kobayashi, R. Masuda, M. Seto, H. Akai, *Phys. Rev. Lett.* **125** (2020) 236806
[14] P. Hofmann, B. G. Briner, M. Doering, H.-P. Rust, E. W. Plummer, A. M. Bradshaw, *Phys. Rev. Lett.* **79** (1997) 265—268
[15] S. Rouzière, S. Ravy, J.-P. Pouget, S. Brazovskii, *Phys. Rev. B* **62** (2000) R16231(R)

STUDIA UBB PHYSICA, Vol. 68 (LXVIII), 1-2, 2023, pp. 57-66
(RECOMMENDED CITATION)
doi:10.24193/subbphys.2023.06

EXPLORING THE FEASIBILITY OF PARALLEL I^{2}C SENSOR INTERFACING ON AN EDUCATIONAL FPGA BOARD: RESOURCE UTILIZATION ANALYSIS AND DESIGN CONSIDERATIONS

A. OPREA[1,2], B.S. KIREI[1,2], R.V.F. TURCU[1,3,*]

ABSTRACT. The goal of this work is to showcase the capabilities of Field Programmable Gate Arrays (FPGAs) as powerful reconfigurable computing devices for educational and research purposes. The work will demonstrate the high processing power of an FPGA by controlling multiple I^{2}C buses to and from peripheral sensors. The article will provide a guide on implementing a state machine in VHDL hardware description language and will present the response of the sensors and the working capacity of Basys 3 FPGA. The I^{2}C signals will be visualized using a Logic Analyzer and explained. The conclusion of the article will highlight the capabilities of FPGAs and explore the potential for their use in other complex tasks.

Keywords: *FPGA, sensor, I2C, fast processing, resource usage*

INTRODUCTION

Field-Programmable Gate Arrays (FPGAs) are widely utilized in physics research for their high-performance computing and processing capabilities [1], data acquisition and control systems [2]. In addition, this device can be reprogrammed in the field, which is a crucial feature for experiments where changes to the system

[1] *National Institute for Research and Development of Isotopic and Molecular Technologies, Centre of Advanced Research and Technologies for Alternative Energies (CETATEA), Cluj-Napoca, Romania*
[2] *Faculty of Electronics, Telecommunications and Information Technology, Technical University, Cluj-Napoca, Romania*
[3] *Faculty of Physics, Babeş-Bolyai University, Cluj-Napoca, Romania*
* *Corresponding author: flaviu.turcu@ubbcluj.ro*

are often necessary. In research, FPGAs have been used to implement high-speed digital signal processing systems for particle detectors [3], to control and synchronize multiple data acquisition systems [4], and to implement real-time data processing algorithms [5]. Moreover, FPGAs can directly interface with digital and analog components, such as sensors, facilitating rapid integration of new hardware into experimental setups. Table 1 presents a comparison of key resources between the Basys 3 FPGA and the Arduino Uno [6], [7], providing an overview of their capabilities for research purposes.

Table 1. Comparison between Basys 3 and Arduino Uno key resources

Function	Basys 3	Arduino
Work frequency	100 MHz	16 MHz
Volatile Memory	4.9 Mb block RAM	2Kb SRAM
Non-volatile Memory	180 Kb distributed	32 Kb flash memory
I2C maximum clock speed	700kHz	400kHz
Built-in DSP	Yes	No

This work analyzes the I2C protocol for real-time data transmission between a development board and two sensors using the Basys 3 FPGA [6] (Figure 1) The goal is to explore the potential of developing multiple sensor devices for complex applications, such as human-computer interfaces. The Basys 3 FPGA offers a wide range of peripherals and connectivity options, making it a versatile tool for various applications.

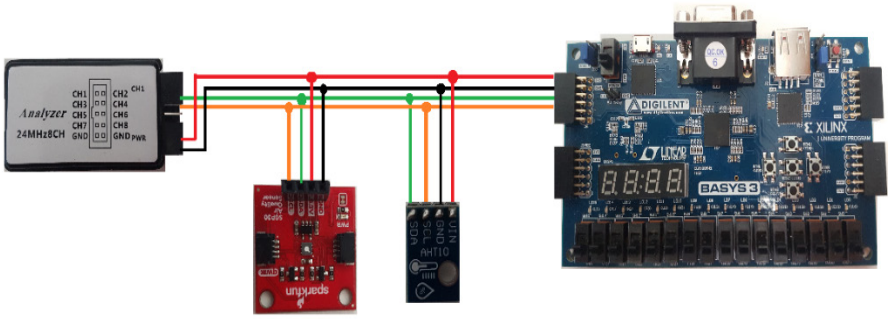

Fig. 1: External circuit designed for serial controlling of two sensors. From left to right: Logic Analyzer, SGP30 Air Quality sensor, AHT10 temperature and humidity sensor, Basys 3 board.

The AHT10 sensor [8] is a high-precision temperature and humidity sensor that uses Inter-Integrated Circuit (I^2C) protocol [9] for serial communication. It has a wide measurement range, high accuracy, and low power consumption. I^2C communication involves data, SDA, and a clock, SCLK, signal transferred bit by bit along a single wire. The frame format used by the protocol consists of a start bit , the I2C address, and write or read bits for commands or data transfer, respectively. The sensor responds with ACK bits and sends requested data bytes, with the session ending with a stop bit from the master device.

The SGP30 [10] (Figure 1) is a digital gas sensor used for measuring indoor air quality (IAQ) with high accuracy. It can detect a wide range of volatile organic compounds (VOCs) and gases, including carbon dioxide (CO_2). The sensor communicates via I^2C interface. It provides real-time output of IAQ measurements.

The FPGA configuration files are generated by the vendors proprietary software, in present case is the VIVADO design suite [11]. The hardware description language used for designing the digital circuits was VHDL. VHDL is a high-level hardware description language used to model digital circuits and systems. It is used to design complex digital systems by breaking them down into smaller, more manageable parts. In VHDL, designers use constructs like processes, signals, and components to describe the behavior of a digital system [12]. Concurrent processes in digital circuits execute in parallel and communicate using signals. Signals represent inputs/outputs and transmit data between processes. Components represent reusable hardware blocks that can be instantiated multiple times. VHDL is commonly used to implement controller modules for I^2C communication. These modules are designed as state machines that manage different protocol phases, such as start/stop condition, address phase, and data phase. State transitions are based on signal timing. The controller also includes logic for generating SCL clock signal based on desired frequency.

EXPERIMENTAL DETAILS

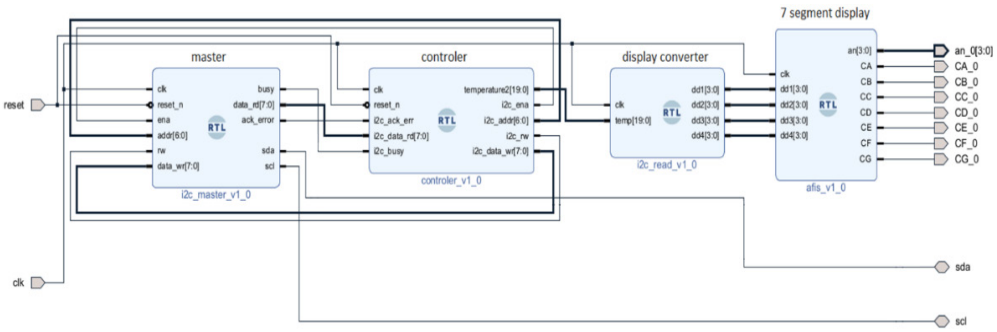

Fig. 2: Internal circuit made with VHDL for serial controlling of two sensors. From left to right, the following components are presented: master, controller, display converter and 7-segment display.

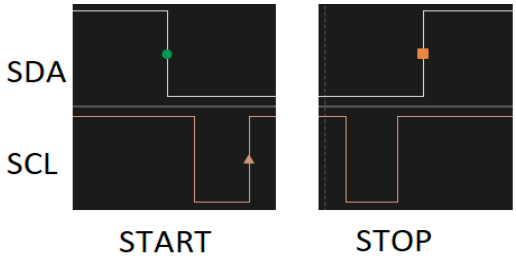

Fig. 3: Example of start and stop command. Falling edge of sda when scl is high, sets start command and rising edge of sda when scl is high sets stop command.

Figure 2 contains the main internal modules designed for controlling the sensor. The master is responsible for direct data transfer between board and sensors over SDA and SCL lines. Controller manages different states of the process and display modules help visualizing processed data. Start and stop conditions are depicted in Figure 3 below:

The two sensors' protocols are similar and depicted in Figure 4 using an algorithm for a finite state machine managed by the controller that guides the master through communication with sensor. The system starts in an idle state, then triggers the master to send slave address and command. After a pause for sensor data acquisition, the controller enters read command state, sends sensor address and read bit '1'. In read data state, the controller waits for master to send data and sends acknowledgement after each byte. Transaction ends with NACK bit

and stop. The external circuit for controlling AHT10 and SGP30 is shown in Figure 1. Signals captured with a Salea Logic Analyzer are displayed in Figure 5 [14]. It's important to note that AHT10 and SGP30 have different data acquisition times after triggering, with SGP30 requiring a longer waiting time of 12 ms compared to AHT10, which requires a significantly shorter time of less than 1 ms [8], [10].

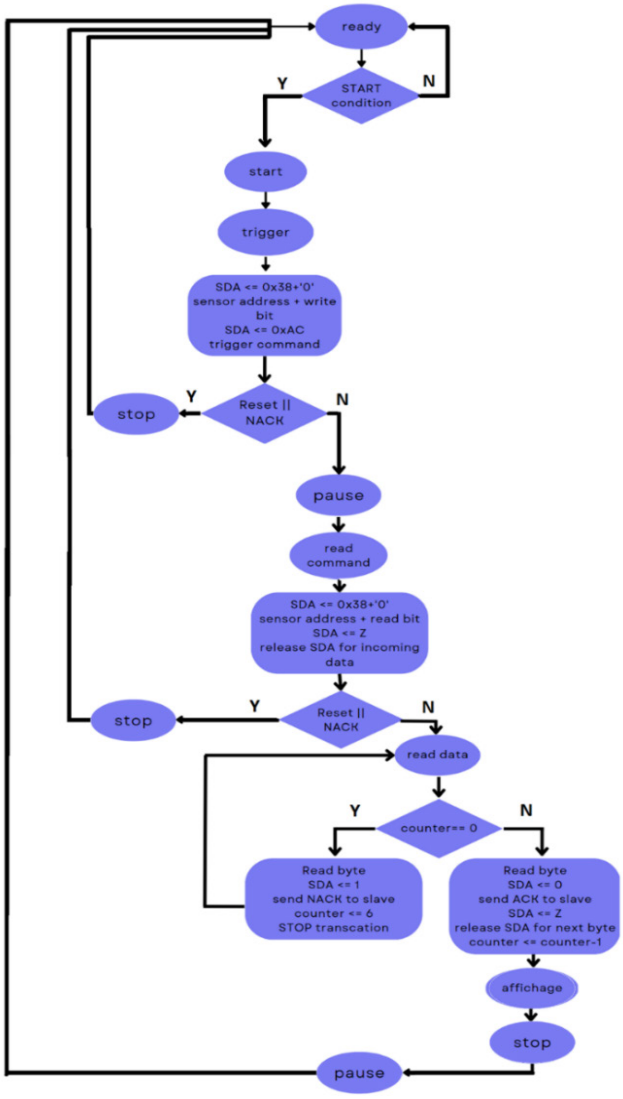

Fig. 4: Finite state machine implemented for controller communication with master. It follows all steps between start and data read and affichage and accounts for any NACK or reset.

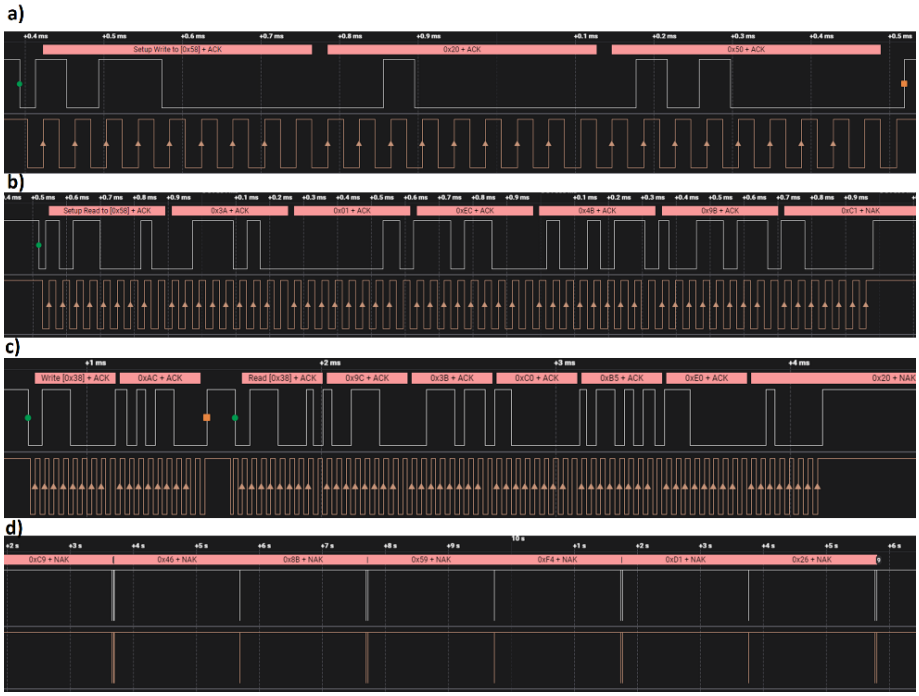

Fig. 5: SDA and SCL signals for serial communication**. a)**: Start transaction and data bytes sent from master to SGP30 sensor: 0x58 address + '0' write bit followed by '0' ACK bit sent from sensor; **b)**: command bytes: 0x20 and 0x50 followed by ACK from slave. Second: Data transfer from SGP30 sensor and stop command: 0x58 address + '1' read bit followed by '0' ACK bit sent from sensor; 5 data bytes sent from sensor to master followed by ACK sent from master, last data byte followed by stop command; **c)**: Full transaction between master and AHT10 sensor: Start command followed by address 0x38 and trigger command 0xAC. After 1ms pause the master sends address with read bit and starts receiving 6 bytes of data than it stops the transaction by sending NACK bit which means it sets sda to high impedance 'Z'; **d)**: Transaction buses over time for common sda and scl wires, the board alternates between the two sensors.

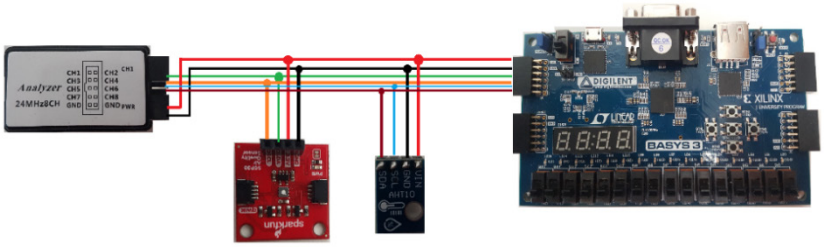

Fig. 6: External circuit designed for parallel controlling of the two sensors. From left to right: Logic Analyzer, SGP30 sensor, AHT10 sensor, Basys 3 board.

To resolve potential delays in processing multiple signals, the design was modified to utilize multiple PMOD ports and enable simultaneous data acquisition from both sensors using separate SDA and SCL wires for each sensor [15].

The updated design in Figure 6 incorporates additional pins on the Basys 3 board for the new SDA and SCL wires. Figure 7 shows the internal circuit of the parallel processing design with two masters, one for each sensor, allowing for customized working frequencies. Concurrent data transfer is illustrated in Figure 8, with data from each sensor transmitted via its respective SDA.

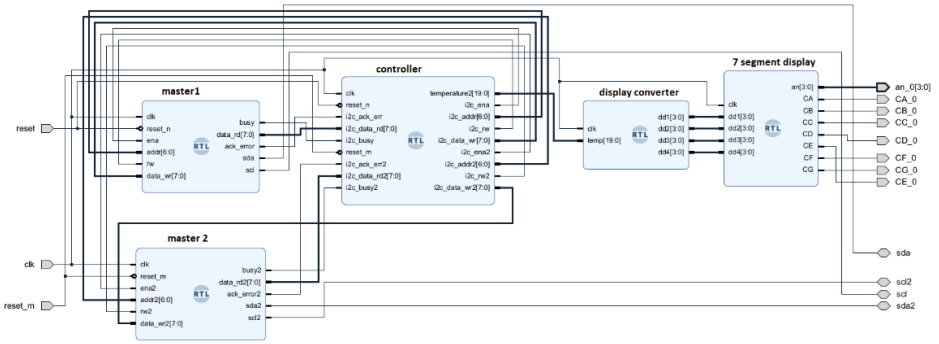

Fig. 7: Internal circuit made with VHDL for parallel controlling of two sensors. From left to right: two masters, controller, display modules.

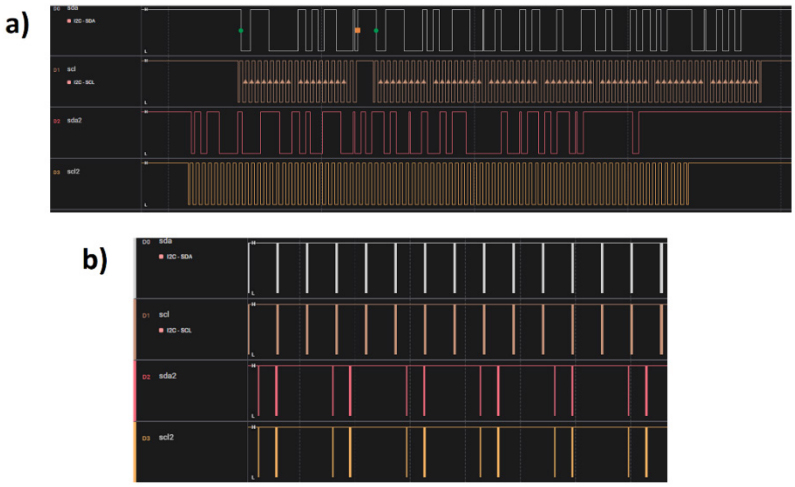

Fig. 8 a): Parallel transaction between board and the two sensors, up: AHT10 sensor, down: SGP30 sensor. Data from both sensors is transmitted at the same time. This method allows for different work frequencies; **b):** Transaction buses over time for parallel communication, the board uses multiple SDA and SCL wires and receives data from multiple sensors at the same time.

RESULTS AND DISCUSSION

Table 2 summarizes resource utilization in various scenarios, including multiple sensors and a simpler scenario with one sensor. Data was obtained from Vivado's report after bitstream generation, showing <0.5% increase in resource usage with new sensors or design development. Resource utilization is reported for three I^2C working frequencies (100 kHz, 400 kHz, and 700 kHz). Resource demand does not exhibit linear behavior with increasing I^2C working frequency. Metrics include Slice LUTs, Slice Registers, Slice, and Bonded IOB.

Table 2. VIVADO Summary of resource demand for driving one, two serial and two parallel sensors.

	Single sensor				Double sensor serial				Double sensor parallel			
Site Type	Frequency (kHz)	Used	Available	Utilized (%)	Frequency (kHz)	Used	Available	Utilized (%)	Frequency (kHz)	Used	Available	Utilized (%)
Slice LUTs	100	3364	20800	16.17	100	3415	20800	16.42	100	3507	20800	16.86
	400	3364		16.18	400	3414		16.41	400	3505		16.85
	700	3367		16.19	700	3415		16.42	700	3507		16.86
Slice Registers	100	166	41600	0.4	100	203	41600	0.49	100	246	41600	0.59
	400	164		0.39	400	201		0.48	400	242		0.58
	700	164		0.39	700	201		0.48	700	242		0.58
Slice	100	1004	8150	12.32	100	990	8150	12.15	100	1030	8150	12.64
	400	971		11.91	400	990		12.15	400	1055		12.94
	700	990		12.15	700	988		12.12	700	1035		12.7
Bonded IOB	-	17	106	16.04	-	17	106	16.04	-	18	106	16.98

The Slice LUTs are basic building blocks in an FPGA for implementing combinational logic functions; SliceRegisters (FFs) are Flip-flops used for storing data and implementing sequential logic; Slice are configurable portion of an FPGA for implementing digital circuits and Bonded IOB represent specialized blocks for interfacing with external signals.

The analysis indicates that the Basys 3 FPGA board can handle more complex tasks and has high performance potential for multi-sensor applications, as demonstrated by successful operation at 700 kHz I^2C frequency.

CONCLUSIONS

This study introduced an educational FPGA board as a powerful tool for sensor data recording and processing in experimental physics. The I^2C communication protocol and specifics of communication with the sensors were described. Data recording was successfully achieved at various SCL frequencies. The findings suggest potential for research, education, and industrial applications where high-speed sensor

communication and processing capabilities are needed. Further exploration could unlock the Basys 3 FPGA's full potential for complex tasks in embedded systems and digital design. More information about the VHDL code used can be found at [16].

Results highlight the versatility and suitability of the Basys 3 FPGA for advanced future applications requiring simultaneous control and communication with multiple sensors. A proposed such application is a human-machine interface in the shape of a pointer incorporating multiple positioning sensors and accelerometers for real time 3D painting in the air. This application could be a helpful tool in fields like education, arts, or presentations. The interface would allow users to create different shapes by moving the pointer in the air, capturing the position and acceleration data from the sensors and visualizing them on a display or with the help of VR glasses.

REFERENCES

[1] M. I. AlAli, K. M. Mhaidat, and I. A. Aljarrah, "Implementing image processing algorithms in FPGA hardware," in *2013 IEEE Jordan Conference on Applied Electrical Engineering and Computing Technologies (AEECT)*, Amman, Jordan: IEEE, Dec. 2013, pp. 1–5. doi: 10.1109/AEECT.2013.6716446.

[2] S. Bao, H. Yan, Q. Chi, Z. Pang, and Y. Sun, "FPGA-Based Reconfigurable Data Acquisition System for Industrial Sensors," *IEEE Trans. Ind. Inform.*, vol. 13, no. 4, pp. 1503–1512, Aug. 2017, doi: 10.1109/TII.2016.2641462.

[3] L. Musa, "FPGAS in high energy physics experiments at CERN," in *2008 International Conference on Field Programmable Logic and Applications*, Heidelberg, Germany: IEEE, 2008, pp. 2–2. doi: 10.1109/FPL.2008.4629896.

[4] K. T. Pozniak, "FPGA-based, specialized trigger and data acquisition systems for high-energy physics experiments," *Meas. Sci. Technol.*, vol. 21, no. 6, p. 062002, Jun. 2010, doi: 10.1088/0957-0233/21/6/062002.

[5] G. Korcyl *et al.*, "Evaluation of Single-Chip, Real-Time Tomographic Data Processing on FPGA SoC Devices," *IEEE Trans. Med. Imaging*, vol. 37, no. 11, pp. 2526–2535, Nov. 2018, doi: 10.1109/TMI.2018.2837741.

[6] Digilent, "Basys 3 Reference Manual." https://digilent.com/reference/programmable-logic/basys-3/reference-manual?redirect=1

[7] ATMega, "Arduino® UNO R3 Product Reference Manual." [Online]. Available: https://docs.arduino.cc/resources/datasheets/A000066-datasheet.pdf

[8] Asair, "AHT10 Technical Manual ASAIR® Temperature and humidity sensor," [Online]. Available: https://server4.eca.ir/eshop/AHT10/Aosong_AHT10_en_draft_0c.pdf

[9] Philips Semiconductors, *The I2c-bus specification*. 1998.

[10] SENSIRION, "Datasheet SGP30 Indoor Air Quality Sensor for TVOC and CO2eq Measurements."

[11] Xilinx, “Vivado Design Suite.” [Online]. Available:
https://caxapa.ru/thumbs/486666/wp416-Vivado-Design-Suite.pdf
[12] nandland, “VHDL Tutorials and Examples.” https://nandland.com/learn-vhdl/
[13] sparkfun, “I2C Introduction.” https://learn.sparkfun.com/tutorials/i2c/all
[14] saleae, “Saleae Logic Analyzer.” [Online]. Available: https://www.saleae.com/
[15] Digilent, “Basys 3 Artix-7 FPGA Trainer Board.” [Online]. Available:
https://digilent.com/reference/programmable-logic/basys-3/start
[16] “I2C sensor control with FPGA.” https://github.com/AlexOProject/FPGA-I2c-sensor-controll.

STUDIA UBB PHYSICA, Vol. 68 (LXVIII), 1-2, 2023, pp. 67-81
(RECOMMENDED CITATION)
doi:10.24193/subbphys.2023.07

COMPARATIVE STUDY ON THE SPEED OF SOUND MEASUREMENT IN METALS BASED ON COLLISION TIME

R. PÉTER[1], A.R. TUNYAGI[2*], A. SIMON[2*]

ABSTRACT. Several electrical measurement methods based on impact time measurements are presented in order to determine the sound propagation velocity in different metals. The sound impulses were initiated by dropping metal rods or tubes on a rigid anvil, and the speed of sound was determined by measuring the impact time and the time needed for the wave to propagate from the impacting end to the free end. Several electric methods are presented and compared, the results obtained for the speed of sound being in fair agreement with theory. The experiments described in this paper could be successfully used as undergraduate Physics experiments leading students towards better understanding of phenomena regarding sound propagation in solids.

Keywords: *sound propagation in solids, impact time, electric methods, comparison*

INTRODUCTION

The physics of mechanical wave propagation plays an important role in the education process of both physicists and engineers. It provides the first introductory steps to wave phenomena and will support, from both phenomenological and mathematical point of views, further more complex subjects such as optics, quantum mechanics or electromagnetism.

[1] *Undergraduate student, Engineering Physics,*
[2] *Faculty of Physics, Babeș-Bolyai University, Cluj-Napoca, Romania*
* *Corresponding authors: alpar.simon@ubbcluj.ro*; *arthur.tunyagi@ubbcluj.ro*

More and more accurate measurements of speed of sound in different propagation media have a very long, almost 400 years old history [1].

The development of measurement techniques from Kundt's tube to the use of sophisticated microphones made the measuring of speed of sound in air to become a relatively easy task. Meanwhile, the measurement of sound speed in solids, especially in metals, using electrical methods can be more difficult and complex, from both theoretical and experimental point of views, and it is an excellent inter- and multidisciplinary subject for undergraduate research for Engineering Physics students

This work describes and compare several electric methods based on impact time used to determine the speed of sound in metals. It was proposed as a graduation project for Engineering Physics specialization, at Babeș-Bolyai University, Faculty of Physics [2].

The paper is organized as follows: in the first section some general considerations are presented about sound propagation with a short review of measuring techniques for propagation in metals, a simple experimental set-up based on the impact time measurement between a metallic rod or tube and a compact anvil is described in the subsequent sections together with several appropriate measurement techniques. Finally, results are presented and conclusions are made.

SOUND VELOCITY AND ITS MEASUREMENT TECHNIQUES

The physical phenomenon of sound is defined to be a disturbance of matter that is transmitted as a wave from its source outward, through a transmission medium that surrounds the source, with a well-defined velocity called speed of sound.

According to standards, sound may be defined as being an "oscillation in pressure, stress, particle displacement, particle velocity, etc., propagated in a medium with internal forces (e.g., elastic or viscous), or the superposition of such propagated oscillation" [3, 4].

Sound can propagate through a medium (gas, liquid, solid or plasma) as longitudinal wave and as a transverse (shear) wave, but only in solids. At a fixed distance from its source, the pressure, velocity, and displacement of the medium will vary in time and at a given moment in time, the pressure, velocity, and displacement may vary in space.

The sound propagation is generally affected by the relationship between the density and pressure of the medium (affected also by temperature), the motion of the medium itself (being subject to Doppler-Fizeau effect) and the viscosity of the medium (causing attenuation).

Sound, like all waves, travels at a certain speed through the propagation medium and has the properties of frequency and wavelength. Direct evidence of the speed of sound can be observed while watching some phenomena implying both sound and light, thundering and lightning for instance. The flash of the lightning is seen well before the sound of the thunder is heard, implying that sound travels at a finite speed, much lower in value than light.

The speed of sound depends on the medium the sound waves pass through; it is a fundamental property of the material and is given by a Newton–Laplace type equation:

$$c_s = \sqrt{\frac{K}{\rho}} \tag{1}$$

where c_s is the speed of sound, ρ is the mass density of the medium and K describes the stiffness of the medium (modulus of bulk elasticity for gases and liquids and Young's modulus for solids, respectively).

In the case of plasmas, sound velocity is given by a much-complicated relationship, depending on electrons kinetic temperature and charge state and mass of ions from plasma.

Regarding speed of sound measurements, traditionally two fundamental directions are commonly used. Either the travelling time between two reference points is measured or the measurement of frequency (the inverse of propagation time) or wavelength is performed. The implemented measurement techniques are various.

The first ever reasonably accurate estimate of the speed of sound in air was performed by W. Derham: the time interval was measured between the sight of a fired gun smoke and hearing firing [1].

Probably the most well-known historical experiment for the measurement of the speed of sound in a gas or a solid rod was performed in 1866 by German physicist A. Kundt using the tube later named after him [5].

This type of experiment uses a metal rod held in midpoint and excited to vibrate along its length at one end, and a movable piston blocking the other end, capable to adjust the length of the tube. When the length of the tube is a multiple of half wavelength, the sound waves in the tube are in the form of standing waves, and the fine powder deposited previously inside tube is rearranged in a very specific pattern (nodes and antinodes). The distance between the neighboring nodes is one half wavelength of the sound. By measuring the distance between the nodes, the wavelength can be found, multiplying it by the frequency the speed of sound is found. Modern experimental demonstrations usually use a loudspeaker attached to a signal generator producing a sinusoidal wave.

The modern, weaponless version of Derham's experiment uses two microphones and a fast-recording device (digital storage scope). The sound source and the two microphones are arranged in a straight line, with the sound source at one end. The oscilloscope records the delay between the signals given by the two microphones, the distance between them divided by delay time will give the velocity of sound. A more sophisticated versions implies the use of PC sound cards and adequate software for recording and processing [6]. This technique is a single-shot timing type method or it may be regarded as a time-of-flight technique.

Another widely used measurement technique implies the use of a laboratory made "giant make-and-break switch": one part of the "switch" will be the metal rod or tube in which we want to determine the speed of sound, the other component is a hitting hammer, a colliding body or a large metallic base. When contact is made for a short period of time (cause by a hit or a single drop), the compression pulse travels along the rod or tube to the far end and is reflected as a rarefaction pulse to the near end. The sound path will be twice the length of the rod and the speed of sound will be equal to this distance over contact time. In the scientific literature there are several techniques used to measure this contact time:

a) by partially discharging a capacitor through a resistance or speaker during contact and then determining the residual charge [7-9]

b) by using a digital timer [10]

c) by sound sensor or the movement of a pendulum bob [11].

Other time-of flight techniques use gongs, bells, and hammers with oscilloscopes [12, 13] or PC audio cards [12] or 555 timer-based circuitry and piezoelectric sensor [14] or oscilloscope [15].

Speed of sound might be determined using Lissajous figures [16)] or smartphone and cardboard too [17].

EXPERIMENTAL DETERMINATIONS

A simple experimental set-up was built up to measure the impact time between a metallic rod or tube and a large compact metallic anvil (Fig. 1).

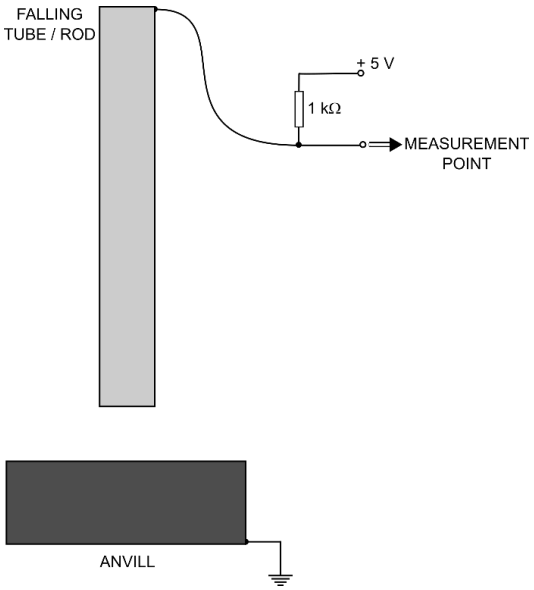

Fig. 1: The experimental set-up

As one can see, the set-up is a make-and-brake switch incorporated in a voltage divider, the voltage at the measurement point would be the supply voltage (+ 5 V) when there is no contact between the tube or rod and the anvil, and 0 V if the collision takes part.

The theoretical shape of the signal at the measurement point is presented in Fig.2.

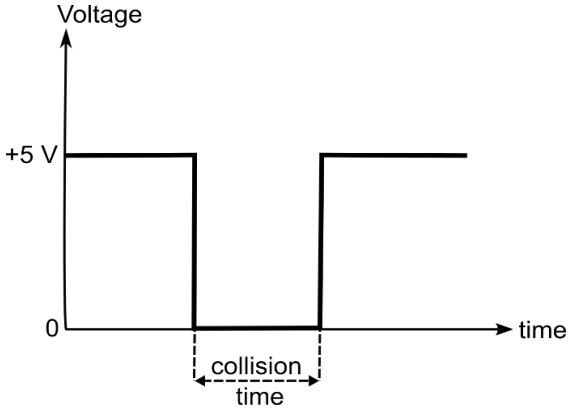

Fig. 2: Theoretical signal shape

The rod or the tube was freely dropped on the anvil and caught after the first spring up to avoid further contacts with the anvil. The time dependence of the voltage at the measurement point could be measured or recorded and the value of the collision time deduced.

The different tubes and rods used during experiments are presented in Table 1.

Table 1. Tubes and rods used in experiment

Material	Type	Diameter (cm)	Thickness (mm)	Length (cm)
Cu	tube	3	1	20.1
				32.2
				51.5
				84.0
				110.4
Al	tube	1.2	1.5	23.1
				33.7
				42.1
				51.4
				60.2
				72.1
	rod	2	-	25.4
				51.2
				75.0
				99.6

Five different measurement techniques were applied to analyze the voltage at the measurement point.

***Method 1*:** An Arduino Uno [18] microcontroller was used to analyze the signal by means of a build in function called *pulseIn* [19]. Particularly in our experiments, the so-called LOW pulse read method was applied using the digital pin 7 of the Arduino. The + 5 V supply voltage was ensured by the microcontroller.

It was observed that with this method the measurements were sensitive to dropping and surface shaping, the emerging noise having an unwanted influence on the shape of the signal. The *pulseIn*() method from Arduino framework is not able to handle multiple edges which are present in the real experiment, due to imperfect contact between the dropped rod and the sitting anvil.

***Method 2*:** The same Arduino Uno was used, this time the detection was made using Falling interrupt in conjunction with the Timer1 from the Atmega328. The Timer1 was configured to run in NORMAL mode with an input clock prescaler of 1. Considering the 16 MHz quartz crystal, from the Uno, the Timer1 is incremented every (1/16) μs. This counting is used to measure the time between the first falling edge and the last rising edge of a contact pulse as describer earlier. The routine is presented in the figure from below where the first part of the code is responsible with the detection of the first falling edge and the second part of the code is responsible to catch the last rising edge of the pulse and to store that value of the timer in the "ui16PulseEndTime" variable.

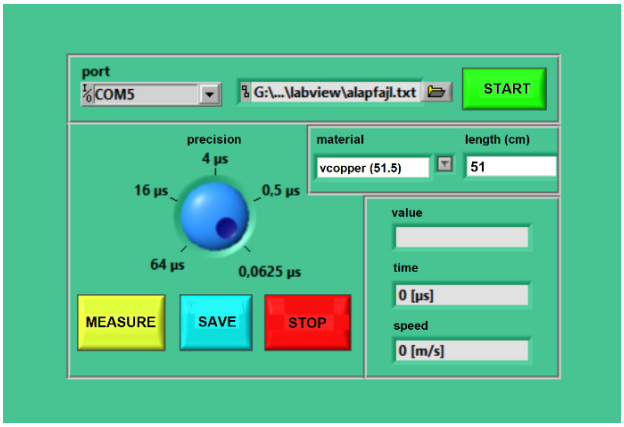

Fig. 3: The LabView interface

```
49  void LowEdgeInterrupt(void)
50  { // called if a falling edge is detected
51
52    // detecting the beginning of the pulse (the first falling edge)
53    if(!bStartEdgeDetected)
54    { // initial edge detected
55      TCNT1 = 0;  // clear the timer counting register
56      bStartEdgeDetected = true;
57    }
58
59    // detecting the last rising edge of the pulse (the end of the pulse)
60    while(!(PIND & (0x01 << 2)))
61    { // stay in this loop untill the PD2 is LOW => catch the last RISING transaction
62      ui16PulseEndTime = TCNT1;
63    }
64
65    return;
66  }
```

Fig. 4: Sequence of the Arduino code

The interrupt reaction time will decrease the total contact pulse width value but this was measured and a correction can be added. A jittering effect in time measurement is also added due to the time spent inside the while loop depending when exact the last falling edge occurs and when the while loop condition is checked. These errors can be corrected by adding a 3.7 μs to the total time measured by the timer and the real times are obtained.

To check the methods precision, we have used an AnalogDiscovery2 to generate standard pulses and checked the length of the pulses using the Arduino. The results are discussed below.

For a 10 μs pulse generated with the AnalogDiscovery the Arduino measured 102 timer pulses and that means:

$$\frac{102}{16} = 6.375 + 3.7 = 10.075\ \mu s$$

For a 100 μs pulse generated with the AnalogDiscovery the Arduino measured 1542 timer pulses and that means:

$$\frac{1542}{16} = 96.375 + 3.7 = 100.075\ \mu s$$

For a 200 μs pulse generated with the AnalogDiscovery the Arduino measured 3138 timer pulses and that means:

$$\frac{3138}{16} = 196.125 + 3.7 = 199.925\ \mu s$$

This demonstrate that using a simple Arduino Uno board it is possible to measure the speed of sound even as an elementary physics teaching activity on a high school.

***Method 3*:** Measurements are performed using a LCsoft Miniboard [20] and the *PulseView* software. The miniboard supplied the + 3.3 V for the divider, the HIGH and LOW signals were taken from digital pin 7 and the collision time was measured using cursors on the *PulseView* plot (Fig. 5).

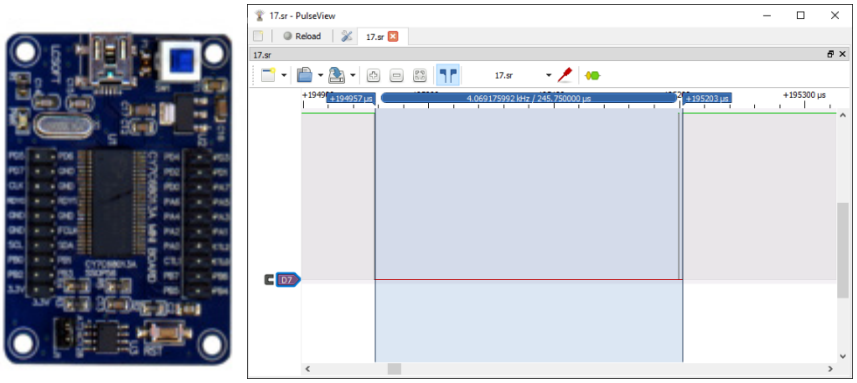

Fig. 5: The LCsoft Miniboard and PulseView window

***Method 4*:** At the measurement point the voltage was monitored by a *Tektronix DPO3032* oscilloscope [21, 22]. The oscilloscope was programmed to expect a negative impulse and to measure its length (Fig. 6).

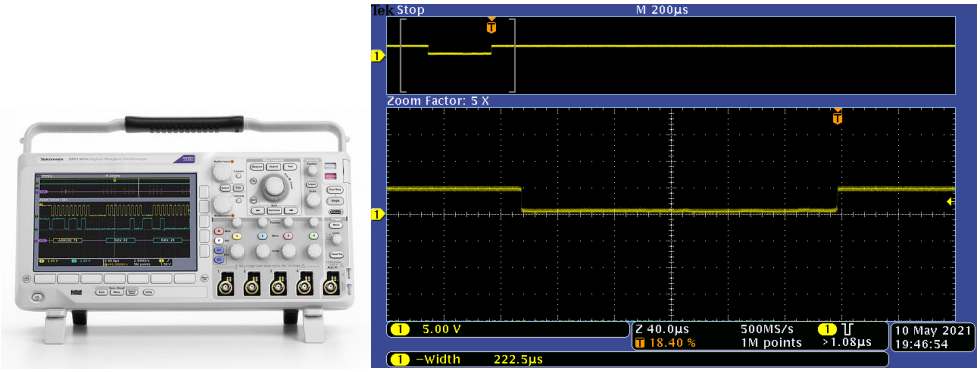

Fig. 6: The oscilloscope and the measuring window

All the above-mentioned methods will lead to the speed of sound in the metal (v) by means of the formula:

$$\mathrm{v} = \frac{2l}{t} \tag{2}$$

where l is the length or the tube of the rod, and t is the collision time.

***Method 5*:** The voltage divider was replaced by a piezoelectric sensor [23] attached to the free end of the rod or tube. The arrival of the shock wave to the sensor was detected by means of a voltage. This method does not measure the contact time between the two metallic parts, but the travelling time necessary for the sound to travel from the contact end to the free end (Fig. 7).

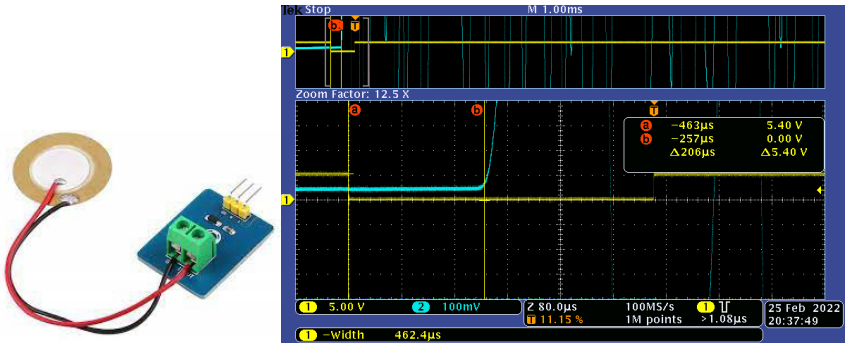

Fig. 7: The piezo sensor and the measuring window

In this case the shockwave has to travel only one length to reach the measurement point (sensor), thus the speed of sound in the metal (v) will be calculated by means of the formula:

$$\mathrm{v} = \frac{l}{t} \tag{3}$$

where l is the length or the tube of the rod, and t is the travelling time from the collision end to the free end.

As one can, the first three methods are somehow related, measuring the contact time via microcontroller, the fourth method uses a digital oscilloscope instead of the microcontroller and all methods lead to a speed of sound deduced by considering a back and forth travelling for the sound. For the fifth method, the sensor records a single length propagation from the contact end towards the free end where the sensor is placed.

RESULTS AND DISCUSSIONS

Performing some preliminary measurements, it was found that the collision times measured with the first four methods, as function of length, have the same order of magnitude for a given length and type of material, but the sound velocity calculated with equation (2) led to different values for each length. This result

suggests that the speed of sound might depend on the length of the tube or rod, finding that could not be true, therefore further, and deeper analysis must be done.

Plotting the collision times as function of tube length, for both copper and aluminum tubes, obtained with the first three methods, the plots presented below are obtained (Fig. 8).

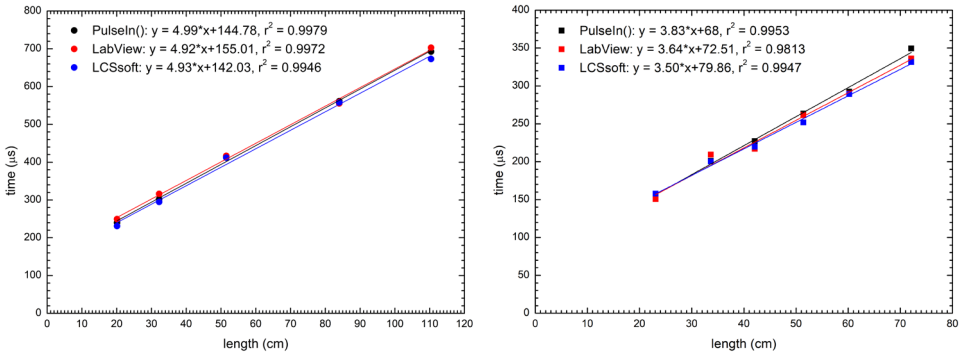

Fig. 8: The experimental results for the first three methods
(Cu tube – left, Al tube – right)

The results obtained by oscilloscope measurements are presented in Fig.9 and those with the piezo sensor in Fig.10.

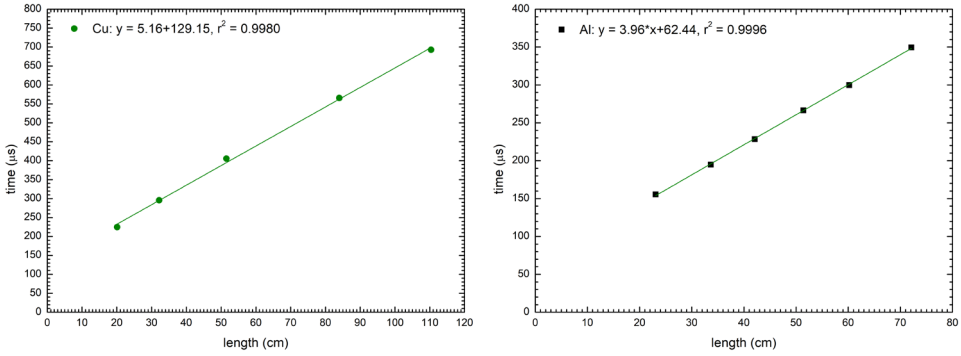

Fig. 9: Oscilloscope measurement results (Cu tube – left, Al – right)

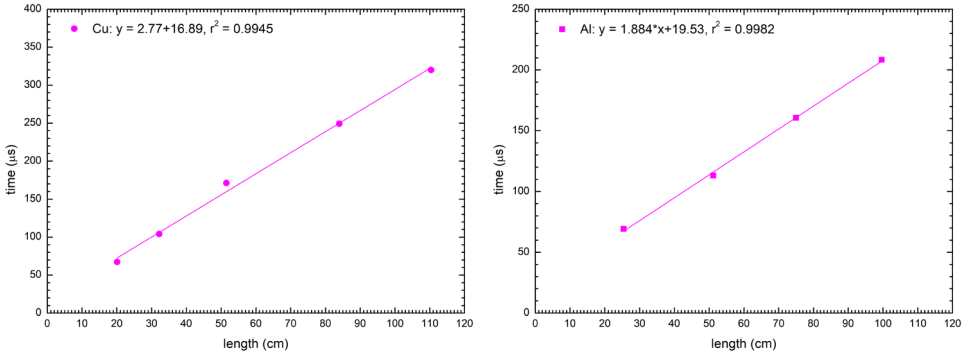

Fig. 10: Piezo sensor measurement results (Cu tube, Al rod)

As one can see, all plots demonstrate a good linear relationship between the collision time and the tube length (r-square > 0.99) and in all cases there is an offset time of about 100 μs when the first four methods are implemented, and less than 50 μs when the piezo sensor is used.

A qualitative explanation for the appearance of the offset time is given in the papers of Prowse and Brittoin [24, 25]. The variation of the pressure with time at the impact boundary is depicted below.

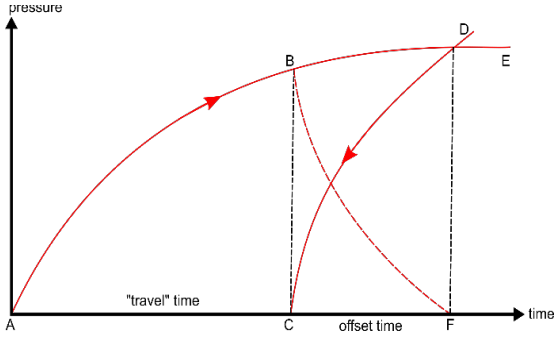

Fig. 11: Variation of pressure with time according to [24]

A compression pulse is initiated by the impact of the tube with the anvil. This will propagate along the tube towards the free and of it. Because of the finite length, the pulse will suffer a complete reflection with phase reversal. At this moment, the pulse will propagate from the free end towards the impact end with the velocity v and when arrives to the contact area (regarded as a rigid boundary) will suffer a perfect reflection but twice as fast. When the total pressure at the impact zone is reduced to zero, the tube will jump from the anvil and separates.

The initial growth in pressure at the impact end is represented by curve *AE* in Fig. 11. For the rod of length l, after a "travel" time $2l/\mathrm{v}$, the leading front of the initial stress pulse reaches the impact end (denoted point *C* on the time axes). The reflected pulse grows at twice rate of the initial pulse and it is depicted by curve *DC* in Fig. 11. This must be subtracted from the portion BE in order to obtain the resultant stress profile *BF*.

According to all these considerations, the total time of contact between the tube and the anvil will be given by the sum of two times, the travel time, and the time in the initial stress pulse necessary for the pressure to grow to half of its final value. This latter time corresponds to those offset times showed in Fig. 11.

Thus, the offset times deduced from the plots are subtracted from the measured impact times and with the resulted time twice of the length of the tube was divided in order to obtain the speed of sound (just the length in case of the piezo measurements).

The results (offset times and average velocities) of 30 time measurements for each tube or rod length given in Table 1, are summarized below (see Table 2).

Table 2. Tubes and rods used in experiment

Method	Material	Type	Offset time (μs)	Speed of sound (m/s)
#1	Cu	tube	155.01	4086.31
#2			144.78	4063.99
#3			142.03	4018.68
#1	Al	tube	72.51	5580.63
#2			68.00	5283.65
#3			76.86	5786.58
#4	Cu	tube	129.20	3940.77
	Al	tube	62.44	5066.29
		rod	154.41	5978.79
#5	Cu	tube	16.89	3661.40
	Al	tube	19.53	5295.79
		rod	1.49	4991.83

CONCLUSIONS

Five electrical methods based on the impact time measurement between a tub/rod and an anvil was implemented in order to determine the speed of sound propagation in metals.

It was experimentally demonstrated that, there is an offset time in the relationship of the measured impact time and the length of the tubes or rods. This offset time is not demonstrable if only one length is used and the deduced speeds will not be accurate.

The impact time is between 130 – 150 μs and the speed of sound between 3940 and 4087 m/s in case of copper tubes, and around 60 μs and 5000 – 5800 m/s in case of aluminum tubes, respectively. Larger values were found for Al rods.

These results are in good agreement with literature, 3810 m/s for Cu and 5000 m/s for Al [26].

The results obtained with the piezo sensor led to a relatively small offset time (less than 20 μs) and much better speeds, 3661 m/s for Cu and 4990 – 5300 m/s for Al, respectively.

REFERENCES

[1.] P. Murdin, “Full Meridian of Glory: Perilous Adventures in the Competition to Measure the Earth”, Springer, New York, 2008, p. 35–36.
[2.] R. Péter, “Speed of sound measurement via impact time measurements” BSc Thesis, Engineering Physics, Faculty of Physics, Babes-Bolyai University, Romania, July 2022.
[3.] ANSI/ASA S1.1-2013 - Acoustical Terminology - ANSI Webstore, https://webstore.ansi.org/standards/asa/ansiasas12013 (accessed April 2022)
[4.] LibreTexts PHYSICS (online): Introduction to Physics (Park), https://phys.libretexts.org/Bookshelves/Conceptual_Physics/Introduction_to_Physics_(Park), Unit 2: Mechanics I - Energy and Momentum, Oscillations and Waves, Rotation, and Fluids, Chapter 5: Oscillations and Waves, 5.7: Sound & 5.8: Speed of Sound, Frequency, and Wavelength (accessed April 2022)
[5.] A. Kundt, Annalen der Physik (in German). 127 (4): 497–523 (1866)
[6.] C. C. Carvalho, J. M. B. Lopes dos Santos, and M. B. Marques, The Physics Teacher 46, 428 (2008)
[7.] Z. Neda, FIRKA 2, 78 (1992)
[8.] R.M. Whittle and J. Yarwood “Experimental Physics for Students”, Chapman and Hall, London, 1973, p. 168-169
[9.] J. E. Girard, The Physics Teacher 17, 393 (1979)

[10.] W. G. B. Britton, J. J. Fendley, and M. E. Michael, Am. J. Phys. 46, 1124 (1978)
[11.] C. Fazio, I. Guastella, R. M. Sperandeo-Mineo and G. Tarantino, Eur. J. Phys., 27 687 (2006)
[12.] S. Ganci, Physics Education 46 (5) 533 (2011)
[13.] C. K. Manka, Am. J. Phys. 37 223 (1969)
[14.] S. Ganci, Physics Education 51 034003 (2016)
[15.] G. B. Karshner, Am. J. Phys. 57 920 (1989)
[16.] R. E. Berg and D. R. Brill, The Physics Teacher 43, 36 (2005)
[17.] S. Hellesund, Phys. Educ. 54 035015 (2019)
[18.] Arduino Uno, https://store.arduino.cc/arduino-uno-rev3 (accessed October 2021)
[19.] https://reference.arduino.cc/reference/en/language/functions/advanced-io/pulsein/ (accessed October 2021)
[20.] https://sigrok.org/wiki/Lcsoft_Mini_Board (accessed October 2021)
[21.] Tektronix MSO3000 and DPO3000 Series User Manual, https://download.tek.com/manual/071265602web.pdf (accessed October 2021)
[22.] Tektronix MSO3000 Series, DPO3000 Series Data Sheet. https://ro.mouser.com/datasheet/2/403/tektronix%20inc_3gw_21364_7_0-1207531.pdf (accessed October 2021)
[23.] J. Fraden, “Handbook of modern sensors: physics, designs, and applications”. Springer, 2016, Chapter 12.4
[24.] W.A. Prowse, The London, Edinburgh, and Dublin Philosophical Magazine and Journal of Science 22.146 209 (1936)
[25.] W. G. B. Britton, J. J. Fendley, and M. E. Michael, Am. J. Phys. 46, 1124 (1978)
[26.] D. R Lide, “CRC handbook of chemistry and physics”, CRC press, 2004, p. 14-41

STUDIA UBB PHYSICA, Vol. 68 (LXVIII), 1-2, 2023, pp. 83-94
(RECOMMENDED CITATION)
doi:10.24193/subbphys.2023.08

PREDICTION OF THE ANTIOXIDANT CHARACTER BY USING PHOTOCATALYTIC ACTIVITY OF DIFFERENTLY SHAPED CERIUM-OXIDE NANOPARTICLES

ZS.-R. TÓTH[1,2], K. MAGYARI[2], A. FERARU[1,2], I. SZEKELY[1,2], L. NÁNAI[3], A. DREANCA[4], L. BAIA[2,5*]

ABSTRACT. Injury is an everyday risk in our lives, but some of us could have several wound healing problems, originating from additional pathologies (diabetes, cancer, and vitamin defects). As a solution, some metal-based nanomaterials, such as cerium-oxide (CeO_2) could be applied, which could help the regeneration. The CeO_2 nanomaterials need to have antioxidant character in order to be used in wound healing. Besides the wide use of CeO_2 particles in the biological field, it could be also utilized as a catalyst. This study compares these two applications, analyzing the photocatalytic activity of differently shaped CeO_2 nanoparticles and their possible antioxidant character.

Keywords: *photocatalytic activity, morphology, cerium-oxide, nanomaterial, predicted antioxidant character*

[1] *Doctoral School in Physics, Faculty of Physics, Babeș-Bolyai University, M. Kogalniceanu 1, RO-400084, Cluj-Napoca, Romania.*
[2] *Centre of Nanostructured Materials and Bio-Nano Interfaces, Institute for Interdisciplinary Research on Bio-Nano-Sciences, Treboniu Laurian 42, Cluj-Napoca RO-400271, Romania.*
[3] *Institute of Physical Metallurgy, Metal Forming and Nanotechnology, University of Miskolc, Miskolc-Egyetemváros, HU-3515 Miskolc, Hungary.*
[4] *Faculty of Veterinary Medicine, University of Agricultural Science and Veterinary Medicine, Calea Manastur 3-5, RO-400372 Cluj-Napoca, Romania.*
[5] *Faculty of Physics, Babeș-Bolyai University, M. Kogalniceanu 1, Cluj-Napoca RO-400084, Romania.*
[*] *Corresponding author: lucian.baia@ubbcluj.ro*

INTRODUCTION

Cerium(IV)-oxide (CeO_2) is receiving a lot of attention in research today. But the question is why does it attract attention? What makes it special from many other metal-based nanomaterials? First, cerium is a metal from lanthanide serial and can switch its oxidation state depending on the environment (Ce^{3+} to Ce^{4+}) [1]. Second, it has two different oxides: (i) cubic–type structure of CeO_2 and (ii) hexagonal A–type structure of Ce_2O_3 [2]. CeO_2 is a much more stable form, which can be involved in catalytic [3], sensor [4], and biological applications [5]. The nanoparticles of CeO_2 (NP-CeO_2) have several unrivalled properties, such as antibacterial, antioxidant, antifungal, anti-inflammatory, angiogenic, anti-apoptotic, and oxygen storage capacity [5,6]. Even though the above-mentioned properties cannot be ignored for some areas of application, it is important to note that the applications in which CeO_2 is used, are greatly influenced by its shape, size, and surface defects that appear on its surface. Thus, the research attention turned to optimizing a synthesis method of NP-CeO_2. NP-CeO_2 could be synthesized with various synthesis methods, such as hydrothermal, precipitation, microwave-assisted, green synthesis, microemulsion, oxidation, and sonochemical [1]. The application of NP-CeO_2 in biological fields (such as cardiovascular, anti-diabetic, photoreceptor protection, wound healing, and biosensor [7]) is not surprising regarding the mentioned characters.

Wound healing has four different stages: hemostasis, inflammation, proliferation, and remodelling [8]. Several studies showed that in the last three stages of wound healing CeO_2 was involved, but only a few articles focused on hemostatic application [5]. To be used in the stage of hemostasis it needs to have several important characters. First, it needs to be stable, which being a metal oxide is not questionable. Second, it needs to have an antioxidant character and third, it needs to be an angiogenic character.

CeO_2 was used as a catalyst in several articles and industries [3], and therefore, the assumption that the NP-CeO_2 has a photocatalytic character is not surprising at all. Since the most widespread use of CeO_2 is as a photocatalyst, why not use this property to predict a preliminary antioxidant property? Thus, we can reduce several experiments. Starting from the fact that while model pollutant degradation needs to have charge carriers and the (photo)catalytic degradation takes place through redox reactions, an antioxidant will capture these radicals. Thus, according to our assumptions, substances proved to be photocatalytically active will not be antioxidants, while a nanoparticle with an antioxidant character will show non-photocatalytic properties. In this way, materials thought to be useless as catalysts may have new uses. Therefore, this article focuses on the synthesis of

differently shaped NP-CeO_2 and using them for paracetamol and methyl orange degradation, for prescreening of the antioxidant character, and for the possible future application in the hemostasis stage of wound healing.

EXPERIMENTAL

Synthesis of the nanocubes and polyhedral of CeO_2

The hydrothermal synthesis method of the nanocubes and polyhedral nanoparticles only differs from the used amount of NaOH (sodium-hydroxide, pellets, 99%, VWR Chemicals) and it is based on the synthesis methods of Mai and co-workers [9]. As cerium precursor $Ce(NO_3)_3 \cdot 6H_2O$ (cerium (III)-nitrate hexahydrate, 99%, Sigma-Aldrich) was used in both syntheses of nanocubes and polyhedral. Two different solution was made with mentioned precursors: (1) 0,868 g of $Ce(NO_3)_3 \cdot 6H_2O$ was added into 5 mL of ultrapure water and (2) 8,4 g of NaOH (amount used for the synthesis of nanocube) // 14 mg of NaOH (amount used for the synthesis of polyhedral) was added into 35 mL of ultrapure water (in ice bath). Both solutions were introduced into a Teflon autoclave and were stirred at room temperature for 30 minutes, afterward, it was transferred into an oven and kept at 180°C for 24 hours. The solution was cleaned for the unreacted components with a centrifugation cleaning process for 10 min and 6,000 RPR with 2 × 50 mL of ultrapure H_2O and 2 × 25 mL EtOH (absolute ethyl alcohol; Chimreactiv SRL). The abbreviation of the samples will be the following: nanocubes and polyhedral.

Synthesis of the nanosphere of CeO_2

The synthesis method of nanosphere was produced using Wang and co-workers [10] hydrothermal synthesis method. The cerium precursor was the same used for the synthesis of nanocubes and polyhedral particles. Polyvinylpyrrolidone (PVP, average mol wt. 40,000; Sigma-Aldrich) was used as a shaped-tailoring agent. In a solution of 30 mL of EtOH and 10 mL ultrapure water 1.63 g $Ce(NO_3)_3 \cdot 6H_2O$ and 1.11 g PVP were added. The mixture was stirred for 30 minutes and transferred to an oven, where it was kept at 160°C for 1 hour. The obtained solution was centrifuged at 15,000 RPR for 5 minutes in 2 mL of Eppendorf and cleaned several times with water. Only the white part of the solution was dried and used for analysis. The obtained nanoparticles will be abbreviated as nanosphere.

Characterization, adsorption, and photocatalytic test

The obtained nanoparticles were **characterized** by:

- Shimadzu 6000 X-ray diffractometer (XRD), with the following parameters: 40 kV (30 mA), radiation with $\lambda_{CuK\alpha}$ = 1.54 Å), scanning between 5 and 80° (2θ range), and with scan speed 2° · min^{-1}.
- FEI Technai G2 F20 high-resolution transmission electron microscopy (TEM) with 200 kV and 300 mesh Cu grid.
- Confocal multi-laser Renishaw inVia Reflex spectrometer equipped with a Rencam CCD detector with the following laser parameters: 633 nm, and 17 mW.
- Jasco-V650 diffuse reflectance spectroscopy (DRS) equipped with an ILV-724 integrative sphere, the spectrum was taken between 190-800 nm. Kubelka Munk equation [11] was used to estimate the bandgap energy values of samples.

The **adsorption test** was used to understand the adsorption properties of the sample. 30 mg of nanomaterial was added in 30 mL of methyl orange (Chempur, 97%; C=50 µM)/ paracetamol (Helcor, pill of 500 mg; C=0.1 mM). A 50 mL Berzelius beaker was used, and it was surrounded with aluminium foil, to avoid all the sunlight. The sampling was in 20, 40, 60, 90, 120 minutes. The obtained sample was centrifugated (3 minute, 15,000 RPR), filtered and the concentration changes were analyzed using JASCO-V650 tip spectrophotometry.

A double-walled photoreactor, with a suspension concentration of 1 mg · mL^{-1} was used for analyzing the **photocatalytic activity** of the samples. Two different model pollutants were used: (i) methyl orange (C=50 µM) and (ii) paracetamol (C=0.1 mM) and two different lamp sources were used: (i) 6 × 6 W UV lamps and (ii) 6 × 15 W visible lamps (only in the case of MO). The test was taken for 2 hours, with a sampling from ten to ten minutes in the first hour and then from 20 to 20 minutes in the second hour. Before the test, the suspensions were ultrasonicated for 15 minutes and they were kept in the dark for 10 minutes to reach the adsorption-desorption equilibrium. The concentration changes of the model pollutant were determined for the MO the same as in the case of the adsorption test. Merck-Hitachi L-7100 high-performance liquid chromatography (within a low-pressured gradient pump; Merck-Hitachi L-4250 UV-Vis detector, and Lichrospher Rp 18 column) was used to define the concentration change for paracetamol measurements. The used parameters were the following: eluent - Acetonitrile: H_2O=20:80, adjusted to a 2.30 pH using 85% phosphoric acid, flow rate: 0.500 mL · min^{-1}, and detection wavelength at 243 nm.

The paracetamol (Helcor; 500 mg) was cleaned before being used. We used 3 different pills to determine the purity of the active substance. We made a solution, which was filtered with traditional filter paper thus cleaning the paracetamol from possible additives (such as starch).

RESULTS AND DISCUSSION

Two different synthesis methods were used to obtain differently shaped CeO_2 nanoparticles. First, the synthesis methods of nanocubes and polyhedral-shaped nanomaterials are similar, only the amount of NaOH is changed. Similarly with Mai and co-worker [9], we have found that the crystallinity is shape-dependent, and moreover, the pH of the reaction solution influences the obtained shape. The most crystalline nanostructures were obtained in the case of nanocubes.

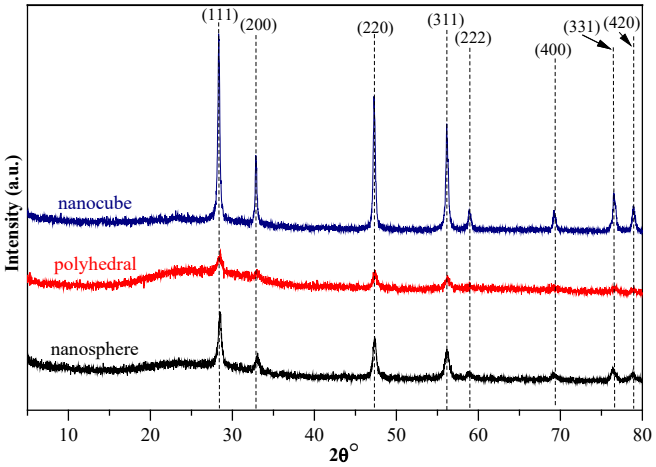

Fig. 1: The XRD patterns of differently shaped CeO_2 nanomaterials: nanocube (blue line), polyhedral (red line), and nanosphere (black line)

In addition, using only additives (in our case PVP; Fig. 1) for the synthesis of nanosphere, higher crystallinity compared with the polyhedral-shaped nanostructures, but lower crystallinity compared to the nanocubes, was observed. All typical reflections of NP-CeO_2 were observed (Fig. 1) in the XRD patterns at 28.55°, 32.81°, 47.26°, 56.20°, 58.95°, 69.27°, 76.61°, and 78.90° indexed with the following Miller indexes (111), (200), (220), (311), (400), (331), (420) using the COD nr. 00-434-3161 card to verify. Indifferent from the obtained shaped, all the reflections were observed in all patterns. No additional reflection was detected in the XRD patterns.

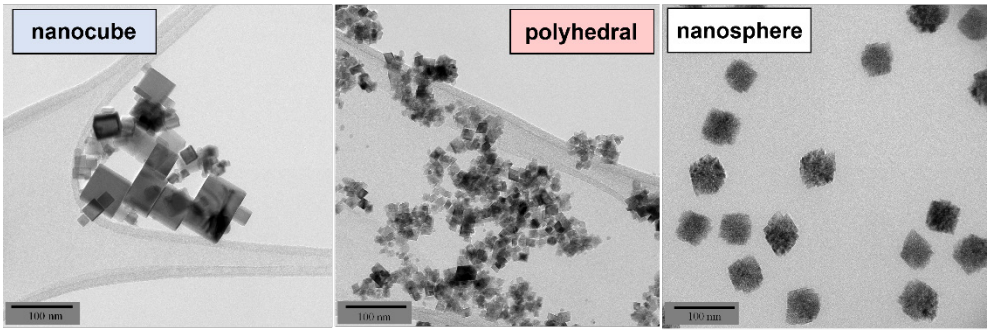

Fig. 2: Transmission electron micrographs of differently shaped CeO_2 nanomaterials: nanocube (đ~25 nm), polyhedral shaped (đ~15 nm), and nanosphere (đ~60 nm).

The next step of this research was to analyze the morphology of the samples for which TEM measurements were used. As can be seen in Fig. 2 all the desired morphologies were synthesized. Unfortunately, the nanocubes have the lowest monodispersity. The highest monodispersity was achieved in the case of the nanospheres. This synthesis method differs from the one used for nanocubes and polyhedral-shaped particles. All the particle sizes of nanomaterials are in the accepted range to be used in biomedical applications, such as wound healing, which are the further plans of this study.

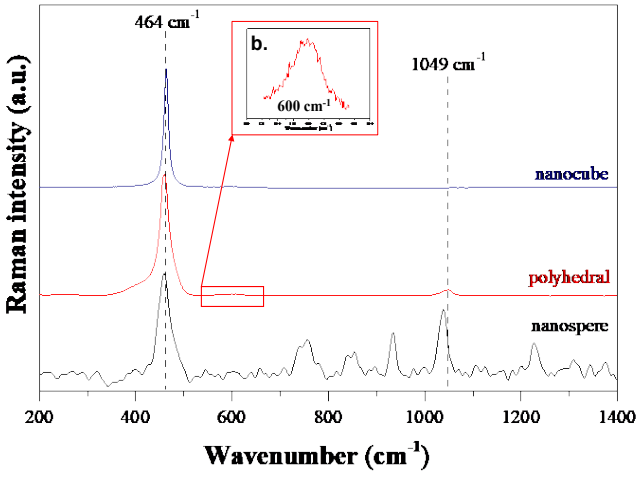

Fig. 3: The Raman spectra for differently shaped CeO_2 nanomaterials: nanocube (blue line), polyhedral (red line), and nanosphere (black line): entire graphs (a) and inserted graph - magnified (b)

According to the XRD measurements (Fig. 1), the samples have different crystallinity amounts regarding the obtained form. Thereby, Raman spectra (Fig. 3) were taken to observe the possible oxygen vacancies in the samples. First, it needs to be mentioned, that the presence of the PVP, which remained from the synthesis, was observed in the Raman spectra of the nanosphere. This PVP could not be washed from the surface of the NP-CeO_2, as tested by the immersion in EtOH and H_2O for 24 hours (this will be not presented here). The PVP adsorption on the surface of the CeO_2 was confirmed by S. Lakhwani *et al.* [12]. The presence of the PVP could be the reason for the low crystallinity, as confirmed by the XRD measurements (Fig. 1). The presence of the PVP does not have a negative effect on the applicability in a biological system [13], thereby the obtained sample is used as synthesized. Three Raman bands were observed in Fig. 3. The most intensive band originates from the cubical structure of the samples and the broadening of the signal (464 cm^{-1}) could be assumed for the obtained morphology [14]. Besides the typical band for CeO_2, two other bands were observed at 610 and 1062 cm^{-1}, which could be attributed to the presence of oxygen vacancies [14]. These bands overlap in the case of nanospheres but are presented in polyhedral. These could be the reason for the low crystallinity since they are not presented in nanocube spectra.

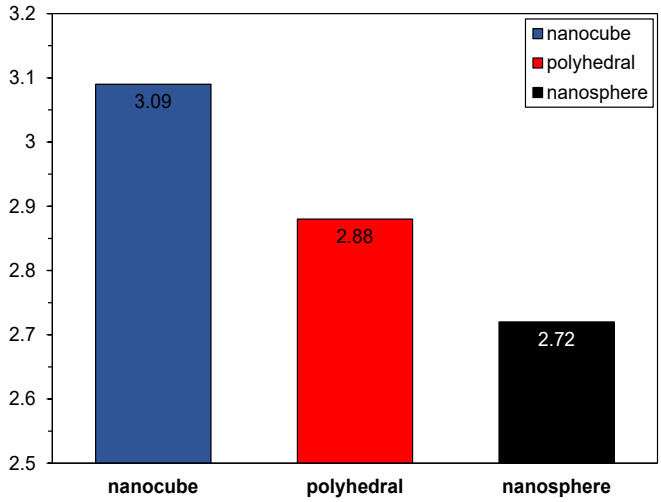

Fig. 4: The estimated bandgap energy values calculated by Kubelka Munk equation for the CeO_2 nanomaterials: nanocube, polyhedral, and nanosphere.

Using a nanomaterial for photocatalytic activity analyzes is necessary to determine their bandgap energy values. The NP-CeO_2 have a bandgap energy value between 3 and 3.40 eV [15]. Similar to TiO_2, it is a UV-active photocatalyst but has

higher oxygen mobility. Surprisingly, the obtained nanomaterials have lower bandgap energy values without any noble metal, or other additional metal-oxide (such as CuO, Ag_3PO_4) capable to reduce the bandgap energy. The obtained values (Fig. 4) show that polyhedral and nanospherical particles could be irradiated by visible light irradiation, while nanocubes can be activated by UV light irradiation. It is important to note that the photocatalytic activity of a nanostructure does not only depend on its bandgap energy but also on its surface properties and the type of model compound chosen. Before starting to discuss the photocatalytic degradation of the chosen model pollutant, it is necessary to understand the relationship between the nanostructure and the model compound, for which we performed adsorption tests (Fig. 5-6).

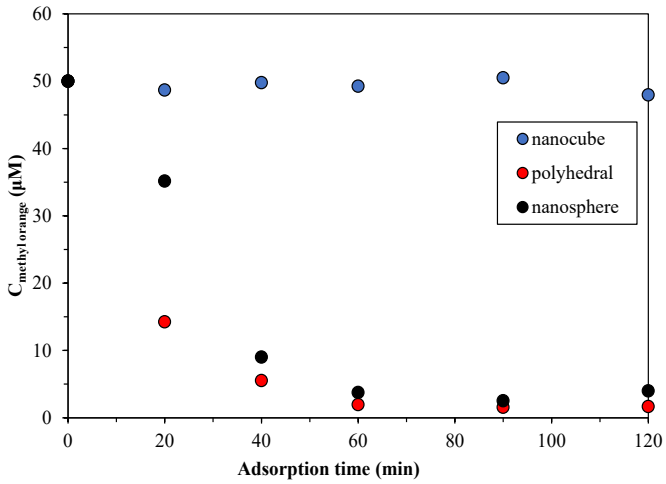

Fig 5: The MO adsorption test of differently shaped CeO_2 nanomaterials: nanocube (blue dots), polyhedral (red dots), and nanosphere (black dots).

The MO adsorption test of CeO_2 nanomaterials shows that the polyhedral-shaped and nanospherical nanoparticles have adsorbed the total amount of MO. Therefore, its photocatalytic activity cannot be determined. Against this, the nanocube does not adsorb any of the MO. The result was compared with the XRD patterns (Fig. 1), where the most crystallized particles were the nanocube-formed particles. In the case of spherical and polyhedral particles, differences can be observed, the magnitude of which is small, but the spherical particles show slower adsorption (Fig. 5). As it was seen in XRD patterns (Fig. 1), the spherical structures exhibited higher crystallinity. According to our assumption, the nanoparticles may have an amorphous structure, so that the MO molecules are adsorbed on their

surface, moreover, the presence of the oxygen vacancies could favor the adsorption of the MO molecules. Thus, our further assumption is that the crystallinity of the nanoparticles is related to their photocatalytic applicability, since the complete adsorption of the model compound, the existence of photocatalytic activity can be completely ruled out.

Although we expected similar results during the adsorption of paracetamol, we were surprised to find that no adsorption was observed in all cases, independently of the synthesized morphology.

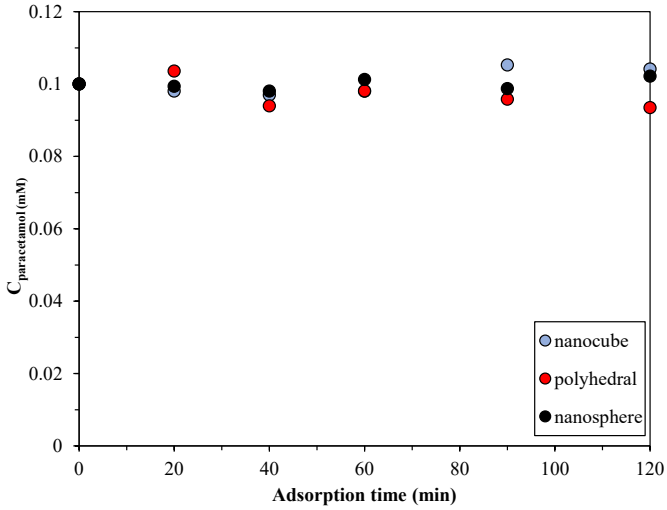

Fig. 6: The paracetamol adsorption of differently shaped CeO_2 nanomaterials: nanocube (blue dots), polyhedral (red dots), and nanosphere (black dots).

The next step of our studies was to assess the photocatalytic activity by using MO, as a model pollutant, and visible and UV light, as an irradiation source. Based on the observed adsorption we will discuss only the degradation using nanocubes. First, we used visible light irradiation, where no photocatalytic activity of nanocubes was observed. In this case, the estimated bandgap energy is at 3.09 eV (Fig. 4), therefore it is not surprising that no photoactivity was observed (Fig. 7a). Secondly, the same test was done; only the lamp`s source was changed to UV light, where no degradation was observed either (Fig. 7b). Therefore, it can be concluded that by using MO as a model pollutant no degradation could be seen regardless of the used lamp source (Fig. 7). This could be predicted to have a good antioxidant character.

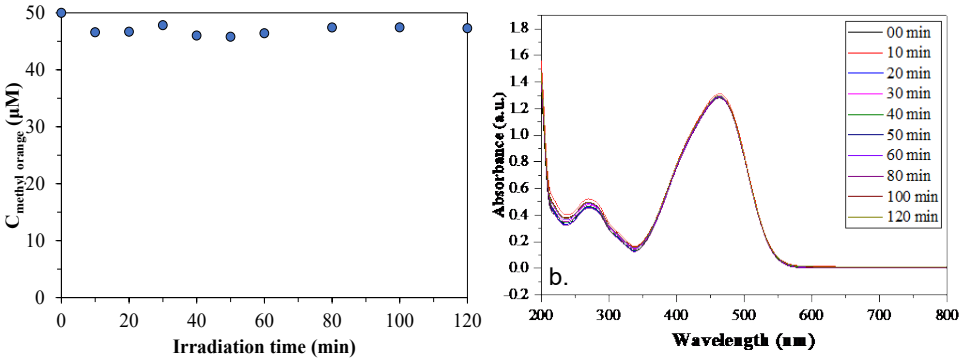

Fig 7: The photocatalytic degradation of MO using nanocube in visible (a) and UV light (b) irradiation.

The paracetamol degradation of CeO_2 nanomaterials was done by using UV light as a light source. No degradation of paracetamol was observed regardless of the differently shaped nanomaterials. Thereby, we assume a good antioxidant character. It needs to be emphasized that the obtained materials have sufficient bandgap energy for producing photocatalytic activity and in the case of polyhedral the presence of oxygen vacancies was also confirmed. The no photocatalytic activity observed in the case of MO (Fig. 7) and paracetamol (Fig. 8) could be a predictor for high antioxidant character.

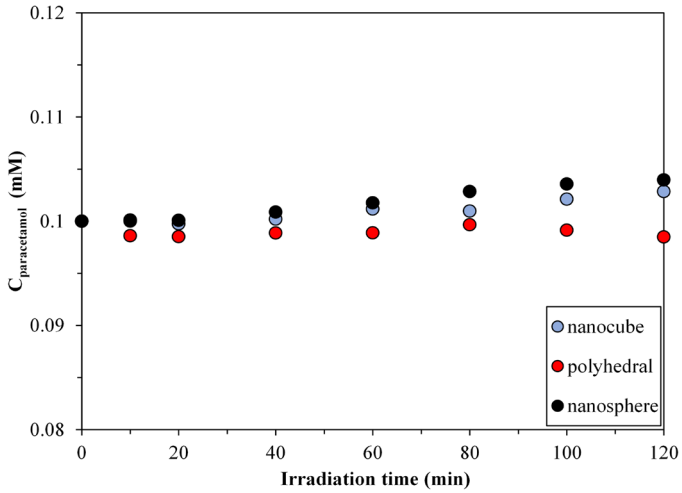

Fig 8: The photocatalytic degradation of paracetamol using nanomaterials: nanocube (blue dots), polyhedral (red dots), and nanosphere (black dots) (due to the small amount of material the 30- and 50-minutes sample was not taken).

The reason for this is that during a photocatalytic activity is mandatory to have charge carriers (e^- and h^+), which could start the degradation of the organic dyes by oxidation of its. Having an antioxidant, as a definition “delays or prevents oxidation of that substrate” [16], therefore the oxidation with the charge carriers is less probable to occur.

CONCLUSIONS

In this work were synthesized two different morphologies of CeO_2 nanoparticles (nanocube, and nanosphere) and a reference material in the form of polyhedral nanoparticles. It has been confirmed that the crystallinity of the samples has a relation with the obtained morphologies. Adsorption of the MO was observed in the case of nanosphere and polyhedral-shaped nanoparticles. No paracetamol and MO degradation was confirmed regardless of the used CeO_2. The non-photocatalytic activity could predict a good antioxidant character and a promising application in wound healing.

ACKNOWLEDGMENT

This work was supported by the project "The Development of Advanced and Applicative Research Competencies in the Logic of STEAM + Health”/POCU/ 993/6/13/153310, project co-financed by the European Social Fund through The Romanian Operational Programme Human Capital 2014-2020. Zs.-R. Toth acknowledges the financial support of MTA Domus 153/10/2022/HTMT.

REFERENCES

[1] N. Thakur, P. Manna, J. Das, J Nanobiotechnology 17 (2019) 84.
[2] L. Sun, W. Xiao, X. Hao, Q. Meng, M. Zhou, Electronic Structure 1 (2019) 015003.
[3] T. Montini, M. Melchionna, M. Monai, P. Fornasiero, Chem Rev 116 (2016) 5987–6041.
[4] H. Li, Y. Qu, X. Zhang, Inorg Chem Commun 130 (2021) 108692.
[5] H. Sadidi, S. Hooshmand, A. Ahmadabadi, S.J. Hoseini, F. Baino, M. Vatanpour, S. Kargozar, Molecules 25 (2020) 4559.
[6] S. Pansambal, R. Oza, S. Borgave, A. Chauhan, P. Bardapurkar, S. Vyas, S. Ghotekar, Applied Nanoscience (Switzerland) 26 (2022) 905.
[7] M.A. Saifi, S. Seal, C. Godugu, Journal of Controlled Release 338 (2021) 164–189.

[8] I. Kalashnikova, S. Das, S. Seal, Nanomedicine 10 (2015) 2593–2612.
[9] H.X. Mai, L.D. Sun, Y.W. Zhang, R. Si, W. Feng, H.P. Zhang, H.C. Liu, C.H. Yan, Journal of Physical Chemistry B 109 (2005) 24380–24385.
[10] Q. Wang, W. Jia, B. Liu, W. Zhao, C. Li, J. Zhang, G. Xu, Chem Asian J 7 (2012) 2258–2267.
[11] J. Tauc, Mat. Res. Bull 3 (1968) 37–46.
[12] S. Lakhwani, M.N. Rahaman, J Mater Sci 34 (1999) 3909–3912.
[13] M. Bejaoui, H. Galai, F. Touati, S. Kouass, in: Dosage Forms - Innovation and Future Perspectives, IntechOpen, 2023.
[14] G. Jayakumar, A. Albert Irudayaraj, A. Dhayal Raj, Opt Quantum Electron 51 (2019) 312.
[15] S. Scirè, L. Palmisano, in: Cerium Oxide (CeO2): Synthesis, Properties and Applications, Elsevier, 2019, pp. 1–12.
[16] K. Brainina, N. Stozhko, M. Vidrevich, Antioxidants 8 (2019) 297.